

Department of Earth and Environmental Sciences (DISAT)
PhD program in Chemical, Geological and Environmental Sciences
Cycle XXXII
Curriculum in Environmental Sciences

Characterization of temporal variability of Plant Traits and Ecosystem Functional Properties using optical signals

Surname: Biriukova

Name: Khelvi

Registration number: 824409

Tutor: Micol Rossini

Coordinator: Prof. Maria Luce Frezzotti

ACADEMIC YEAR 2018/2019

CONTENTS

List of figures	6
List of tables.....	10
Acknowledgements	11
Abstract	12
1. Introduction.....	1
1.1. Plant Traits and Ecosystem Functional Properties	1
1.2. Remote sensing of Plant Traits and Ecosystem Functional Properties	1
1.3. Optical indicators of plant physiological activity.....	2
1.4. Rationale and research gaps	6
1.5. Objectives	7
1.6. Thesis outline.....	7
2. Part 1. Effects of varying solar-view geometry and canopy structure on solar-induced chlorophyll fluorescence and <i>PRI</i>	9
2.1. Introduction.....	10
2.2. Materials and methods	12
2.2.1. Spectral data collection and study sites	12
2.2.2. Spectral measurements protocol	14
2.2.2.1. Protocol to characterize the diurnal cycles of the angular distribution of F , <i>sPRI</i> and R	14
2.2.2.2. Protocol to characterize the angular distribution of F , <i>sPRI</i> and R over the hemisphere	15
2.2.2.3. Measure of anisotropy	15
2.2.3. Acquisition of biochemical and structural parameters	16
2.2.4. Simulations of spectro-directional response of F	17
2.3. Results	18
2.3.1. Diurnal changes of the angular distribution of F , <i>sPRI</i> and R in the SPP, CPP and AR.....	18
2.3.1.1. Chickpea: R , F and <i>sPRI</i> in the SPP and CPP	18
2.3.1.2. Grass: R , F and <i>sPRI</i> in the SPP and CPP	20
2.3.1.3. Rice: R , F and <i>sPRI</i> in the SPP and AR	22
2.3.2. Midday cycles	25
2.3.3. Effects of canopy structure on F_{760} and F_{687} directional response in the SPP	27
2.3.3.1. Modelling results	27
2.3.3.2. Comparison between F directional responses of canopies with different structural properties	27
2.3.4. Fluorescence apparent yield and <i>sPRI</i> daily averages	28
2.4. Discussion	29
2.4.1. Fluorescence and <i>sPRI</i> anisotropy as a function of solar-view geometry	29
2.4.2. Effects of structural parameters on fluorescence directional response in the SPP: comparison between observations and simulations	31

2.4.3. Fluorescence apparent yield and <i>sPRI</i> daily variations as a function of VZA and RAA: Implications for the ground measurements.....	32
2.5. Conclusions.....	33
2.6. Supplementary material.....	34
3. Part 2. Extracting the vegetation physiological response from time series of solar-induced chlorophyll fluorescence and PRI using Singular Spectrum Analysis	45
3.1. Introduction.....	46
3.2. Theoretical background: Singular Spectrum Analysis	48
3.3. Proof of the concept: a model-based study	50
3.3.1. Methods	50
3.3.1.1. SCOPE simulations	50
3.3.1.2. SSA decomposition	54
3.3.1.3. Statistical analysis.....	55
3.3.2. Results	56
3.3.2.1. Seasonal cycles of simulated variables.....	56
3.3.2.2. $\Delta PRI_{\text{scope}}$ and $\Delta F_{760}^{\text{scope}}$ as a function of vegetation physiological response	57
3.3.2.3. Proof of concept : extraction of slow dynamics from $PRI_{\text{xan}}^{\text{scope}}$, F_{760}^{scope} and $Fy_{760}^{*\text{scope}}$ with SSA	59
3.3.2.4. Proof of concept: extraction of fast variability from $PRI_{\text{xan}}^{\text{scope}}$, F_{760}^{scope} and $Fy_{760}^{*\text{scope}}$ with SSA	59
3.3.2.5. Link between fast SSA components of $PRI_{\text{xan}}^{\text{scope}}$, F_{760}^{scope} , $Fy_{760}^{*\text{scope}}$ and light-use efficiency	61
3.3.3. Discussion	63
3.3.3.1. Performance of SSA in separation of seasonal and fast dynamics in optical signals	63
3.3.3.2. Limitations and applicability to field data	66
3.4. Case study: application of SSA to measured time series of optical signals	68
3.4.1. Methods	68
3.4.1.1. Study site	68
3.4.1.2. Spectral measurements and data processing and F retrieval	68
3.4.1.3. Eddy covariance flux measurements and meteorological data	70
3.4.1.4. Acquisition of biochemical and structural parameters	71
3.4.1.5. SSA decomposition	72
3.4.2. Results and discussion	72
3.4.2.1. Overview of seasonal cycles	72
3.4.2.2. Extraction of seasonal dynamics from PRI , LUE^* , F_{760} and Fy_{760}^*	74
3.4.2.3. Extraction of fast variability from PRI , LUE^* , F_{760} and Fy_{760}^*	74
3.5. Conclusions.....	77
4. Thesis Summary and Conclusions.....	78

4.1.	Main results	78
4.1.1.	Part 1.	78
4.1.2.	Part 2.	78
4.2.	Concluding remarks.....	79
5.	Bibliography.....	80

List of figures

Figure 1	<i>Distribution of absorbed light in a leaf: photochemical quenching, energy dissipation as heat (NPQ) and chlorophyll fluorescence (modified from Gamon, 2015).</i>	3
Figure 2	<i>Left panel: multi-angular spectral measurements of chickpea with the FloX system and the goniometer with figure 3 schematic representation of the solar principal plane (SPP) with its backward and forward scatter directions and cross principle plane (CPP). Right panel: the photographs of studied canopies inside the azimuthal circle of the goniometer device (A – chickpea, B – alfalfa, C – grass, D – rice).</i>	13
Figure 3	<i>For chickpea in the SPP: the distribution of F_{760}, F_{687}, sPRI (row 1), R_{750}, R_{680}, R_{570} (row 2) and $F_{760} - R_{750}$, $F_{687} - R_{680}$, sPRI - R_{570} (row 3) as a function of SZA and VZA. F, sPRI and R were scaled between 0 and 1 before subtraction. Negative values of SZA correspond to the cycles acquired before midday, positive - after midday. Negative values of VZA represent the backscatter direction, positive – the forward scatter direction within a plane. The points of measurements are marked with white points. The values between the measurements are linearly interpolated.</i>	19
Figure 4	<i>For chickpea in the CPP: the distribution of F_{760}, F_{687}, sPRI (row 1) R_{750}, R_{680}, R_{570} (row 2) and $F_{760} - R_{750}$, $F_{687} - R_{680}$, sPRI - R_{570} (row 3) as a function of SZA and VZA. F, sPRI and R were scaled between 0 and 1 before subtraction. Negative values of SZA correspond to the cycles acquired before midday, positive - after midday. Negative values of VZA represent the backscatter direction, positive – the forward scatter direction within a plane. The points of measurements are marked with white circles. The values between the measurements are linearly interpolated.</i>	20
Figure 5	<i>For grass in the SPP: the distribution of F_{760}, F_{687}, sPRI (row 1), R_{750}, R_{680}, R_{570} (row 2), and $F_{760} - R_{750}$, $F_{687} - R_{680}$, sPRI - R_{570} (row 3) as a function of SZA and VZA. F, sPRI and R were scaled between 0 and 1 before subtraction. Negative values of SZA correspond to the cycles acquired before midday, positive - after midday. Negative values of VZA represent the backscatter direction, positive – the forward scatter direction within a plane. The points of measurements are marked with white circles. The values between the measurements are linearly interpolated.</i>	21
Figure 6	<i>For grass in the CPP: the distribution of F_{760}, F_{687}, sPRI (row 1), R_{750}, R_{680}, R_{570} (row 2), and $F_{760} - R_{750}$, $F_{687} - R_{680}$, sPRI - R_{570} (row 3) as a function of SZA and VZA. F, sPRI and R were scaled between 0 and 1 before subtraction. Negative values of SZA correspond to the cycles acquired before midday, positive - after midday. Negative values of VZA represent the backscatter direction, positive – the forward scatter direction within a plane. The points of measurements are marked with white circles. The values between the measurements are linearly interpolated.</i>	22
Figure 7	<i>For rice in the SPP: the distribution of F_{760}, F_{687}, sPRI (row 1), R_{750}, R_{680}, R_{570} (row 2), and $F_{760} - R_{750}$, $F_{687} - R_{680}$, sPRI - R_{570} (row 3) as a function of SZA and VZA. F, sPRI and R were scaled between 0 and 1 before subtraction. Negative values of SZA correspond to the cycles acquired before midday, positive - after midday. Negative values of VZA represent the backscatter direction, positive – the forward scatter direction within a plane. The points of measurements are marked with white circles. The values between the measurements are linearly interpolated.</i>	23

	<i>of measurements are marked with white circles. The values between the measurements are linearly interpolated.</i>	
Figure 8	<i>For rice in the AR: the distribution of F_{760}, F_{687}, sPRI (row 1), R_{750}, R_{680}, R_{570} (row 2), and $F_{760} - R_{750}$, $F_{687} - R_{680}$, sPRI - R_{570} as a function of SZA and VZA. F, sPRI and R were scaled between 0 and 1 before subtraction. Negative values of SZA correspond to the cycles acquired before midday, positive - after midday. Negative values of VZA represent the backscatter direction, positive - the forward scatter direction within a plane. The points of measurements are marked with white circles. The values between the measurements are linearly interpolated.</i>	24
Figure 9	<i>Polar plots of the angular distribution of F_{760}, F_{687}, R_{750}, R_{680}, R_{570} and sPRI measured in chickpea, alfalfa, grass and rice canopies as a function of VZA and RAA.</i>	26
Figure 10	<i>Distribution of multi-angular F_{760} (left) and F_{687} (right) in the solar principal plane (SPP) as a function of VZA for alfalfa, chickpea and rice measured with SZA of 22 - 30° and SAA of 220 - 230°, and grass measured with SZA of 39° and SAA of 184°. Negative values of VZA represent the backscatter direction, positive - the forward scatter direction within a plane.</i>	28
Figure 11	<i>The daily average values for Fy^*_{760}, Fy^*_{687} and sPRI obtained at four VZAs (0°, 15°, 30°, 45°) with four RAAs (0°, 90°, 18°, 270°) for chickpea (row 1), grass (row 2) and rice (row 3).</i>	29
Figure S1	<i>Diurnal cycles of PAR, F_{760}, F_{687} and PRI acquired from a nadir-viewing direction for chickpea (row 1), grass (row 2) and rice (row 3). Error bars for chickpea and rice indicate standard deviation ($n = 3$). Measurements over the grass were collected as a single acquisition ($n = 1$). Negative values of SZA correspond to the cycles acquired before midday, positive - after midday.</i>	34
Figure S2	<i>Distribution of multi-angular F_{760} (A) and F_{687} (B) in the solar principal plane (SPP) as a function of view zenith angle (VZA) and LIDF (erectophile, planophile and spherical) simulated with the SCOPE model. LAI = 3 m² m⁻², SZA = 0°, C_{ab} = 40 ug cm⁻², hc = 0.5 m, lw = 0.05 m. Negative values of VZAs represent the backscatter direction, positive – the forward scatter direction within a plane.</i>	39
Figure S3	<i>Distribution of multi-angular F_{760} (top) and F_{687} (bottom) in the solar principal plane (SPP) as a function of view zenith angle (VZA) and LAI simulated with the SCOPE model for erectophile (left), spherical (middle) and planophile (right) canopy types. SZA = 30°, C_{ab} = 40 ug cm⁻², hc = 0.5 m, lw = 0.05 m. Negative values of VZAs represent the backscatter direction, positive – the forward scatter direction within a plane.</i>	40
Figure S4	<i>Distribution of multi-angular F_{760} (top) and F_{687} (bottom) in the solar principal plane (SPP) as a function of view zenith angle (VZA) and sl simulated with the SCOPE model for erectophile (left), spherical (middle) and planophile (right) canopy types. LAI = 3 m² m⁻², SZA = 30°, C_{ab} = 40 ug cm⁻². Negative values of VZAs represent the backscatter direction, positive - the forward scatter direction within a plane.</i>	40
Figure S5	<i>Distribution of multi-angular F_{760} (top) and F_{687} (bottom) in the solar principal plane (SPP) as a function of view zenith angle (VZA) and SZA simulated with the SCOPE model for erectophile (left), spherical (middle) and planophile (right) canopy types. LAI = 3 m² m⁻², C_{ab} = 40 ug cm⁻², hc =</i>	43

	<i>0.5 m, $lw = 0.05$ m. Negative values of VZAs represent the backscatter direction, positive – the forward scatter direction within a plane.</i>	
Figure 12	<i>Schematic diagram of SCOPE simulations and SSA analysis.</i>	52
Figure 13	<i>Time series of (A) air temperature (T_{air}), (C) vapor pressure deficit (VPD), (E) soil moisture content (SM_p), (G) photosynthetically active radiation (PAR), (I) leaf area index (LAI) and chlorophyll content (C_{ab}), (B) gross primary production (GPP), (D and F) photochemical reflectance index affected and not affected by xanthophyll cycle de-epoxidation (PRI_{xan}^{scope}, PRI_0^{scope}) and (H and J) far-red fluorescence simulated with and without fluorescence amplification factor ϕ'_f (F_{760}^{scope}, $F_{0,760}^{scope}$). Colour lines represent mean daily values for T_{air}, VPD and PAR, and mean daily values in the time interval between 10 and 3 pm for GPP, PRI_{xan}^{scope}, PRI_0^{scope}, F_{760}^{scope}, $F_{0,760}^{scope}$.</i>	57
Figure 14	<i>(A) Relationship between ΔPRI^{scope} and NPQ and (B) coefficients of determination (R^2) for linear relationships between ΔPRI^{scope} and NPQ aggregated by LAI classes of equal size. (C) Relationship between ΔF_{760}^{scope} and ϕ'_f and (D) coefficients of determination (R^2) for linear relationships between ΔF_{760}^{scope} and ϕ'_f aggregated by LAI classes of equal size. The data presented on the figure correspond to daytime data, SZA $\leq 80^\circ$ and the fraction of the day between 0.2 and 0.8.</i>	58
Figure 15	<i>(A) Relationship between PRI_{xan}^{ssa} [seasonal] and PRI_0^{scope}, (B) F_{760}^{ssa} [seasonal] and $F_{0,760}^{scope}$, and (C) Fy^{*ssa}_{760} [seasonal] and $Fy^{*scope}_{0,760}$. The data presented on the figure correspond to daytime data, SZA $\leq 80^\circ$ and the fraction of the day between 0.2 and 0.8.</i>	59
Figure 16	<i>(A) Relationship between PRI_{xan}^{ssa} [diurnal + sub-diurnal] and ΔPRI^{scope} and R^2 for linear relationships PRI_{xan}^{ssa} [diurnal + sub-diurnal] vs PRI_0^{scope} and PRI_{xan}^{ssa} (30 min – 1 week) vs NPQ aggregated by LAI classes of equal size (D); (B) F_{760}^{ssa} [diurnal + sub-diurnal] and ΔF_{760}^{scope} and R^2 for linear relationships aggregated by LAI classes of equal size (E); (C) Fy^{*ssa}_{760} [diurnal + sub-diurnal] and ΔF_{760}^{scope}/PAR and R^2 for linear relationships aggregated by LAI classes of equal size (F). The data presented on the figure correspond to daytime data, SZA $\leq 80^\circ$ and the fraction of the day between 0.2 and 0.8.</i>	60
Figure 17	<i>(A) Relationship between PRI_0^{ssa} [diurnal + sub-diurnal] and ΔPRI^{scope}; (B) $F_{0,760}^{ssa}$ [diurnal + sub-diurnal] and ΔF_{760}^{scope}; (C) Fy^{*ssa}_{760} [diurnal + sub-diurnal] and ΔF_{760}^{scope}/PAR. The data presented on the figure correspond to daytime data, SZA $\leq 80^\circ$ and the fraction of the day between 0.2 and 0.8.</i>	60
Figure 18	<i>Mean diurnal variation of ΔF_{760}^{scope} computed for each month.</i>	61
Figure 19	<i>First row: relationships between PRI_{xan}^{scope} and LUE (A), PRI_{xan}^{ssa} [diurnal+sub-diurnal] and LUE (B) and distance correlation (dCor) between the two computed using moving window of 20 days (C). Second row: relationships between F_{760}^{scope} and LUE (D), F_{760}^{ssa} [diurnal+sub-diurnal] and LUE (E) and distance dCor between the two computed using moving window of 20 days (F). Third row: relationships between Fy^{*scope}_{760} and LUE (G), Fy^{*ssa}_{760} [diurnal+sub-diurnal] and LUE (H) and dCor between the two computed using moving window of 20 days (I).</i>	62
Figure 20	<i>Relationship between Fy^{*ssa}_{760} [diurnal+sub-diurnal] and LUE computed for NPQ < 0.1 (A) and NPQ between 0.1 and 2.5 (B).</i>	63

Figure 21	<i>Relationship between fluorescence efficiency (ϕ'_f) and photochemical yield (ϕ_p). The data presented on the figure correspond to daytime data , with PAR values $\geq 500 \mu\text{mol m}^{-2} \text{s}^{-1}$, SZA $\leq 80^\circ$ and the fraction of the day between 0.2 and 0.8.</i>	65
Figure 22	<i>The FloX installed over the winter wheat field in Gebesee, Germany. The photo is taken in the 3^d of June 2019.</i>	69
Figure 23	<i>Site map with distribution of the peak flux footprint. The isolines and colours represent the percentiles of the distribution of the peak flux footprint in a particular sector.</i>	71
Figure 24	<i>Time series of (A) air temperature ($T_{air} [{}^\circ\text{C}]$), (C) vapour pressure deficit (VPD [hPa]), (E) soil water content (SWC [m^3m^{-3}]), (G) photosynthetically active radiation (PAR [$\mu\text{mol m}^{-2} \text{s}^{-1}$]), (I) gross primary production (GPP [$\mu\text{mol m}^{-2} \text{s}^{-1}$]), (B) chlorophyll red-edge index (Clre), (D) light-use efficiency (LUE* [$\mu\text{mol CO}_2 / \mu\text{mol photos of PAR}$]), (F) Photochemical Reflectance Index (PRI),(H) far-red fluorescence ($F_{760} [\text{mW m}^{-2} \text{sr}^{-1} \text{nm}^{-1}]$), (J) far-red apparent fluorescence yield ($Fy^{*760} [\text{sr}^{-1} \text{nm}^{-1}]$) measured over winter wheat during a period from 10th of April until 30th of June 2019.</i>	73
Figure 25	<i>Linear relationships: (A) PRI^{ssa} [seasonal] vs faPAR, (B) F_{760}^{ssa} [seasonal] vs faPAR, (C) $Fy^{*760}_{760}^{ssa}$ [seasonal] vs faPAR, (D) LUE*^{ssa} [seasonal] vs faPAR. Colour-coded with chlorophyll red-edge index (Clre).</i>	74
Figure 26	<i>First row: relationships between PRI and LUE* (A), PRI^{ssa} [diurnal+sub-diurnal] and LUE*^{ssa} [diurnal+sub-diurnal] (B) and distance correlation (dCor) between the two computed using moving window of 20 days (C). Second row: relationships between F_{760} and LUE* (D), F_{760}^{ssa} [diurnal+sub-diurnal] and LUE*^{ssa} [diurnal+sub-diurnal] (E) and distance dCor between the two computed using moving window of 20 days (F). Third row: relationships between Fy^{*760} and LUE*(G), $Fy^{*760}_{760}^{ssa}$ [diurnal+sub-diurnal] and LUE*^{ssa} [diurnal+sub-diurnal] (H) and dCor between the two computed using moving window of 20 days (I).</i>	76
Figure 27	<i>Relationship between $Fy^{*760}_{760}^{ssa}$ [diurnal+sub-diurnal] and LUE*^{ssa} computed for T_{air} between 10° and 25° (A) and T_{air} lower than 10° or higher than 25° (B).</i>	77

List of tables

Table 1	<i>Definition of terms used to describe the geometry of the measurements.</i>	14
Table 2	<i>Data acquisition schemes for diurnal and midday cycles for each canopy.</i>	15
	<i>Negative values of VZA represent the backscatter direction, positive – the forward scatter direction within a plane.</i>	
Table 3	<i>Biochemical and structural characteristics of vegetation targets.</i>	17
Table 4	<i>SCOPE model parameters used to simulate spectro-directional response of F.</i>	17
Table S1	<i>ANIX calculated for F_{760}, F_{687} and sPRI measured in the SPP over chickpea.</i>	35
Table S2	<i>ANIX calculated for F_{760}, F_{687} and sPRI measured in the CPP over chickpea.</i>	36
Table S3	<i>ANIX calculated for F_{760}, F_{687} and sPRI measured in the SPP over grass.</i>	37
Table S4	<i>ANIX calculated for F_{760}, F_{687} and sPRI measured in the CPP over grass.</i>	38
Table S5	<i>ANIX calculated for F_{760}, F_{687} and sPRI measured in the SPP over rice.</i>	38
Table S6	<i>ANIX calculated for F_{760}, F_{687} and sPRI measured in the AR over rice.</i>	39
Table S7	<i>ANIX calculated for F_{760}, F_{687} simulated by SCOPE with the input parameters: SZA = 30°, C_{ab} = 40 ug cm⁻², hc = 0.5 m, lw = 0.05 m, LAI = 1, 3, 5, 7 m² m⁻² and LIDF corresponding to erectophile, spherical and planophile canopy types.</i>	41
Table S8	<i>ANIX calculated for F_{760}, F_{687} simulated by SCOPE with the input parameters: SZA = 30°, C_{ab} = 40 ug cm⁻², LAI = 3 m² m⁻², hc = 0.1, 0.5, 1 m, lw = 0.01, 0.05, 0.1 m, sl = 0.01, 0.02, 0.05, 0.1, 0.2, 0.5, 1 and LIDF corresponding to erectophile, spherical and planophile canopy types.</i>	43
Table S9	<i>ANIX calculated for F_{760}, F_{687} simulated by SCOPE with the input parameters: SZA = 10°, 30°, 45°, 60°, 75°, C_{ab} = 40 ug cm⁻², LAI = 3 m² m⁻², hc = 0.5m, lw = 0.05 m and LIDF corresponding to erectophile, spherical and planophile canopy types.</i>	44
Table 5	<i>Definition of the variables simulated with SCOPE and modelled with SSA.</i>	53
Table 6	<i>Parameters of filterTSeriesSSA (spectral.methods R-package (Jannis V Buttlar, 2015)) function used for the decomposition of PRI_{xan}^{scope}, PRI₀^{scope}, F₇₆₀^{scope}, F₇₆₀^{*scope}, Fy₇₆₀^{*scope}.</i>	55
Table 7	<i>Data quality indices and their corresponding thresholds for which data are retained.</i>	69
Table 8	<i>Parameters of filterTSeriesSSA (spectral.methods R-package (Jannis V Buttlar, 2015)) function used for the decomposition of PRI, F_{760}, Fy₇₆₀[*] and LUE*.</i>	72

Acknowledgements

It always seems impossible until it's done.

Nelson Mandela

This PhD was a great journey, which would not be possible without wonderful people I met on the way.

First, I am deeply thankful to Micol and Cinzia, who led Trustee project and have chosen me among many candidates for this PhD position in Milano. I am grateful to Micol for being always thoughtful and supportive in scientific as well as personal aspects. Thank you for guiding me in these complex research topics and finding just the right solution when is most needed. Cinzia, thank you for your inspiring optimism, for always being there for me and creating a warm atmosphere when I just arrived.

I am happy to have met amazing people of LTDA team. I am grateful to Tommi, who taught me about hyperspectral data and coding in the beginning, and who took me to Majadas for the first time. This was very important to have your support while making the first steps in my PhD. I am also very lucky to have closely worked with Marco. Thank you for being always truthful with me and giving an enormous support in my research work. Thank you for all the adventures we had together. I want to say thank you to: Sergio for always having time to ask how things are going, Biagio for his never-ending inspiring curiosity, Robi G for being patient and tranquil, Robi C for always having something to joke about, Giulia for encouraging me during hard times and laughing together, Javi for being my buddy and being up to a weekend trip in the middle of nowhere, Martina for having nice chats and her help in Grosseto, Ilaria, Francesca, Min and Gabri for being positive and heart-warming.

I was very fortunate to have spent 9 months in Max Planck Institute for Biogeochemistry in Jena. Having the opportunity to work with Mirco and Miguel enabled me to look broader on the remote sensing and ecology in general, and deeper in my research questions. I am grateful to EIES and BAIE groups for hosting me. Special thank you to Javi Pacheco-Labrador who I could always rely on, for giving me timely and comprehensive answers to my million questions and accompanying me in the fieldworks in Gebesee. I want to thank my friends – Sungmin, Lina, Xuanlong – for spending great time on the bike rides across Germany. I never felt lonely being far from family thanks to you.

I want to thank all Trustee members for organizing trainings and summer schools, and fellow ESRs – Dominic, David, Vicente, Maria, Laura, Vikas, Imran, Egor, Geogrios, Daniel, Juan – for making this experience fun.

Thanks to my family and friends, who send me good vibes from far away and for those who always tried to be close. Dad, Masha, Zi, Nastya, Anya, Jenya, Kirill, Sasha, Vanya, Julya, Kondrati, Dasha O. – thank you for believing in me. Thank you to my mom and Ivasha who I survived COVID quarantine with and who supported me in all possible ways. I am grateful to have Anton by my side who offers me caring and unconditional support throughout all the endeavours we embark on together. Спасибо!

Abstract

Photosynthesis is the key process sustaining life on Earth. Accurate prediction of the dynamics of CO₂ exchange between terrestrial vegetation and atmosphere through photosynthesis is crucial for prediction of functioning of Earth's system. The efficiency of photosynthesis under varying environmental conditions is maintained by fast-responding regulatory mechanisms, namely chlorophyll a fluorescence emission (*F*) and non-photochemical quenching (*NPQ*). These processes help to dissipate the excess of energy absorbed by photosynthetic pigments not used for photochemistry. *F* is an electromagnetic radiation emitted at longer wavelengths (640-850 nm) than for excitation. *NPQ* is a complex process which includes the de-epoxidation of xanthophyll cycle pigments resulting in dissipation of excess energy as heat. This translates into changes in leaf absorbance at 531 nm, which can be detected with the photochemical reflectance index (*PRI*). Proximal sensing is a powerful tool for exploitation of subtle signals related to the downregulation of photosynthesis by means of high-spectral and high-temporal resolution spectral measurements. However, *F* and *PRI* are also influenced by canopy structural and biochemical properties, illumination conditions and solar-view geometry, and its explicit interpretation is still challenging.

The aim of my Ph.D. project was to exploit the methods of proximal sensing of vegetation to elucidate a link between continuous hyperspectral measurements of optical indicators related to plant physiology (*F* and *PRI*) and vegetation functioning. Despite rapid proliferation of high-resolution spectroradiometers and increasing interest towards exploitation of time series of *F* and *PRI*, a lot of work remains to be done before these optical signals can be accurately interpreted to unambiguously represent the physiological processes occurring inside a photosynthetic machinery. In the thesis, I focused on using multi-angular observations and high spectral and temporal resolution times series of *F* and *PRI* – both modelled and experimentally acquired.

Multi-angular measurements were used to characterize the anisotropic response of far-red (*F₇₆₀*), red (*F₆₈₇*) fluorescence and *PRI* and to ultimately evaluate the impact of the viewing geometry on these signals under varying solar geometry and structural and biochemical canopy properties. I present an extensive experimental dataset of multi-angular measurements of *F*, *PRI* and *R* collected during a day at canopy-level with a high-resolution spectrometer (FloX, JB Hyperspectral Devices UG, Germany) over four different vegetation targets: Mediterranean grassland, alfalfa, chickpea and rice. Based on the characteristic angular distribution of *F* and *PRI* obtained in the several azimuthal planes (Solar Principle Plane, Cross Principle Plane and the intermediate planes) and varying view zenith angles (VZAs), directional responses of *F₇₆₀*, *F₆₈₇* and *PRI* in horizontally homogeneous canopies are characterized by increased values in the backscatter direction with a maximum in the hotspot and decreased values in the forward scatter direction. Radiative transfer theory and observations agree that the shape of *F* and *PRI* angular response is mostly controlled by leaf inclination distribution function (*LIDF*), while a magnitude and shape of the hotspot peak is sensitive to a combination of factors - leaf area index (*LAI*) and the ratio of leaf width to canopy height. Quantitative evaluation of the impact of anisotropy on

fluorescence apparent yields (Fy^*_{760} and Fy^*_{687}) showed, that, on average, off-nadir observations were overestimated by 20-67% in the backscatter direction and underestimated in other directions by 10-45%. The archived results reinforce the importance of maintaining nadir observation geometry for continuous measurements of F and PRI . Moreover, full characterization of F and PRI anisotropy based on ground-based multi-angular observations can be useful for validation of practical approaches aimed at normalization of directional observations to standard viewing geometry, which can be potentially applied to data acquired at a coarser spatial resolution (i.e. airborne, satellite data).

Additional complexity for the interpretation of time series of optical signal lies in time-scale dependant vegetation dynamics. Here I test the applicability of highly-adaptive time series decomposition technique Singular Spectrum Analysis (SSA) for disentangling slow and fast varying components of vegetation dynamics in time series of F_{760} , Fy^*_{760} and PRI . First, the proof of concept was developed based on spectral and flux half-hourly time series realistically simulated with the Soil Canopy Observation of Photochemistry and Energy fluxes (SCOPE) model parameterized to reproduce the spectral behaviour of a Mediterranean grassland. The simulations included two outputs - featuring and excluding the effect of the xanthophyll cycle de-epoxidation and fluorescence efficiency amplification factor on PRI and F_{760} , respectively. The decomposed slow varying SSA-components of total PRI , F_{760} and Fy^*_{760} showed a good correlation with reference constitutive variability simulated excluding the effect of physiological modulation (PRI_0 , $F_{0,760}$, $Fy^*_{0,760}$). The accuracy of disentangled fast varying SSA-components was validated with the reference physiologically-induced variables (ΔPRI , ΔF), and NPQ and light-use efficiency (LUE). Then, the application of this methodology on a field dataset of spectral and flux time series collected in winter wheat field allowed to significantly improve the correlation of fast components of F_{760} and PRI with the fast component of LUE in comparison with original time series. Therefore, SSA-based approach is a promising tool for decoupling physiological information from continuous measurements of optical signal which can foster the use of automated proximal sensing systems.

Overall, the findings of this project emphasize the importance of careful consideration of the effects of confounding factors on optical signals linked to plant physiological activity. The approach of decoupling slow and fast variability in time series of F and PRI developed here can be potentially applied to time series of remote sensing data acquired from different platforms.

1. Introduction

1.1. Plant Traits and Ecosystem Functional Properties

Over the last decades, especially under the threat of climate change and increasing pressure imposed by human activities, scientific community has been focused on advancing the understanding of interactions between climate and biosphere, mediated by human interventions (Arneth et al., 2010; Heimann & Reichstein, 2008). Terrestrial ecosystem functioning, and land-atmosphere interactions are influenced by the increasing pressure of these changes, therefore, it is important to improve the predictions of biogeochemical cycles of terrestrial ecosystems and ultimately predict the impact on resultant ecosystem service provision. Environmental disturbances translate into modifications of ecosystem functioning properties (EFPs) via the change in the representation of plant traits (PTs) (Lavorel & Garnier, 2002). PTs are the morphological, anatomical, physiological, biochemical and phenological characteristics of an individual plant (Violle et al., 2007). EFPs are defined by Reichstein et al., 2014 as ecosystem-scale quantities “derived from flux and biometric observations, which allow a better characterization and understanding of the ecosystem”. These are often analogous to leaf-level properties, such as water and light-use efficiency (Knauer et al., 2018), light-use efficiency, or light-saturated photosynthetic CO₂ uptake (Kergoat, Lafont, Arneth, Le Dantec, & Saugier, 2008; Musavi et al., 2016), or related to physical and ecohydrological characteristics important for land surface – atmosphere interaction (e.g. aerodynamic and surface conductance, albedo, evaporative fraction). Using complementary information of PTs and EFPs, one can infer variations in key terrestrial ecosystems processes, such as photosynthesis, respiration, and evapotranspiration (Musavi et al., 2015).

1.2. Remote sensing of Plant Traits and Ecosystem Functional Properties

Hyperspectral remote sensing (RS) offers great potential to retrieve PTs and EFPs at spatial scales ranging from leaf and canopy up to ecosystem and global scales, as well as to improve the temporal resolution of the retrieval of vegetation properties. The physical principles behind RS of vegetation are determined by the three main physical mechanisms: absorption, reflection, and transmission of incident radiation (Roelofsen, van Bodegom, Kooistra, & Witte, 2014). Most of the characteristic spectral features of green vegetation are located in the optical domain of the solar radiation (i.e. between 400 and 2500 nm). Reflectance (R) spectra of a green leaf is generally characterized by: 1) strong absorption by photosynthetic pigments in the visible domain (VIS, 400-700 nm), 2) strong R in the near infrared domain (NIR, 700-1300 nm), 3) and water absorption in the shortwave infrared (SWIR, 1300 – 2500 nm). Top of the canopy (TOC) R is determined by the radiative transfer of leaf-level reflected radiance within a leaf and then between canopy elements and background. Mainly, TOC R is affected by canopy structure (e.g. leaf area index, LAI ; leaves orientation), but also by solar-view geometry (directional effects). In RS community, considerable efforts have been made to develop methods for minimizing the confounding effects imposed by solar-view geometry (e.g. Knyazikhin et al., 2013), however, it is still a challenging task. Alternatively, an integrating approach of spectro-directional RS (Schaepman, 2007) can be exploited for combined use of spectral and

directional information for minimizing the directional effects on the one hand, and for maximizing the accuracy of the retrieval of the vegetation traits of interest, on the other hand.

RS can provide information on PTs related to biochemical, structural and functional parameters (Homolová, Malenovský, Clevers, García-Santos, & Schaepman, 2013). Traits commonly retrieved with remote and proximal sensing include chlorophyll and nitrogen content (e.g. Knyazikhin et al., 2013), water content (e.g. Colombo et al., 2008), LAI (e.g. Zheng and Moskal, 2009), leaf mass per leaf area (*LMA*) and specific leaf area (*SLA*) (e.g. Asner et al., 2011), phenology transition date (e.g. Zhang et al., 2003) and species richness (e.g. Rocchini et al., 2010). RS observations were also proved useful for inferring functional aspects of the ecosystem (EFPs). Following the model proposed by (Monteith, 1972) gross primary production (*GPP*) (i.e. assimilation of CO₂) can be expressed as a product of photosynthetically active radiation absorbed by chlorophyll (*aPAR_{Cab}*) and light-use efficiency factor (*LUE*):

$$GPP = PAR \times faPAR_{Cab} \times LUE \quad (1)$$

where *aPAR_{Cab}* is a product of photosynthetically active radiation (*PAR*) (incoming light between 400 and 700 nm) and the fraction of the photosynthetically active radiation absorbed by chlorophyll (*faPAR_{Cab}*). *faPAR_{Cab}* can be determined from RS observations using reflectance-based vegetation indices (VIs), exploiting the red and near-infrared bands in Normalized Difference Vegetation Index, *NDVI* (Tucker, 1979). In a seasonally dynamic biomes (broadleaf forests, grasslands, croplands) VIs have been successfully used to track *GPP*, where *aPAR* largely explains the variability in photosynthesis (Running et al., 2004). While *aPAR* provides insights into structural control on *GPP*, *LUE* represents physiological control on *GPP* under varying environmental conditions. Temporarily resolved estimations of photosynthetic dynamics affected by short-term stress conditions occurring before the degradation of chlorophylls or the monitoring of *GPP* in evergreen vegetation (Wong & Gamon, 2015) are only possible with accurate estimations of *LUE*.

1.3. Optical indicators of plant physiological activity

During the process of photosynthesis, plants aim to assimilate a maximum amount of CO₂ and produce maximum energy in favourable environmental conditions. There are two main stages involved in this process: light reactions and dark reactions. Light reactions involve the absorption of *PAR* by photosynthetic pigments. Most of the *aPAR* is moved from the antenna complexes to the reaction centres of photosystem I (PSI) and photosystem II (PSII) (P700 and P680, respectively), where specialized pigment-protein complexes able to convert the excitation energy into chemical energy. These two photosystems are present in higher plants and act in reverse order, moving electrons from PSII to PSI in a series of reactions that form the Linear Electron Transport (LET) (Porcar-Castell et al., 2014). Dark reactions are characterised by the carbon fixation and production of sugars from atmospheric CO₂. Environmental conditions (light, water availability, temperature) influence these two types of reactions differently and, therefore, the production of chemical energy and its consumption by the carbon reactions do not always conform. Plants evolved different mechanisms to maintain the balance in energy distribution. In fact, absorbed solar light can follow

three alternative pathways: 1) photochemical quenching (*PQ*), where the excitation energy is used for photosynthesis; 2) chlorophyll a fluorescence (*F*), where the energy is re-emitted at longer wavelengths (640-850 nm) than for excitation; and 3) non-photochemical quenching (*NPQ*), where the energy is dissipated as heat (Butler, 1978) (Figure 1). *NPQ* and *F* help keeping the energy balance of the light-absorbing complexes (the photosystems) stable, minimizing the chance of formation of harmful reactive species (e.g. Barber and Andersson, 1992). In particular, *NPQ* and *F* help dissipating the excess *aPAR* that is not used for *PQ*.

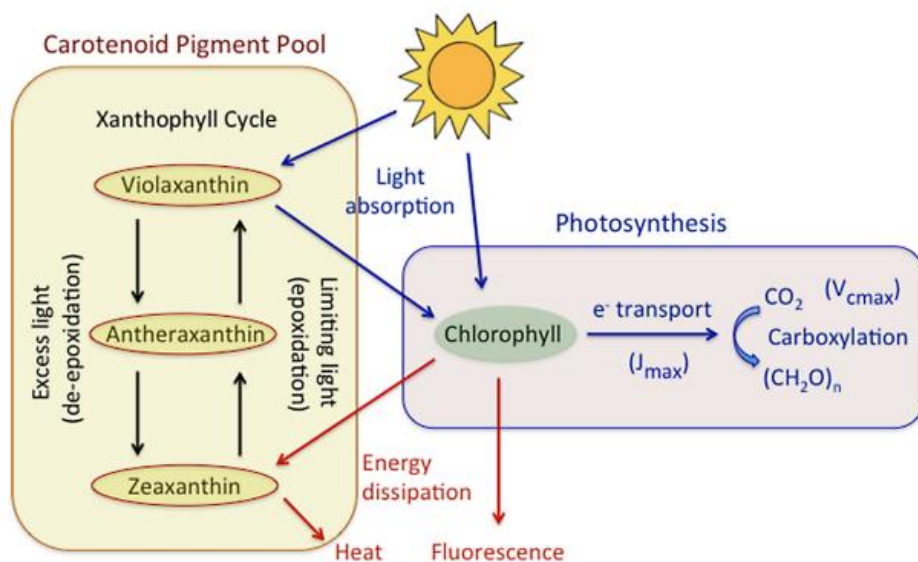


Figure 1. Distribution of absorbed light in a leaf: photochemical quenching, energy dissipation as heat (*NPQ*) and chlorophyll fluorescence (modified from Gamon, 2015).

PQ, *NPQ* and *F* emission are linked to each other in a complex way, particularly under stress caused by abiotic (water deficit, extremely high temperatures, toxic substances) and biotic (species types, photosynthetic capacities) environmental factors. Under low light unstressed conditions, absorbed energy is efficiently used for photochemistry. With the increase of the incoming light energy, the carbon fixation centres become light saturated, which results in increased dissipation of *aPAR* in form of *NPQ* and *F*. However, a quantitative general relationship between these three processes is hard to establish since each component is highly dependent on physiological properties.

F emission spectrum is characterized by two peaks at approximately 685 nm (red region) and 740 nm (far-red region). The two photosystems contribute differently to *F* signal: PSI emits *F* mostly in the far-red region, while PSII contributes to the emission in both the red and far-red regions.

Originally, *F* was explored with active methods based on Pulse Amplitude Modulated (PAM) fluorometry (Baker, 2008). PAM technique involves the use of a measuring light and saturating light and provides a measure of the relative chlorophyll fluorescence quantum yield (ϕ_f) (van Der Tol, Berry, Campbell, & Rascher, 2014). Based on the highly cited study of Genty et al., 1989, photochemical yield (ϕ_p) can be calculated from fluorescence PAM metrics, and, subsequently, photosynthetic electron transport rate can be estimated. Therefore, PAM fluorometry allowed to study the correlation between fluorescence signal and CO₂ assimilation in situ. However, active

fluorometry is mostly restricted to leaf-level observations, while for the monitoring of canopy- and ecosystem level photosynthetic activity remote sensing methods are required.

Passive methods based on retrieval of solar-induced chlorophyll fluorescence (S/F) have been extensively explored during the last decades (Meroni et al., 2009; Mohammed et al., 2019) and are commonly employed on the canopy-level and above. Although S/F is a weak signal, comprising only 1-5% of the reflected radiation, its contribution can be detected by high spectral resolution sensors. The underlying principle in retrieving TOC S/F in observation direction (hereafter F) relies on the exploitation of the regions of the spectrum where the incoming radiation reaching vegetation is low. These include the absorption features: Solar Fraunhofer Lines, where the Sun emission is lower, e.g. the hydrogen absorption band ($H\alpha$, 656 nm); and the two telluric oxygen absorption features in the Earth atmosphere – O_2B (centred at 687 nm) and O_2A (centred at 760 nm). Consequently, the faint F signal can be passively estimated by infilling the absorption features, measuring the extent to which the “wells” are filled with F relative to the reference value. However, the width of the absorption features is a function of illumination conditions, the proportion of direct/diffuse incoming radiation, sun zenith angle, and view geometry. Thus, these conditions have to be properly considered to enable accurate retrievals (e.g. Cendrero-Mateo et al., 2019).

The two main methodologies developed for F estimation from high-spectral resolution ground measurements are the Fraunhofer Line Depth (FLD) and the Spectral Fitting Method (SFM). The FLD method proposed in Plascyk, 1975 and Plascyk and Gabriel, 1975 is the basis of radiance-based approaches. It is simple as it only requires measurements in two adjacent spectral bands: one inside and one outside the absorption feature. The FLD principle assumes that R and F remain constant in the two immediately adjacent measured narrow bands. However, this assumption has been questioned by many researchers (e.g. Alonso et al., 2008; Meroni and Colombo, 2006). Overall, the performance of FLD methods is influenced by the band position, the spectral resolution of the instrument, and the absorption feature characteristics, which are the function of the illumination and observation geometry, as the strength of the atmospheric absorption is related to the atmospheric path length. SFM estimates R and F by spectral curve fitting, based on the assumption that the spectral variations of R and F in the defined spectral range can be described by polynomial or other mathematical functions (Meroni and Colombo, 2006, Meroni et al., 2010). An optimised SFM algorithm (Cogliati, Verhoef, et al., 2015) offers F detection at both O_2 absorption bands with high spectral resolution. Furthermore, the authors extended the SFM approach over the entire fluorescence spectral region introducing SpecFit algorithm (Cogliati et al., 2019).

In the last years, F has been fruitfully used to derive information on photosynthetic activity using ground-based platforms (Yang et al., 2015; Cogliati et al., 2015a; Rossini et al., 2016; Campbell et al., 2019) unmanned aerial vehicles (UAVs) (Zarco-Tejada et al., 2012; Garzonio et al., 2017; Quirós Vargas et al., 2020), airborne (Rascher et al., 2015; Sun et al., 2018; Colombo et al., 2018; Celesti et al., 2018; Tagliabue et al., 2019) and satellite (He et al., 2020; Köhler, Guanter, Kobayashi, Walther, & Yang, 2018; Sun et al., 2018) platforms.

Following the framework of light-use efficiency model (Monteith, 1972), F can be defined as a function of $aPAR_{Cab}$, fluorescence quantum efficiency (ϕ_f) and fluorescence escape probability (f_{esc}) (e.g. Lee et al., 2013):

$$F = PAR \times faPAR_{Cab} \times \phi_f \times f_{esc} \quad (2)$$

F emitted by all leaves is then propagated inside the canopy encountering complex processes of scattering, reabsorption, and re-emission. In particular, F in the red region is highly reabsorbed inside the leaf and the canopy, and potentially re-used for feeding the photosynthetic machinery, while F in the far-red is less reabsorbed and highly scattered (Gitelson et al., 1999). Therefore, a resultant TOC F signal captured by a sensor is significantly modified by the two terms of the equation (2) – $faPAR_{Cab}$ and f_{esc} (Guanter et al., 2014) – which are driven by canopy structural (e.g. LAI) and biochemical (e.g. chlorophyll content, C_{ab}) properties. Significant efforts have been made to estimate f_{esc} using near-infrared R metrics (Yang and van der Tol, 2018; Zeng et al., 2019), and to identify controlling structural parameters affecting f_{esc} (Migliavacca et al., 2017; Martini et al., 2019). However, those methods are not yet universally adopted, and alternative approaches in disentangling variability driven by structural parameters and physiology in TOC F signal should be developed.

A variety of data acquisition levels (from tower-based observations to spaceborne platforms), a diversity of target ecosystems and differences in adopted F metrics indicate that there is an emerging interest in this topic. However, in order to improve the understanding of the link between F and GPP and/or LUE , the dynamics of NPQ and its influence on photochemistry and F should be considered (Porcar-Castell et al., 2014; Frankenberg and Berry, 2018).

During the energy-dependant mechanism of NPQ , when $aPAR$ exceeds the capacity of the photosynthetic reactions, xanthophyll cycle pigments adjust the energy distribution in the photosynthetic reaction centre resulting in dissipation of excess energy as heat (Demmig-Adams & Adams, 1992). The pigment changes associated with xanthophyll cycle de-epoxidation state (Figure 1) affect R at 531 nm. Based on this, the Photochemical Reflectance Index (PRI), derived from reflectance at 531 nm and a reference wavelength (typically 570 nm) has been proposed as an indicator of xanthophyll cycle activity and photosynthetic LUE (Gamon, Peñuelas, & Field, 1992). The link between PRI and LUE was observed for a number of species from proximal (e.g. Filella et al., 1996; Zhang et al., 2015; Alonso et al., 2017), airborne (Rossini et al., 2013; Soudani et al., 2014; Schickling et al., 2016; Middleton et al., 2017) and spaceborne sensors (Drolet et al., 2005; Garbulsky et al., 2013; Stagakis et al., 2014; Middleton et al., 2016). However, PRI is also influenced by seasonally changing chlorophyll-carotenoid ratios, which corresponds to constitutive variability of PRI (Gamon & Berry, 2012). Both changing pigment pools and xanthophyll cycle activity contribute to photoprotection, but they operate over different timescales and their relative contribution to PRI signal has often been unclear. Understanding and disentangling the effects of these factors on different scales is necessary to interpret the PRI dynamics.

1.4. Rationale and research gaps

The Fluorescence EXplorer (FLEX) mission, selected as the European Space Agency's eighth Earth Explorer and planned for launch by 2022, aims to globally measure the F emission from terrestrial vegetation (Drusch et al., 2017). FLEX will, for the first time, enable the terrestrial observation of photosynthesis using an emitted radiance. An advantage of F over traditional reflectance-based methods is its capacity to serve as a pre-visual indicator of stress effects before damage is irreversible and detectable through reflectance measurements. Combining use of F , surface temperature and measurements of changes in the reflectance spectrum associated with NPQ and detectable with PRI will reduce the uncertainty in the quantification of photosynthetic rates.

Within a framework of the FLEX mission, ground-based network of automated proximal sensing systems have been established to gain knowledge about a link between F and R and photosynthesis at canopy scale before these can be upscaled to satellite level (Aasen et al., 2019). These systems are often installed at research station featuring eddy covariance towers and other auxiliary measurements (e.g. Hyttiälä (Zhang et al., 2019) and Majadas de Tiétar (Migliavacca et al., 2017)). Continuous spectral measurements of high temporal resolution in conjunction with flux observations can bring insights into both vegetation long-term slow changes, associated with phenology, as well as vegetation functioning associated with short-term stress events (e.g. heatwaves, Wohlfahrt et al., 2018)). Another level of complexity is introduced by solar-view geometry. On the one hand, solar angles change at diurnal and yearly time scales, and on the other hand, viewing geometry also deviate from nadir in some tower-based set-ups (e.g. Wohlfahrt et al., 2018; Yang et al., 2017). The sensitivity of F and PRI solar-view geometry implies difficulties for the interpretation of data acquired in different locations with different viewing geometry. There have been several initiatives aimed at standardizing acquisition protocols (e.g. EUROSPEC and OPTIMISE COST action (Balzarolo et al., 2011; Pacheco-Labrador et al., 2019)). However, for an accurate interpretation of the time series of spectral data, directional effects imposed both on R and F should be considered. While there are studies aimed at characterization of anisotropic response using multi-angular observations of PRI (Hall et al., 2008; Hall et al., 2011; Hilker et al., 2008; Hilker et al., 2010a; Hilker et al., 2011; Middleton et al., 2009a; Zhang et al., 2015; Zhang et al., 2017; Hilker et al., 2010b; Middleton et al., 2009b; Middleton et al., 2012; Cheng et al., 2010, Cheng et al., 2012) and F (Liu, Liu, Wang, & Zhang, 2016; Elizabeth M. Middleton et al., 2012; Pinto et al., 2017) individually, these have not been explored together aiming to identify the effects of canopy structural properties on the peculiarities of their directional responses. Moreover, the accurate characterization of the directional response is needed for the development of the practical and physically-based approaches (e.g. based on near-infrared reflectance of vegetation (NIRv) and kernel-driven models) for normalizing directional F to a standard viewing geometry.

In order to elucidate a link between spectral observations and photosynthetic rates, it is necessary to develop a robust method for disentangling physiologically relevant information from F and PRI time series. A common approach to extract pigments-driven slow variability of PRI (PRI_0) is based on measurements of dark-adapted leaves or estimation of PRI_0 as an intercept of the relationship between PRI and PAR (e.g. Hmimina et al., 2014). Fluorescence physiological emission is usually

either approximated by fluorescence apparent yield ($Fy^*=F/PAR$) or retrieved through RTM inversions (e.g. Celesti et al., 2018). Time series of optical signals related to plant physiology are affected by processes acting at different time scales - physiological modulation of photosynthesis is mostly associated with short-term stress events, while pigment pools and canopy structure varies at seasonal scale. Thus, it is promising to test applicability of spectral-domain time series analysis methods, such as, for example, Fourier Transform, Empirical Mode Decomposition (Huang et al., 1996), Wavelet Analysis, Singular Spectrum Analysis (Golyandina, Nekrutkin, & Zhigljavsky, 2001). These techniques have been successfully applied to extract time-dependant information from time series of climatic data (e.g. Ghil et al., 2002), and CO₂ fluxes (e.g. Mahecha et al., 2007), however have not been tested on the time series of spectral data. Therefore, it is important to exploit potential of spectral time series analysis, which can expand the applicability of continuous spectral measurements towards accurate estimation of EFPs.

1.5. Objectives

The aim of this Ph.D. project was to exploit proximal sensing data to elucidate a link between continuous hyperspectral measurements of physiological optical signals and vegetation functioning. To reach this aim I addressed the following specific objectives:

- to investigate the directional response of F and PRI and its correlation with R combining field data and radiative transfer simulations with the Soil-Canopy Observation of Photochemistry and Energy fluxes (SCOPE) model (van Der Tol, Verhoef, Timmermans, Verhoef, & Su, 2009) (Part 1);
- to evaluate the impact of the viewing geometry on the time series of spectral measurements of F and PRI and to provide recommendations on geometrical configuration of optical measurement systems for deployment on flux towers (Part 1);
- to test the potential of data adaptive time series decomposition method – Singular Spectrum Analysis (SSA) - to decouple fast variability, attributed to physiological status, and slow variability, attributed to seasonally changing structural and biochemical vegetation properties, of F and PRI in half-hourly SCOPE-simulated time series (Part 2);
- to apply the SSA approach to real spectral data (Part 2).

1.6. Thesis outline

This Ph.D. thesis is organised in two parts, each one presented with its own introduction, material and methods, results, discussion, and conclusions. The analyses presented in this thesis are based on the field multi-angular data collected over four different vegetation targets in Mediterranean grassland (Majadas de Tiétar, Spain) and agricultural field of alfalfa, chickpea and rice (Braccagni, Italy), ground-based high temporal resolution time series coupled with fluxes observations in winter wheat field (Gebesee, Germany), and SCOPE simulations parameterised with the canopy structural traits and meteorological data from Majadas de Tiétar research site.

In Part 1, I present an extensive dataset of multi-angular measurements of F , PRI and R collected with FloX system (JB Hyperspectral Devices UG, Germany) coupled with a goniometer device allowing to collect measurements with a 5° increment in view zenith and azimuth angles (VZA, VAA).

Spectral measurements were collected during a day in the Solar Principal Plane (SPP), Cross Principle Plane (CPP) and intermediate planes. I investigated the effects of canopy structural and biochemical parameters (LAI , $LIDF$, C_{ab}) on the directional response of red (F_{687}) and far-red (F_{760}) fluorescence, fluorescence apparent yields (Fy^*_{760} and Fy^*_{687}), PRI and R . Further, I discuss the implications for the ground measurements and provide recommendation for optimal setup for continuous measurements of F and PRI .

In Part 2, I present a proof of concept of the decoupling of slow and fast temporal dynamics with SSA in time series of physiological optical signals using one year of SCOPE simulated time-series. The evaluation of the methodology was based on the two SCOPE runs – with and without the effect of the xanthophyll cycle de-epoxidation on leaf absorptance simulated with Fluspect-CX module of SCOPE (Vilfan et al., 2018). Similarly, TOC F was simulated featuring and excluding fluorescence efficiency amplification factor (ϕ'_f). Therefore, this allowed to evaluate the SSA-decomposition of PRI , F and Fy^*_{760} against the reference physiologically induced variables (ΔPRI , ΔF) and baseline variables excluding the effect of physiological modulation (PRI_0 , $F_{0,760}$, $Fy^*_{0,760}$). Further, I provide plausible results on the correlation between fast SSA-component extracted from PRI , F_{760} and Fy^*_{760} with LUE . The applicability of the developed methodology was also tested on time series of PRI , F_{760} and Fy^*_{760} covering the whole growing cycle of winter wheat. The outcomes of this study were evaluated against LUE inferred from eddy covariance observations.

In the thesis conclusions, I present the main findings of the Ph.D. project and provide suggestions for future research.

2. Part 1. Effects of varying solar-view geometry and canopy structure on solar-induced chlorophyll fluorescence and *PRI*

Abstract

¹The increasing amount of continuous time series of solar-induced fluorescence (*SIF*) and vegetation indices (e.g. Photochemical Reflectance Index, *PRI*) acquired with high temporal (sub-minute) frequencies is foreseen to allow tracking of the structural and physiological changes of vegetation in a variety of ecosystems. Coupled with observations of CO₂, water, and energy fluxes from eddy covariance flux towers, these measurements can bring new insights into the remote monitoring of ecosystem functioning. However, continuously changing solar-view geometry imposes directional effects on diurnal cycles of the fluorescence radiance in the observation direction (*F*) and *PRI*, controlled by structural and biochemical vegetation properties. An improved understanding of these directional variations can potentially help to disentangle directional responses of vegetation from physiological ones in the continuous long-term optical measurements and, therefore, allow to deconvolve the physiological information relevant to ecosystem functioning. Moreover, this will also be useful for better interpreting and validating *F* and *PRI* satellite products (e.g., from the upcoming ESA FLEX mission).

Many previous studies focused on the characterization of reflectance directionality, but only a handful of studies investigated directional effects on *F* and vegetation indices related to plant physiology. The aim of this study is to contribute to the understanding of red (F_{687}) and far-red (F_{760}) fluorescence and *PRI* anisotropy based on field spectroscopy data and simulations with the Soil-Canopy Observation of Photochemistry and Energy fluxes (SCOPE) model. We present an extensive dataset of multi-angular measurements of *F* and *PRI* collected at canopy-level with a high-resolution spectrometer (FloX, JB Hyperspectral Devices UG, Germany) over different ecosystems: Mediterranean grassland, alfalfa, chickpea and rice.

F_{760} and F_{687} directional responses of horizontally homogeneous canopies are characterized by higher values in the backward scattering direction with a maximum in the hotspot and lower values in the forward scatter direction. The *PRI* exhibited similar response due to its sensitivity to sunlit-shaded canopy fractions.

As confirmed by radiative transfer forward simulations, we show that in the field measurements leaf inclination distribution function controls the shape of *F* and *PRI* anisotropic response (bowl-like/dome-like shapes), while leaf area index and the ratio of leaf width to canopy height affect the magnitude and the width of the hotspot. Finally, we discuss the implications of off-nadir viewing

¹ The content of this part has been published in International Journal of Applied Earth Observation and Geoinformation as Biriukova, K., Celesti, M., Evdokimov, A., Pacheco-Labrador, J., Julitta, T., Migliavacca, M., Giardino, C., Miglietta, F., Colombo, R., Panigada, C., & Rossini, M. (2020). Effects of varying solar-view geometry and canopy structure on solar-induced chlorophyll fluorescence and *PRI*. *International Journal of Applied Earth Observation and Geoinformation*, 89, 102069

geometry for continuous ground measurements. F observations under oblique viewing angles showed up to 67% difference compared to nadir observations, therefore, we suggest maintaining nadir viewing geometry for continuous measurements of F and vegetation indices. Alternatively, a correction scheme should be developed and tested against multi-angular measurements to properly account for anisotropy of canopy F and PRI observations. The quantitative characterization of these effects in varying illumination geometries for different canopies that was performed in this study will also be useful for the validation of remote sensing F and PRI products at different spatial and temporal scales.

2.1. Introduction

In the last decades, the remote sensing community has increased its interest in the study of vegetation physiology. Technical advances have enhanced the capabilities to exploit the subtle signals induced by mechanisms related to the downregulation of photosynthesis (Grace et al., 2007; Coops, Hilker, Hall, Nichol, & Drolet, 2010) by means of solar-induced chlorophyll fluorescence (SIF) and the Photochemical Reflectance Index (PRI). SIF is a part of photosynthetically active radiation absorbed by chlorophyll a ($aPAR$) and reemitted at longer wavelengths (red and far-red). SIF competes with photochemical quenching (PQ) and non-photochemical quenching (NPQ) for the same energy and can be considered as a direct probe of the functioning of the photosynthetic machinery (Meroni et al., 2009; Porcar-Castell et al., 2014; Mohammed et al., 2019). In fact, SIF emission is affected not only by variations in the efficiency of PQ , but also of NPQ . This implies that both SIF and NPQ should be taken into account for getting information on the photosynthetic functioning (Porcar-Castell et al., 2014; Frankenberg and Berry, 2018). Highly sensitive to changing environmental conditions, SIF was employed for monitoring variations in photosynthesis and was proved to serve as a better indicator of vegetation stress than traditional reflectance-based indices (Sun et al., 2015; Rossini et al., 2015; Guan et al., 2016; Yang et al., 2017; Luus et al., 2017; Köhler et al., 2018; Migliavacca et al., 2017; Celesti et al., 2018). NPQ is a regulatory mechanism that helps keeping the energy balance of the light-absorbing complexes stable by dissipating the excess of energy as heat, and thus minimizing the chance of formation of harmful reactive species (Krause and Weis, 1991; Müller et al., 2001). The protection of the photosystems from the photoinhibition takes place in the energy-dependent NPQ and it is associated with the de-epoxidation of the xanthophyll pigments (Demmig-Adams and Adams, 1992), that, in turn, results in a decrease in reflectance at 531 nm which can be assessed with PRI (Gamon et al., 1992; Peñuelas, Filella, & Gamon, 1995).

The link between PRI and light-use efficiency (LUE) (Garbulsky et al., 2011) was observed for a number of species using proximal (Filella et al., 1996; Zhang et al., 2015; Alonso et al., 2017), airborne (Rossini et al., 2013; Soudani et al., 2014; Schickling et al., 2016; Middleton et al., 2017) and spaceborne sensors (Drolet et al., 2005; Garbulsky et al., 2013; Stagakis et al., 2014; Middleton et al., 2016). Similarly, in the last years, SIF datasets have been collected over a number of natural and agricultural vegetation targets using ground-based platforms (Cogliati et al., 2015a; Rossini et al., 2016; Campbell et al., 2019), unmanned aerial vehicles (UAVs) (Zarco-Tejada et al., 2012; Garzonio et al., 2017) and airborne platforms (Rascher et al., 2015; Sun et al., 2018; Colombo et al., 2018). In this context, a substantial input was given by the Earth-Explorer 8 FLorescence EXplorer

(FLEX) satellite mission of the European Space Agency (ESA), the first mission specifically intended for global-scale *S/F* retrieval from space in the red and far-red spectral regions (Drusch et al., 2017). Continuous measurements of fluorescence radiance in the observation direction (*F*) are becoming increasingly available from high spectral resolution devices (Aasen et al., 2019). Among these, the FloX system (JB Hyperspectral Devices UG, Germany) was developed as a ground counterpart for the FLEX optical payload, with intention to gain insights in short-to-long term vegetation processes, and to establish a ground network for validation of the satellite observations (Julitta et al., 2017).

Leaf properties and canopy structure strongly determines the radiative transfer of *F* and *PRI*. Scattering and absorption processes first take place within the leaf and then propagate further throughout the canopy. Within the canopy, the canopy structure (leaf area index (*LAI*), leaf inclination distribution function (*LIDF*) and bidirectional gap fraction) determines multiple scattering and absorption effects between different layers of foliage. Additionally, the canopy structure also influences the *F* and *PRI* values observed under different solar zenith and azimuth angles (*SZA*, *SAA*), view zenith angles (*VZA*) and relative azimuth angles between the sun and the sensor (*RAA*) (Middleton et al., 2012; Van der Tol et al., 2009).

These directional effects do not depend exclusively on the fraction of sunlit and shaded leaves observed with a given field of view (FOV), but are also influenced by the physiological response of each observed leaf to different levels of absorbed radiation (Hall et al., 2008; Hilker et al., 2008). Multi-angular observations from the tower-based spectroradiometer AMSPEC over conifer (Hall et al., 2008; Hall et al., 2011; Hilker et al., 2008; Hilker et al., 2010a; Hilker et al., 2011; Middleton et al., 2009a; Zhang et al., 2015; Zhang et al., 2017) and deciduous species (Hilker et al., 2010b), and field-based system over corn (Middleton et al., 2009b; Middleton et al., 2012; Cheng et al., 2010; Cheng et al., 2012) demonstrated that *PRI* (computed as $PRI = (R_{531} - R_{570})/(R_{570} + R_{531})$), exhibited lower values near the hotspot due to higher fraction of sunlit foliage, where the canopy is exposed to the light-excess condition.

With the proliferation of high-resolution spectrometers, the interest in characterizing *F* anisotropy through multi-angular measurements increased. Middleton et al. (2012) observed that at daily scale *F* retrieved in the O₂-B absorption band (*F*₆₈₇) in corn was insensitive to solar-view geometry, while the directional response of *F* retrieved in the O₂-A absorption band (*F*₇₆₀) varied for the young and the mature crop. In the early growth stage, *F*₇₆₀ increased at high *VZA*, while in the mature canopy *F*₇₆₀ significantly decreased at high *VZA*. Pinto et al. (2017) investigated *F*₇₆₀ directionality of individual leaf surfaces using imaging spectroscopy and stereo imaging in sugar beet, showing that *F*₇₆₀ increased with higher viewing angles. Diurnal multi-angular measurements of *F* in the two absorption bands in winter wheat (Liu et al., 2016) revealed the differences in the shapes of *F* distribution in the Solar Principal Plane (SPP) for *F*₇₆₀ and *F*₆₈₇. These differences were attributed to the dominant processes in the two absorption bands — *F* scattering in O₂-A and *F* reabsorption in O₂-B — as well as to the bidirectional gap fraction.

Most of the ground *R* and *F* measurements have been collected at nadir (Daumard et al., 2010, Cogliati et al., 2015a, Yang et al., 2018). However, when the spectrometers are deployed over high forests, the sensor's fiber optics were usually tilted up to 30° off-nadir to avoid having the tower

structure in the radiometric footprint or to observe a particular part of the canopy (Yang et al., 2015; Yang et al., 2017; Wohlfahrt et al., 2018). This setup has implications for the comparisons of data over time and space, and for potential calibration and validation (Cal/Val) activities. Several initiatives have aimed to identify the scientific requirements for optical measurement systems for deployment on flux towers, such as SpecNet (<http://specnet.info>; Gamon et al., 2006) and the COST actions EUROSPEC (ES0903) (<http://cost-es0903.fem-environment.eu>; Balzarolo et al., 2011; Porcar-Castell et al., 2015) and OPTIMISE (ES1309) (<http://optimise.dcs.aber.ac.uk>; Aasen et al., 2019; Cendrero-Mateo et al., 2019; Pacheco-Labrador et al., 2019). Nevertheless, while the physical processes behind the *F* and *PRI* directionality have been discussed based on modelling (van der Tol et al., 2009; Vilfan et al., 2018) and field observations (Hilker et al., 2008; Liu et al., 2016), the impact of canopy structure and solar-view geometry on both signals simultaneously has not been quantitatively explored.

In this study we measured the anisotropy of F_{760} , F_{687} , and *PRI* during the day with a consistent setup over four vegetation targets characterized by different structure and illumination geometry to address the following specific objectives:

1) to investigate the directional response of *F* and *PRI* and its correlation with *R* combining field data and radiative transfer simulations with the Soil-Canopy Observation of Photochemistry and Energy fluxes (SCOPE) model; 2) to evaluate the impact of the viewing geometry on the time series of spectral measurements of *F* and *PRI* and to provide recommendations on geometrical configuration of optical measurement systems for deployment on flux towers.

2.2. Materials and methods

2.2.1. Spectral data collection and study sites

Multi-angular measurements of *F* and *R* were acquired with the FloX system, specifically designed to retrieve fluorescence in the O₂A (760 nm) and O₂B (687 nm) absorption bands using a high-resolution QE Pro spectrometer (wavelength range of 650 - 800 nm, spectral sampling interval (SSI) of 0.17 nm and full width at half maximum (FWHM) of 0.3 nm), and visible-near-infrared (VIS - NIR) reflectance with the Flame spectrometer (wavelength range of 400 - 950 nm, SSI = 0.65 nm, FWHM = 1.5 nm) (Ocean Optics, USA). Each spectrometer has two channels – one for down-welling irradiance and one for up-welling radiance with a FOV of 25°. Each acquisition cycle consisted of a series of measurements: 1) down-welling irradiance (E^{\downarrow}_1), 2) up-welling radiance (L^{\uparrow}), 3) a second down-welling irradiance measurement (E^{\downarrow}_2), 4) dark current measurement (DC). The second E^{\downarrow}_2 measurement allows accounting for the stability of illumination conditions for the subsequent data quality control.

To perform the multi-angular acquisition, FloX was coupled with a goniometer device with a circular base of 160 cm in diameter and height of 125 cm, allowing to manually vary VZA and view azimuth angle (VAA) with a step of 5° (Fig. 2) (Giardino and Brivio, 2003). The resulting shape of the target footprint varied from a circle with diameter of 55 cm when observed from nadir to an ellipse with a major axis of 92 cm at extreme VZAs. Down-welling irradiance was measured on a calibrated 99% reflective Spectralon panel (Labsphere Inc., North Sutton, NH, USA), which was fixed and leveled on the tripod and placed 2 - 3 m away from the goniometer device at the height of about 1 m.

F_{760} and F_{687} were estimated using spectral fitting methods (SFM) initially proposed by Meroni and Colombo (2006) and Meroni et al. (2010), and further developed by Cogliati et al. (2015b). PRI was computed with the following equation (Gamon et al., 1992):

$$PRI = \frac{R_{570} - R_{531}}{R_{570} + R_{531}} \quad (3)$$

where R_{531} is the reflectance factor of the xanthophyll-sensitive band at 531 nm and R_{570} is reflectance factor of the reference band at 570 nm. With this formulation, PRI values can vary between -1 and 1 and are directly proportional to NPQ . In this study, PRI was scaled ($sPRI$) according to Rahman, Gamon, Fuentes, Roberts, & Prentiss, 2001 in a range from 0 to 1:

$$sPRI = \frac{PRI + 1}{2} \quad (4)$$

In our study, $sPRI$ was chosen to facilitate the comparison of multi-angular observations between different canopies.

Ground spectral measurements were collected in the following horizontally homogeneous canopies (Fig. 2 A - C): 1) semiarid grassland constituted by grasses, forbs and legumes (hereafter referred as 'grass') in a Mediterranean tree-grass ecosystem in Majadas de Tiétar, Spain ($39^{\circ}56'24.68''N$, $5^{\circ}45'50.27''W$) (Perez-Priego et al., 2015), 2) alfalfa (*Medicago sativa L.*) and 3) chickpea (*Cicer arietinum L.*) fields in Braccagni, Italy ($42^{\circ}49'15.36''N$, $11^{\circ}4'40.49''E$). Measurements were also acquired in a row rice canopy (*Oryza sativa L.*) in Braccagni (Fig. 2 D). Diurnal cycles of multi-angular measurements were conducted in Majadas de Tiétar from 20th to 22th of March 2018, and in Braccagni from 5th to 11th of June 2018 and from 8th to 10th of July 2018.

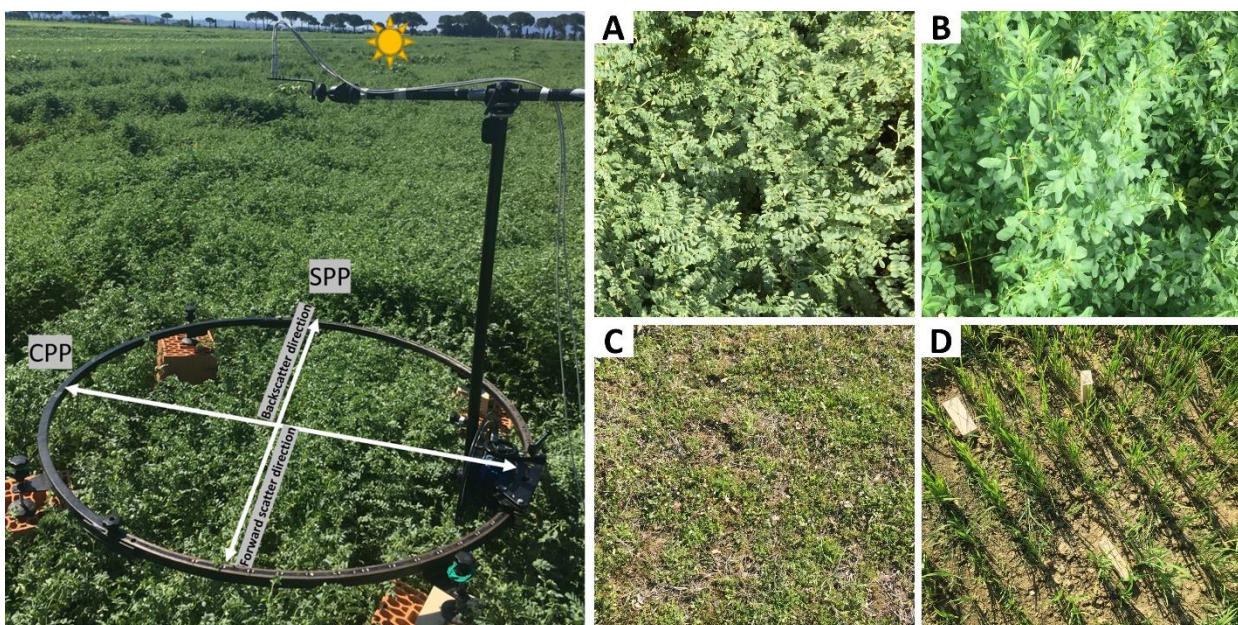


Figure 2. Left panel: multi-angular spectral measurements of chickpea with the FloX system and the goniometer with schematic representation of the solar principal plane (SPP) with its backward and forward scatter directions and cross principle plane (CPP). Right panel: the photographs of studied canopies inside the azimuthal circle of the goniometer device (A – chickpea, B – alfalfa, C – grass, D – rice).

2.2.2. Spectral measurements protocol

2.2.2.1. Protocol to characterize the diurnal cycles of the angular distribution of F , $sPRI$ and R

For the definition of the terms used to describe the geometry of spectral measurements please refer to Table 1.

SZA	Solar Zenith Angle
SAA	Solar Azimuth Angle
VZA	View Zenith Angle
RAA	Relative Azimuth Angle (relative azimuth angle between the sun and the sensor)
SPP	Solar Principal Plane (angular movement of the sensor sits on the same plane of the illumination source and the target)
CPP	Cross Principal Plane (plane normal to the SPP)
AR	Plane parallel to row direction
CR	Plane perpendicular to row direction
Backscatter direction	Direction of reflected radiation scattering opposite to that of the incident radiation
Forward scatter direction	Direction of reflected radiation scattering coinciding with that of the incident radiation

Table 1. Definition of terms used to describe the geometry of the measurements.

To characterize the diurnal evolution of the multi-angular response of F , $sPRI$ and R , we sampled canopy radiance in the SPP, in which the zenith angular movement of the sensor happens in the plane of the illumination source and the target, and the cross principal plane (CPP), which is perpendicular to the SPP along the azimuthal axis. The predominantly sunlit part of the canopy is observed in the backscatter direction of the SPP (hotspot effect), whereas the shaded fraction is mostly observed in the forward scatter direction of the SPP (coldspot effect) (Fig. 2). One acquisition cycle included measurements in two planes – SPP and CPP. For alfalfa and chickpea, the VZA increment was set to 15° resulting in seven observation points from -45° in the backscatter direction to 45° in the forward scatter direction for each plane and a total of 14 observation positions within a cycle. For grass, VZA varied from -50° in the backscatter direction to 50° in the forward scatter direction with a step of 10° and a total of 22 observation positions within a cycle (Table 2). For the rice canopy, we adopted a modified protocol for data acquisition. One acquisition for the row crop

included measurements in the SPP and along the row direction (AR) from -45° to 45° with 15° step. During a day, we collected 12 - 15 acquisition cycles for each canopy. On average, one acquisition cycle took ~15 min with SZA changing from 2° to 3.5°. For the diurnal cycles of alfalfa, chickpea and rice at each observation point we acquired three replicates to estimate uncertainties of the measurements by calculating the standard deviation (σ).

		Chickpea	Alfalfa	Grass	Rice
Diurnal cycles	N of replicates	3	3	1	3
	VZA	-45° to 45° 15° step	-45° to 45° 15° step	-50° to 50° 10° step	-45° to 45° 15° step
	Azimuth planes	SPP, CPP	SPP, CPP	SPP, CPP	SPP, AR
Midday cycles	N of replicates	1			
	VZA	-50° to 50° 10° step			
	Azimuth planes	SPP, CPP, ± 45°		SPP, CPP, AR, CR	

Table 2. Data acquisition schemes for diurnal and midday cycles for each canopy. Negative values of VZA represent the backscatter direction, positive – the forward scatter direction within a plane.

2.2.2.2. Protocol to characterize the angular distribution of F , $sPRI$ and R over the hemisphere

At solar noon, when SZA is at its minimum and changes slowly, we measured several consecutive cycles over four planes starting from the SPP with a step of 45° in azimuth direction and a step of 10° in VZA resulting in 44 data points evenly distributed over the hemisphere for chickpea, alfalfa and grass. For the rice canopy, we collected measurements in the SPP, CPP, AR and across the row direction (CR) with the same VZA intervals (Table 2). On average, one acquisition cycle took 20 min with SZA variation from 0.5° to 1.5°.

2.2.2.3. Measure of anisotropy

For the characterization of F and $sPRI$ response to changing solar-view geometry, we used the anisotropy index ($ANIX$) (Sandmeier et al., 1998) to assess the amplitude of the signal variations within a specific solar plane. Originally, $ANIX$ was defined as the ratio of the maximum and minimum values of reflectance factors. In this study, we adapt the index to F and $sPRI$:

$$ANIX_F = \frac{F_{\max}}{F_{\min}}; \quad (5)$$

$$ANIX_{SPRI} = \frac{SPRI_{\max}}{SPRI_{\min}} \quad (6)$$

Moreover, for the comparison of the multi-angular observations, F , $sPRI$ and R were normalized between 0 and 1 based on minimum and maximum values measured for each canopy, and the difference between the normalized signals most sensitive to physiology (F_{760} , F_{687} and $sPRI$) and reflectance factors of close bands (R_{750} , R_{680} and R_{570} , respectively) was computed. These differences aim to identify physiological effects in the anisotropy since it is expected that one of the two variables paired to produce these differences is affected by plant physiology, whereas the second is expected to be independent or to be much less affected than the first one. The contribution of fluorescence radiance to the reflectance factor is negligible, considering that R_{750} and R_{680} are outside the oxygen absorption bands, and significant divergences might be interpreted as influence of physiology.

To evaluate the impact of the viewing geometry on the long-term time series of F and PRI , we computed daily averages of apparent fluorescence yield (Fy^*) and $sPRI$ acquired with the same viewing geometry. Fy^* was computed as F divided by PAR (W m^{-2}).

2.2.3. Acquisition of biochemical and structural parameters

Biochemical and structural characteristics of vegetation targets are summarized in Table 3. The LAI values of the alfalfa and chickpea plots were measured with the LAI-2000 Plant Canopy Analyzer (LI-COR, USA) device under diffuse illumination sky conditions at low solar elevation to exclude the effects of direct sunlight on the sensor. A single LAI value for each plot was calculated by averaging 5 measurements collected on 3 transects. The LAI value of the rice plot was estimated using hemispherical photos analyzed with the software CAN-EYE (<https://www6.paca.inra.fr/can-eye>). The LAI value of grass was assigned based on the published data at the same experimental site (Migliavacca et al., 2017). The type of $LIDF$ (De Wit, 1965) of each canopy was assigned based on the literature and visual interpretation. Leaf chlorophyll content (C_{ab}) of alfalfa and chickpea was determined spectrophotometrically (V-630 UV-Vis, Jasco, Germany) in a 100% methanol extract at wavelengths 665.2 nm and 652.4 nm, while turbidity was checked by measuring the absorbance at 750 nm and 520 nm. The concentration ($\mu\text{g/ml}$) for C_{ab} was calculated according to empirical equations by Lichtenthaler and Buschmann (2001). C_{ab} of grass and rice samples was estimated following the pigment extraction protocol by Gonzalez-Cascón and Martín (2018). The hot spot size parameter (sl) introduced by Wout Verhoef (1998) in the SAILH canopy reflectance model to describe the hot spot effect for a single layer canopy was computed as the ratio between leaf width (lw) and canopy height (hc) measured in the field:

$$sl = lw/hc \quad (7)$$

Smaller sl factor leads to sharper hotspot peak, while higher sl results in broader hotspot peak (Jupp & Strahler, 1991).

Canopy	Date	LAI (m ² m ⁻²)	LIDF	C _{ab} (μg cm ⁻²)	lw (m)	hc (m)	sl
Chickpea	10/06/2018	8	Planophile	36	0.01	0.85	0.01
Alfalfa	6/06/2018 11/06/2018	7	Plagiophile (Walter-Shea et al., 1997)	39.8	0.009	0.80	0.01
Grass	21/03/2018 22/03/2018	1	Spherical (Migliavacca et al., 2017)	39	0.01	0.10	0.1
Rice	10/07/2018	1.95	Erectophile	27	0.01	0.35	0.03

Table 3. Biochemical and structural characteristics of vegetation targets.

2.2.4. Simulations of spectro-directional response of *F*

SCOPE model (v1.73) was used to characterize the effect of canopy structural parameters (LAI, LIDF, sl), C_{ab} and SZA on spectro-directional *F* response. SCOPE model (van der Tol et al., 2009) is a vertical (1-D) integrated radiative transfer and energy balance model, which calculates radiation transfer in a multilayer canopy in order to obtain reflectance and fluorescence estimations in the observation direction as a function of the solar zenith angle and leaf inclination distribution. The parameters used for SCOPE simulations are reported in Table 4.

Parameter	Value	Unit
Leaf Area Index (LAI)	1, 3, 5, 7	m ² m ⁻²
Leaf width (lw)	0.01, 0.05, 0.1	m
Canopy height (hc)	0.1, 0.5, 1	m
Chlorophyll content (C _{ab})	20, 40, 60	μg cm ⁻²
LIDF types	planophile, erectophile, spherical	
Sun zenith angle (SZA)	0, 15, 30, 45, 60, 75	deg
View zenith angle (VZA)	0, 15, 30, 45, 50, 75	deg
Relative azimuth angles between the sun and an observer (RAA)	0, 30, 60, 90, 120, 150, 180	deg

Table 4. SCOPE model parameters used to simulate spectro-directional response of *F*.

2.3. Results

2.3.1. Diurnal changes of the angular distribution of F , $sPRI$ and R in the SPP, CPP and AR

Figures 3 – 8 show results of diurnal measurements of R_{750} , R_{680} , R_{570} , F_{760} , F_{687} , $sPRI$ and the differences $F_{760} - R_{750}$, $F_{687} - R_{680}$, $sPRI - R_{570}$ as a function of SZA (y-axis) and VZA (x-axis) in the SPP, CPP and AR planes. The values of $ANIX$ computed for F and $sPRI$ are reported in Tables S1 – S6.

2.3.1.1. Chickpea: R , F and $sPRI$ in the SPP and CPP

R , F and $sPRI$ acquired in the SPP over chickpea exhibited a dome-like shape with the highest values measured in the backscatter direction (Fig. 3). The hotspot effect was observed for R , F and $sPRI$. Its location was changing during the day according to the sun position. The highest values of F were recorded in the hotspot during midday cycles (SZA from -30° to 30°). F and $sPRI$ exhibited an asymmetric diurnal course with lower values in the afternoon compared to the morning values measured at nadir under the same SZA. The hotspot effect of R was less pronounced and more localized compared to F and $sPRI$. R increased at higher SZA in the morning and afternoon (SZA = -50° ; 60°) with respect to the noon. Based on the difference between scaled F and R , relatively higher R was observed at high SZA and extreme VZA in the backscatter and forward scatter directions, while F was higher in the middle of the day. The difference $sPRI - R_{570}$ displayed a similar pattern, except for the forward scatter direction, where $sPRI$ exhibited values higher than R_{570} .

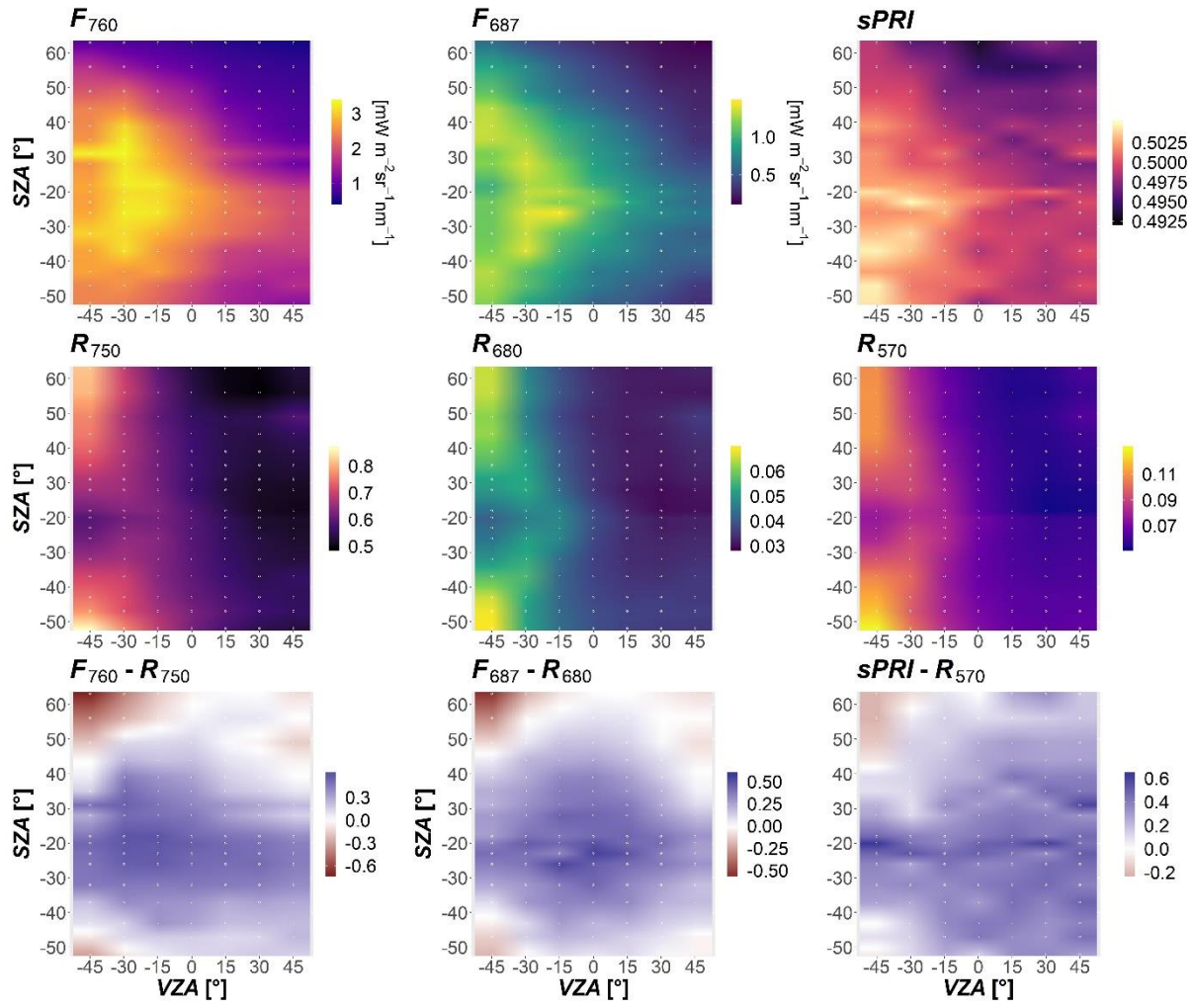


Figure 3. For chickpea in the SPP: the distribution of F_{760} , F_{687} , $sPRI$ (row 1), R_{750} , R_{680} , R_{570} (row 2) and $F_{760} - R_{750}$, $F_{687} - R_{680}$, $sPRI - R_{570}$ (row 3) as a function of SZA and VZA. F , $sPRI$ and R were scaled between 0 and 1 before subtraction. Negative values of SZA correspond to the cycles acquired before midday, positive – after midday. Negative values of VZA represent the backscatter direction, positive – the forward scatter direction within a plane. The points of measurements are marked with white points. The values between the measurements are linearly interpolated.

In the CPP, R , F and $sPRI$ were more evenly distributed and less affected by the viewing geometry compared to the SPP (Fig. 4). A dome-like shape of multi angular F measurements can be observed only around midday (SZA from -30° to 30°) with maximum values measured with a VZA of -15°. Both F and $sPRI$ showed lower values in the afternoon than in the morning at the same SZA. Reflectance factors showed the lowest values in the afternoon when measured with a VZA from -15° to -45°. The differences $F_{760} - R_{750}$ and $F_{687} - R_{680}$ were positive for all SZA and VZA combinations except for a stripe in the afternoon cycles (SZA from 60° to 65°).

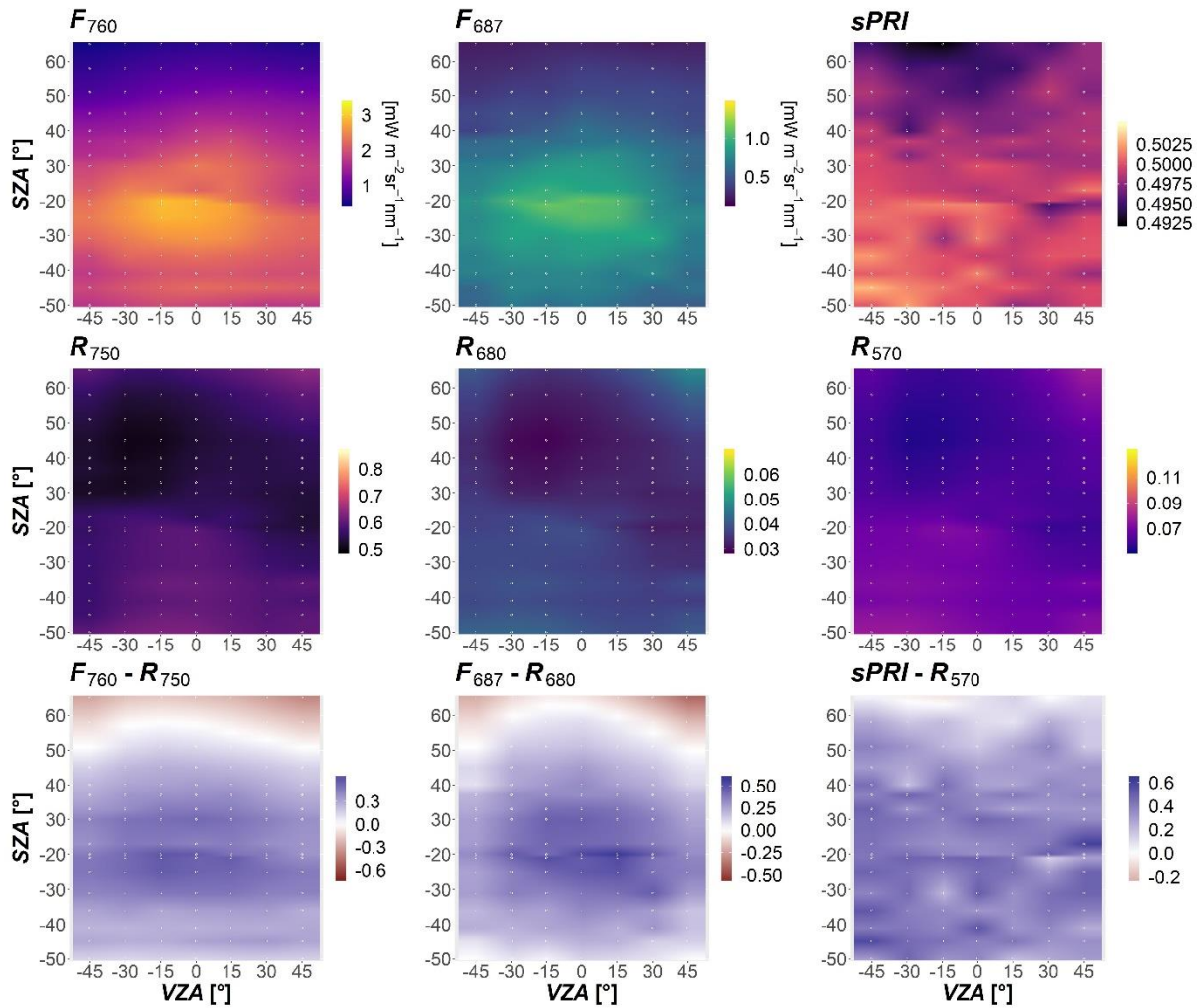


Figure 4. For chickpea in the CPP: the distribution of F_{760} , F_{687} , $sPRI$ (row 1) R_{750} , R_{680} , R_{570} (row 2) and $F_{760} - R_{750}$, $F_{687} - R_{680}$, $sPRI - R_{570}$ (row 3) as a function of SZA and VZA. F , $sPRI$ and R were scaled between 0 and 1 before subtraction. Negative values of SZA correspond to the cycles acquired before midday, positive - after midday. Negative values of VZA represent the backscatter direction, positive - the forward scatter direction within a plane. The points of measurements are marked with white circles. The values between the measurements are linearly interpolated.

2.3.1.2. Grass: R , F and $sPRI$ in the SPP and CPP

The distribution of F_{760} for grass showed a bowl-like shape along the SPP with the maximum values acquired at the extreme VZA in the backscatter direction and with a clear hotspot effect observed at noon ($SZA = -39^\circ$) at VZA between 40° and 50° (Fig. 5). F measured at nadir showed asymmetric diurnal cycle with slightly higher values in the afternoon, while the diurnal course of PAR was symmetrical with respect to solar noon (Fig. S1). The diurnal cycle of $sPRI$ measured over grass exhibited higher values in the morning compared to the afternoon. F_{687} and $sPRI$ exhibited strong fluctuations in multi-angular measurements, however, an increase was observed in the backscatter direction. Reflectance factors displayed a smooth increase from the forward scatter to backscatter direction with the maximum observed at high SZA (-60° ; 60°) and VZA (-50°). The contrasting behaviour of F_{760} and R_{750} were observed early in the morning (SZA from -60° to -50°) and in the evening (SZA from 50° to 60°) under high VZA, when R_{750} exhibited an increase. F_{760} , in turn, showed

relatively higher values around noon and at lower VZA (from -30° to 30°) compared to R_{750} . The difference $F_{687} - R_{680}$ did not reveal a clear pattern due to high intrinsic variability of F_{687} . In comparison to R_{570} , *sPRI* showed stronger variations with higher values in the forward scatter direction.

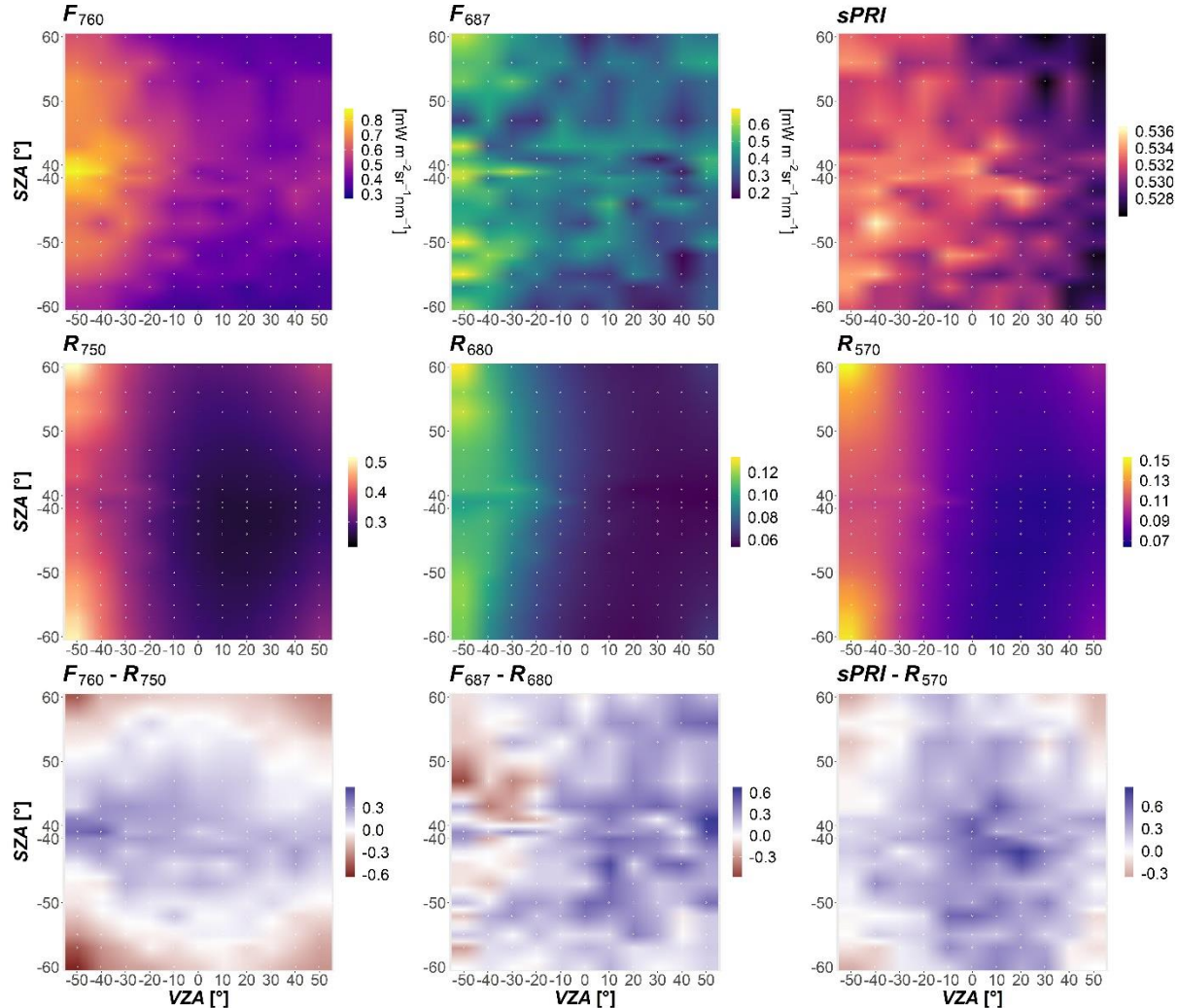


Figure 5. For grass in the SPP: the distribution of F_{760} , F_{687} , *sPRI* (row 1), R_{750} , R_{680} , R_{570} (row 2), and $F_{760} - R_{750}$, $F_{687} - R_{680}$, *sPRI* - R_{570} (row 3) as a function of SZA and VZA. F , *sPRI* and R were scaled between 0 and 1 before subtraction. Negative values of SZA correspond to the cycles acquired before midday, positive - after midday. Negative values of VZA represent the backscatter direction, positive - the forward scatter direction within a plane. The points of measurements are marked with white circles. The values between the measurements are linearly interpolated.

Due to lack of measurements between SZA of 40° and 50° in the CPP, it is hard to analyze the diurnal changes in anisotropy of R , F and *sPRI* over the grass (Fig. 6). Both F_{760} and F_{687} exhibited a bowl-like shape for most of the cycles, while F_{687} was characterized by a slightly higher variability within the plane (Table S3, S4). *sPRI* showed a patchy pattern with a decline towards the forward scatter direction. Reflectance factors showed little angular variation with slightly higher values observed from oblique VZA (-50° ; 50°). The difference between F_{760} and R_{750} showed that R_{750} was relatively higher than F_{760} in the morning (SZA from -58° to -50°) under VZA from 0° to 50° compared to the afternoon.

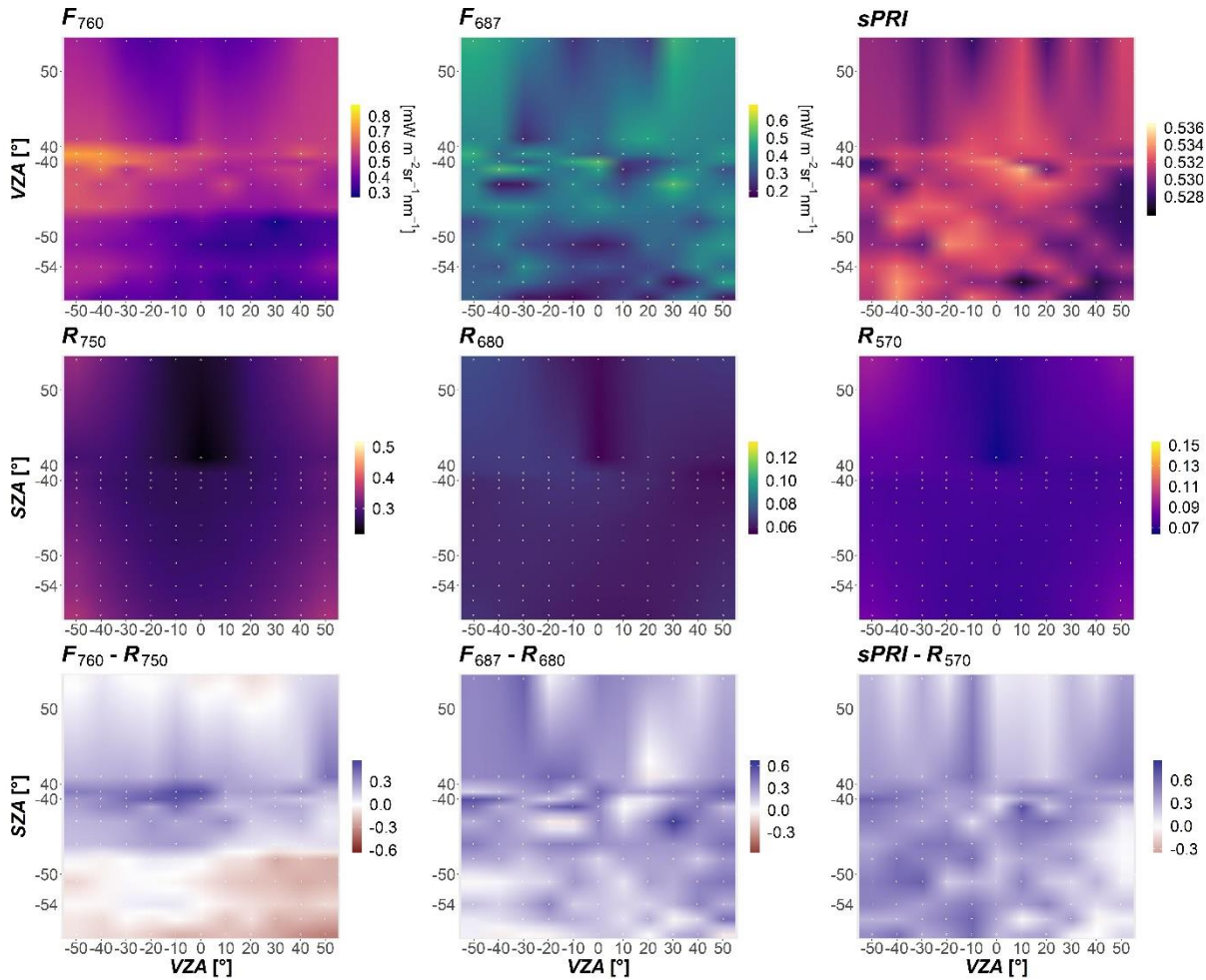


Figure 6. For grass in the CPP: the distribution of F_{760} , F_{687} , $sPRI$ (row 1), R_{750} , R_{680} , R_{570} (row 2), and $F_{760} - R_{750}$, $F_{687} - R_{680}$, $sPRI - R_{570}$ (row 3) as a function of SZA and VZA. F , $sPRI$ and R were scaled between 0 and 1 before subtraction. Negative values of SZA correspond to the cycles acquired before midday, positive - after midday. Negative values of VZA represent the backscatter direction, positive - the forward scatter direction within a plane. The points of measurements are marked with white circles. The values between the measurements are linearly interpolated.

2.3.1.3. Rice: R , F and $sPRI$ in the SPP and AR

The distribution of F_{760} obtained over rice exhibited a similar shape to the one of chickpea in the SPP, with the hotspot in the backscatter direction and the maximum values occurring at noon cycles (SZA from -20° to 30°) at VZA from -15° to -30° (Fig. 7). The angular distribution of F_{687} was heterogeneous, with a general increase towards high VZA in the backscatter direction.

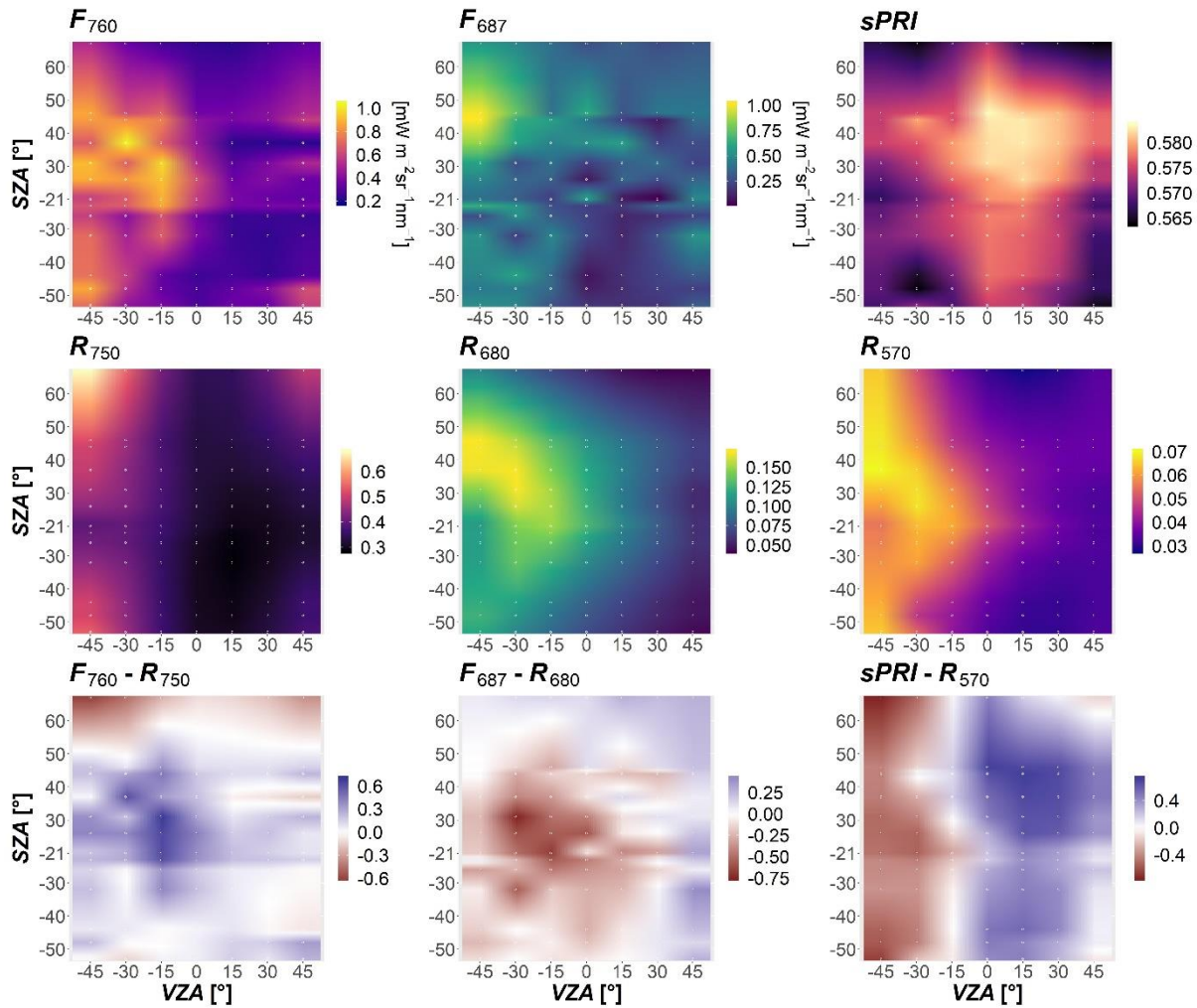


Figure 7. For rice in the SPP: the distribution of F_{760} , F_{687} , $sPRI$ (row 1), R_{750} , R_{680} , R_{570} (row 2), and $F_{760} - R_{750}$, $F_{687} - R_{680}$, $sPRI - R_{570}$ (row 3) as a function of SZA and VZA. F , $sPRI$ and R were scaled between 0 and 1 before subtraction. Negative values of SZA correspond to the cycles acquired before midday, positive - after midday. Negative values of VZA represent the backscatter direction, positive - the forward scatter direction within a plane. The points of measurements are marked with white circles. The values between the measurements are linearly interpolated.

The variation of F_{687} within a plane was generally higher compared to F_{760} , with ANIX changing from 2 to 35 in the SPP (Table S5). The $sPRI$ directional response differed from the ones measured over horizontally homogeneous canopies. $sPRI$ exhibited a dome-like shape with the maximum measured at nadir and in the forward scatter direction, with the highest values in the afternoon (SZA from 30° to 50°). R_{680} and especially R_{570} showed a more distinct hotspot effect than chickpea and grass. R_{750} , in turn, showed a smooth increase from the forward scatter to backscatter direction with maximum values measured at the highest SZA (-50°; 60°) and $VZA = -45^\circ$. The difference between F_{760} and R_{750} revealed that generally F_{760} was relatively higher compared to R_{750} , especially in the backscatter direction. The relative difference $F_{687} - R_{680}$, instead, was negative in the backscatter direction and up to $VZA = 30^\circ$ in the forward scatter direction. $sPRI$ and R_{570} demonstrated contrasting behaviour with their difference being negative in the backscatter at VZA from -15° to -45° throughout the day and positive in the forward scatter direction.

When measured in the AR direction, F_{760} had a less evident hotspot and showed a moderate increase towards higher VZA compared to the SPP (Fig. 8).

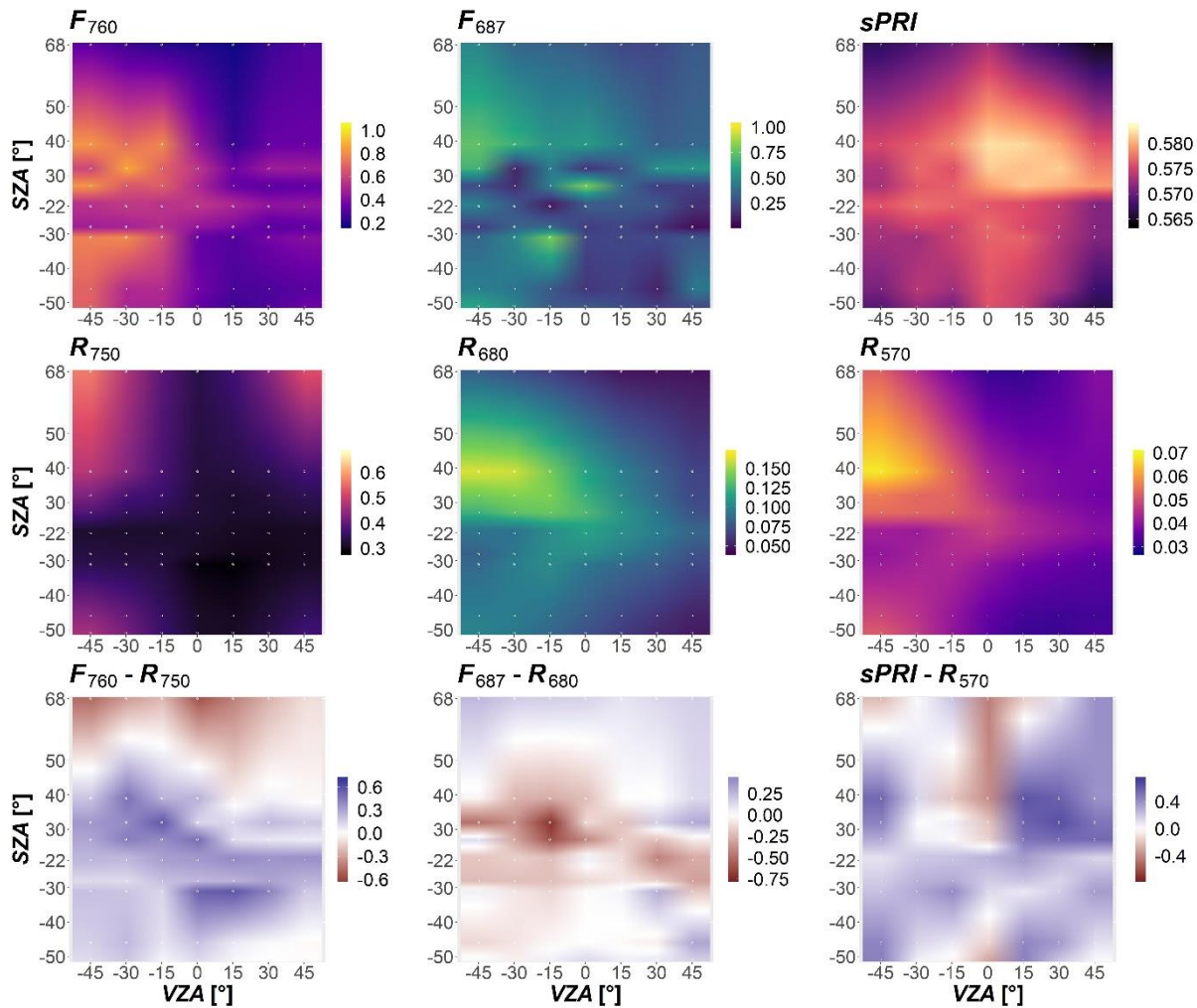


Figure 8. For rice in the AR: the distribution of F_{760} , F_{687} , $sPRI$ (row 1), R_{750} , R_{680} , R_{570} (row 2), and $F_{760} - R_{750}$, $F_{687} - R_{680}$, $sPRI - R_{570}$ as a function of SZA and VZA. F , $sPRI$ and R were scaled between 0 and 1 before subtraction. Negative values of SZA correspond to the cycles acquired before midday, positive - after midday. Negative values of VZA represent the backscatter direction, positive - the forward scatter direction within a plane. The points of measurements are marked with white circles. The values between the measurements are linearly interpolated.

F_{687} exhibited an irregular pattern along the plane with a general increase towards the backscatter. $sPRI$ measured in AR had a similar behaviour to the SPP. Reflectance factors exhibited an asymmetric diurnal cycle with lower values in the morning compared to the afternoon and a maximum found in the backscatter at $SZA = 40^\circ$ for R_{680} and R_{750} and at $SZA = 68^\circ$ for R_{750} . The difference $F_{760} - R_{750}$ was negative in the afternoon at $SZA > 50^\circ$, while at midday and in the morning the positive values prevailed. The difference between F_{687} and R_{680} showed an opposite pattern – negative values in the morning and midday and positive in the afternoon. The difference between $sPRI$ and R_{570} showed an irregular pattern, where $sPRI$ was generally relatively higher at all viewing angles except for a stripe of nadir measurements.

2.3.2. Midday cycles

In homogeneous canopies (chickpea, alfalfa, grass), the angular distribution of both F_{760} and F_{687} measured in four planes resembled the one of reflectance - exhibiting smooth surfaces with gradually increasing values towards the backscatter direction and decreasing towards the forward scatter direction (polar plots, Fig. 9). On the other hand, the angular distribution of F measured in rice canopy showed more complex patterns. An evident stripe of high values parallel to the row orientation was observed in F_{760} distribution, while F_{687} exhibited a bowl-like shape with lowest values measured from nadir and in the backscatter direction at VZA = 20° - 30°.

The highest values of $sPRI$ in chickpea were acquired in the backscatter and the lowest at RAA of 270° in the CPP. Less evident, this pattern was also observed for grass. In alfalfa, the distribution of $sPRI$ showed an irregular pattern, with local increases in the CPP at VZA of 50°, and close to nadir between VZA of 10° and 30°. In rice canopy, there was a pronounced high value stripe along the CPP with the maximum at low VZA (10° - 20°) in the forward scatter direction. The lowest $sPRI$ values for rice were obtained at VZA = 40° - 50°.

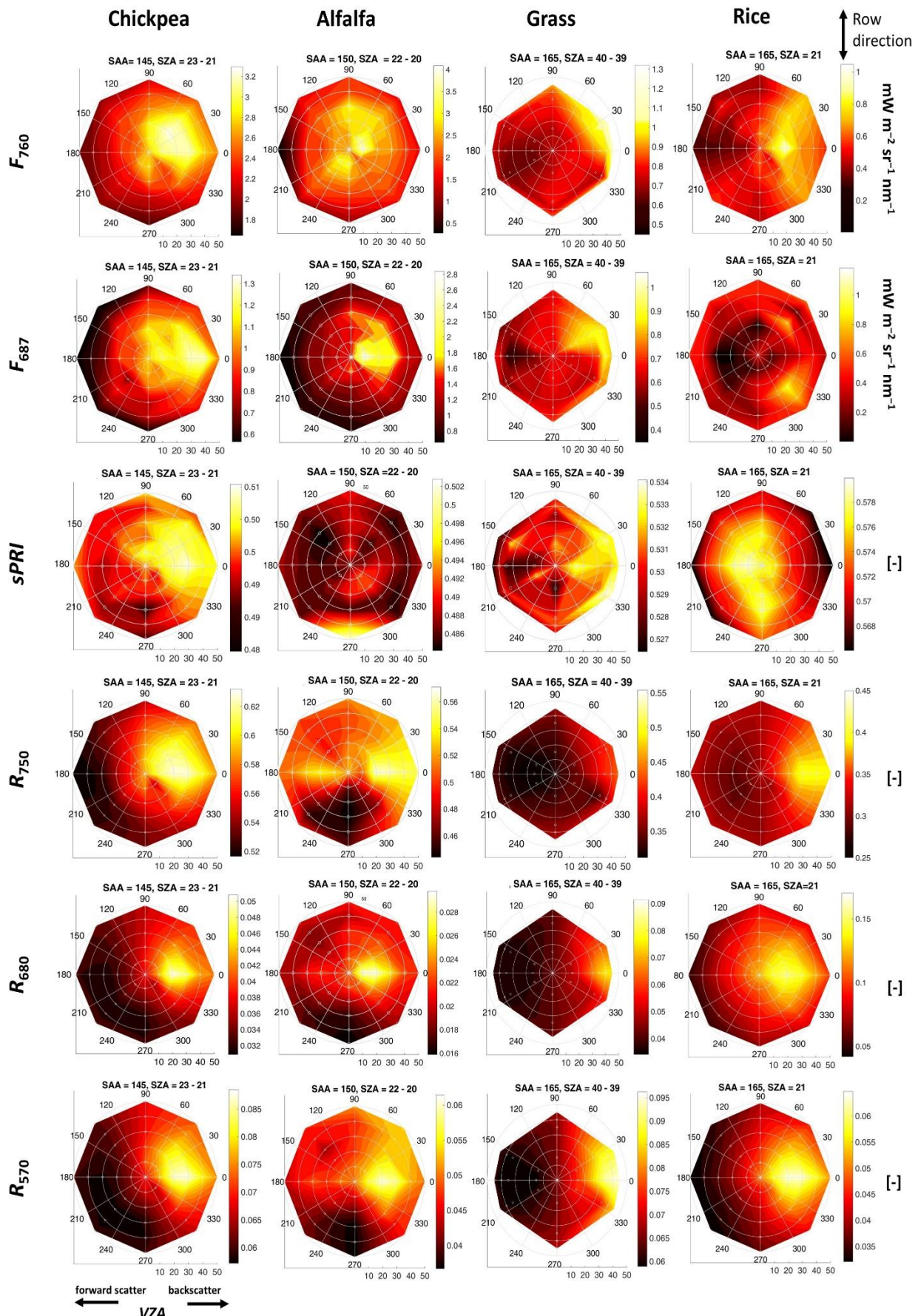


Figure 9. Polar plots of the angular distribution of F_{760} , F_{687} , R_{750} , R_{680} , R_{570} and $sPRI$ measured in chickpea, alfalfa, grass and rice canopies as a function of VZA and RAA.

2.3.3. Effects of canopy structure on F_{760} and F_{687} directional response in the SPP

2.3.3.1. Modelling results

For a fixed SZA SCOPE model showed that the shape of F_{760} and F_{687} directional response in the SPP is mostly driven by $LIDF$ (Fig. S2). In the simulations, F_{760} and F_{687} exhibited a bowl-like shape for erectophile canopy while they show a maximum in the hotspot for planophile and spherical canopy types. F of planophile canopy showed a decrease towards higher VZA, while F of spherical canopy exhibited an increase at extreme VZAs forming a more bowl-like shape (Fig. S2).

For a fixed SZA the model also describes that LAI variations affect the absolute values as well as the shape of the angular distribution of F in the SPP. In simulations of increasing LAI value, the magnitude of the hotspot increased for planophile and spherical canopy types for both F_{760} and F_{687} . For the erectophile type, the F_{760} at $VZA = 0^\circ$ declined with increasing LAI , while there was a clear hotspot effect for F_{687} with $LAI > 3 \text{ m}^2 \text{ m}^{-2}$ (Fig. S3). The highest $ANIX = 4.4$ was observed for F_{687} in the erectophile canopy type with $LAI = 1 \text{ m}^2 \text{ m}^{-2}$. The planophile canopy type was characterized by the smallest $ANIX$ for both F_{760} and F_{687} (Table S7).

SCOPE shows that the width of the region around the hotspot point is driven by the s_l parameter in planophile, spherical and erectophile canopy types for both F_{760} and F_{687} . With decreasing s_l , the hotspot peak became sharper (Fig. S4). For $s_l = 1$, the hotspot effect in F_{760} and F_{687} angular distribution was significantly broadened and smoothed out in the case of erectophile and spherical canopy types. The effect of l_w on the shape of F directional response was negligible for all canopy types. Canopy height variation only affected the amplitude of the hotspot effect in planophile and spherical canopy type, causing the peak levelling off at $hc = 0.1 \text{ m}$.

In SCOPE, SZA also plays an important role in the shape of F directional response (Fig. S5). For planophile canopy type, the hotspot position shifted towards the VZA coinciding with the SZA. For spherical canopy type, with SZA increase, the slope of the angular distribution becomes steeper towards higher VZA. SZA had the biggest impact on the shape of F_{687} directional response for erectophile canopy with $ANIX$ reaching 15.7 at $SZA = 75^\circ$.

2.3.3.2. Comparison between F directional responses of canopies with different structural properties

Both F_{760} and F_{687} directional response for alfalfa and chickpea showed a dome-like shape with maximum values measured in the hotspot at $VZA = 30^\circ$ and $SZA = 22^\circ - 30^\circ$ during the acquisitions (Fig. 10). F measured in alfalfa was higher compared to chickpea. In the forward scatter direction, F_{760} measured in chickpea exhibited a more pronounced coldspot effect decreasing down to $1.06 \text{ mW m}^{-2} \text{ nm}^{-1}$ at VZA of 45° . The F_{760} directional distribution in the SPP measured for grass exhibited a bowl-like shape with steeper increase in the backscatter direction. F_{687} values for grass measured along the SPP were slightly lower, more scattered, and showed an increasing trend from the forward scatter to backscatter direction. F_{760} directional response for rice exhibited a pronounced hotspot, while F_{687} showed a bowl-like pattern with some fluctuations.

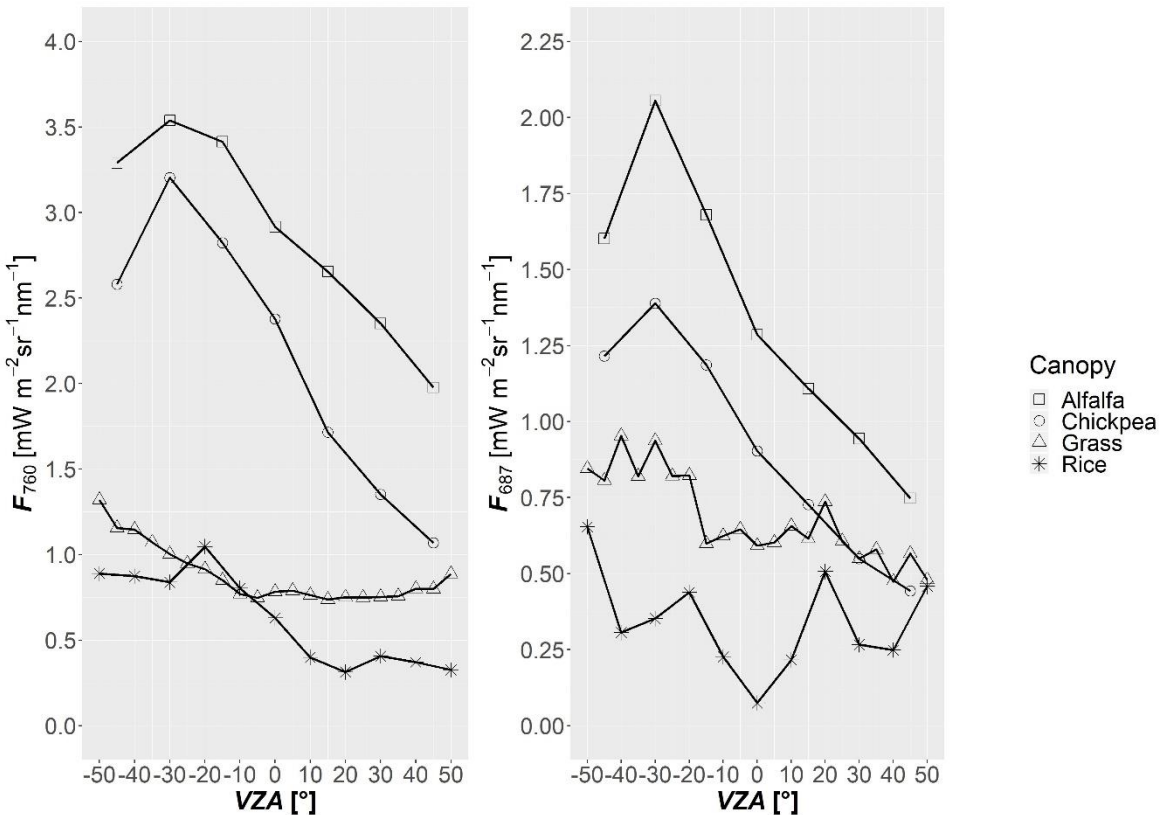


Figure 10. Distribution of multi-angular F_{760} (left) and F_{687} (right) in the solar principal plane (SPP) as a function of VZA for alfalfa, chickpea and rice measured with SZA of 22 - 30° and SAA of 220 - 230°, and grass measured with SZA of 39° and SAA of 184°. Negative values of VZA represent the backscatter direction, positive - the forward scatter direction within a plane.

2.3.4. Fluorescence apparent yield and sPRI daily averages

Fy^*_{760} and Fy^*_{687} were generally higher at lower VZA at all RAA for the chickpea (Fig. 11). The highest values of Fy^*_{760} and Fy^*_{687} were observed at $RAA = 0^\circ$ (hotspot) and the lowest at $RAA = 180^\circ$ (coldspot). Chickpea sPRI also exhibited significant variations at oblique VZA (15° - 45°), characterized by a decrease at $RAA = 180^\circ$ (coldspot) and an increase at 0° (hotspot). Similarly, sPRI showed higher values at lower VZA.

Grass Fy^* and sPRI daily averages exhibited inverse patterns compared to chickpea. The maximum values of Fy^*_{760} and sPRI corresponded to the highest measured $VZA = 45^\circ$. Fy^*_{760} daily average showed its maximum in the hotspot ($RAA = 0^\circ$) and minimum in the coldspot ($RAA = 180^\circ$) for all measured VZAs. Fy^*_{687} daily average increased at $RAA = 0^\circ$ and 270° as well. Interestingly, with higher VZA, Fy^* increase at $RAA = 270^\circ$ became more pronounced. Similar to chickpea, grass sPRI showed the lowest values in the coldspot and increased values in the hotspot direction.

Daily averages of Fy^* and sPRI measured over rice showed the highest variability among the studied canopies. In most cases, the highest Fy^*_{760} values were associated with the hotspot ($RAA = 0^\circ$) and the lowest with the coldspot ($RAA = 180^\circ$). In contrast, Fy^*_{760} signal measured at $VZA = 45^\circ$ showed a distinct decrease at $RAA = 90^\circ$ (CPP) and absolute maximum values with $RAA = 0^\circ$ and 270° . sPRI values measured for rice showed a similar increase at lower VZA than grass but did not vary substantially as a function of RAA.

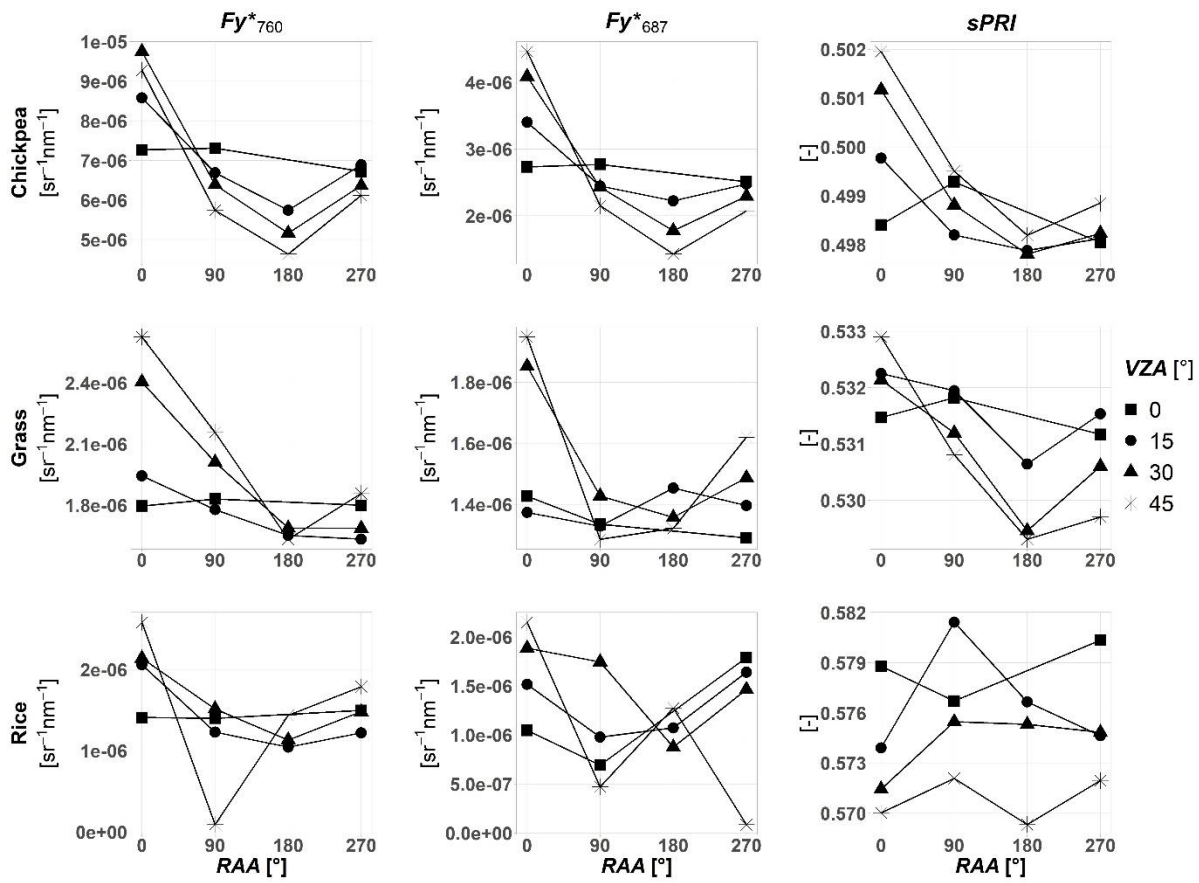


Figure 11. The daily average values for Fy^*_{760} , Fy^*_{687} and $sPRI$ obtained at four VZAs (0° , 15° , 30° , 45°) with four RAAs (0° , 90° , 180° , 270°) for chickpea (row 1), grass (row 2) and rice (row 3).

2.4. Discussion

2.4.1. Fluorescence and $sPRI$ anisotropy as a function of solar-view geometry

Different crops showed diverse shapes of F , $sPRI$ and R angular distribution as an effect of canopy structure and leaf orientation in varying illumination conditions during the day. In particular, the asymmetric diurnal course of both F and PRI with respect to solar noon does not always suggest a larger photosynthetic stress in the afternoon (Rascher et al., 2009; Paul-Limoges et al., 2018) as it would be expected (Fig. S1). This fact can be partly attributed to local changes of the portion of sunlit and shaded leaves inside the canopy induced by changing SZA during a day (Damm et al., 2015). Moreover, in the case of chickpea, this behaviour might be partly driven by slightly lower PAR values in the afternoon compared to the morning (considering the same SZA) (Fig. S1). Regarding the effects of varying viewing geometry, the anisotropic response of F can be explained by changing canopy depths, from which the photons escape the canopy in the direction of the sensor. When measured under high VZA, the sensor captures the signal mostly from the upper sunlit canopy layers and less from deep shaded layers. The canopy structure controls the scattering and absorption of the light inside the canopy (Knyazikhin et al., 2013), resulting in contrasting F directional responses for different canopies (Fournier et al., 2012; Damm et al., 2015). For homogeneous canopies, F_{760} in the SPP is higher in the back- than in the forward scatter direction with a dome-like shape in chickpea and a bowl-like in grass (Fig. 3, 5). F_{687} has a similar shape to F_{760} with higher variability (higher AN/X). This higher variability can be attributed to the prevailing reabsorption processes in

the red than in the far-red region (Gitelson et al., 1999; Buschmann, 2007; Porcar-Castell et al., 2014). F and R anisotropy responses are more coordinated in the SPP, where the backscatter and forward scatter directions are characterized by stronger differences in observed sunlit-shaded fraction than other planes. However, in the case of chickpea and grass, R tends to have higher hotspot values in the evening and morning compared to midday, while the hotspot values of F are the highest at midday (Fig. 3, 5). This contrasting behaviour might be due to the different nature of these two signals. R is a relative metric of scattered radiance normalized by the incoming one. Its anisotropy is purely driven by the radiative transfer of the light scattered by the leaf and within the canopy (which tends to maximize under extreme SZAs and VZAs due to volumetric scattering; Roujean, Leroy, & Deschamps, 1992; Sandmeier et al., 1998). Contrarily, F is an absolute variable in part proportional to the amount of incoming radiance, for this reason, F maximizes at solar noon, when down-welling radiance is also maximum.

F anisotropy is less pronounced in the CPP compared to SPP, as the sunlit-shaded fraction of observed leaves varies less due to solar-view geometry. Although for chickpea F_{760} values measured from oblique VZA in the CPP do not deviate a lot from the values acquired from nadir, we observed a peculiar increase at VZA between 5 and 25° and SZA of 20° and 26° (Fig. 4). This increase could be attributed to the planophile structure of chickpea, characterized by an average leaf angle (ALA) of 26° (Zarco-Tejada, 2000). In this case, the sun light is perpendicular to the ALA, resulting in a higher proportion of sunlit leaves observed by the sensor under the corresponding solar-view geometry.

For chickpea, the decrease of R in the CPP in the afternoon (Fig. 4) might be due to the differences in height within the canopy, casting shadows in this area. While the R response was evident, F did not decrease significantly, which suggests F is less affected by the local geometric effects inside the canopy. This might be explained by the fact that F signal at leaf-level is characterized by isotropic emission (Yang and van der Tol, 2018), which in some cases might result in a less strong angular response than R . Moreover, the link between the incoming radiance and the F emission is mediated by the different physiological state of the leaves in the shaded/illuminated portions of the canopy.

For the homogenous canopies (chickpea and grass), $sPRI$ directional response in the SPP is characterized by a decrease in the forward scatter direction and an increase in the backscatter direction (Fig. 3, 5). Such variability is driven by the dominance of sunlit leaf fraction observed in the backscatter direction, where photoprotective mechanisms activated under higher light intensity cause higher $sPRI$ values (Gamon et al., 1992) compared to the values measured in the forward scatter direction with higher shaded fraction. These results are consistent with the previous research on PRI directional response in coniferous forests (Hilker et al., 2008; Hall et al., 2008, Zhang et al., 2015; Zhang et al., 2017) and in cornfields (Middleton et al., 2012; Cheng et al., 2010; Cheng et al., 2012). Midday $sPRI$ values acquired from nadir conform with typical values associated with high light conditions found in literature (from 0.45 to 0.5; Rossini et al., 2010; Perez-Priego et al., 2015; Schickling et al., 2016).

For rice, F variability within the SPP was particularly strong (Table S5) due to the high contrast between nadir and off-nadir observations determined by the erectophile canopy type. At VZA = 0° the reflected radiance mostly originates from the less illuminated canopy levels, while with

increasing VZAs the contribution of well-illuminated top layers of vegetation to the signal proportionally increases (Sandmeier et al., 1998). When the sun elevation increases, the hotspot effect of F_{760} becomes more distinct; however, its position does not always correspond to SZA (Fig. 7). The shift of the hotspot to lower VZA (15° - 30°) observed for several cycles (Fig. 7) can be attributed to complex interactions between canopy leaf angles and observation geometry, resulting in the maximum of vegetated fraction within the footprint.

When observing the canopy along the row direction, the general increase of F in the backscatter direction is preserved (Fig. 8), which can be explained by a higher probability of having more sunlit fraction observed through the space between rows (Zhao et al., 2010). Lower deviation of F_{760} from nadir values in the AR plane under high sun elevation ($SZA = -22^\circ$) might be explained by the fact that erectophile canopy does not receive direct light on the leaf surface that much, and, therefore, directional effects are significantly reduced. The distribution of $sPRI$ along the SPP and AR measured over rice exhibited a dome-like shape (Fig. 8), which is driven by the lower fraction of vegetation observed from nadir in an erectophile canopy and the contribution of soil to the reflectance signal (Barton and North, 2001), while the sunlit-shaded fraction controls the shape of the $sPRI$ directional response less evidently.

In this work, we measured the reflectance and fluorescence from the top canopy layer, expected to be the one contributing the most to the measured F signal (Van Wittenberghe, Alonso, Verrelst, Moreno, & Samson, 2015). Due to the complexity of the measurement setup, we could not measure the light distribution and the reflectance/fluorescence for different layers inside the canopy. This would have been useful to characterize the physiological response of the different leaves to different levels of radiation; and potentially to better explain the anisotropic behaviour at the top of the canopy. In future campaigns, leaf-level reflectance/fluorescence measurements for different canopy layers, by means of (e.g.) the FLUOWAT leaf clip (Van Wittenberghe et al., 2015) should be performed as well, close in time to the multi-angular measurements.

2.4.2. Effects of structural parameters on fluorescence directional response in the SPP: comparison between observations and simulations

SCOPE forward simulations were useful to disentangle the driving factors of F anisotropy in the different crops. Both modelling and experimental results demonstrated that planophile (chickpea), plagiophile (alfalfa) and spherical (grass) canopy types have similar F directional response, while the erectophile canopy type (rice) significantly differs. The spectro-directional outputs of the SCOPE model showed F distribution characterized by a bowl-like shape with a deep decrease at $VZA = 0^\circ$ for the erectophile canopy (Fig. S2). This agrees with the results on bidirectional response of F_{760} in winter wheat (Liu et al., 2016), driven by the presence of high amount of soil fraction, which is mostly visible from nadir and diminishes with higher VZAs. Measurements of bidirectional radiance over rice were complicated by the row structure (Zhao et al., 2015), which, together with relatively wide FOV, might have contributed to the asymmetrical shape of F_{760} directional response, characterized by shifted minimum values towards coldspot in the forward scatter direction (Fig. 10).

The angular distribution of F for spherical canopy type also shows a bowl-like shape but with lower anisotropy factor and an evident hotspot in the backscatter direction for $LAI > 3 \text{ m}^2 \text{ m}^{-2}$ (Fig. S3). For

grass (spherical), instead, we observed a well-defined bowl-like shape of F_{760} distribution, but no hotspot (Fig. 10). The absence of the hotspot can be explained by relatively high sI (0.1) and low LAI ($1 \text{ m}^2 \text{ m}^{-2}$), which minimized the width and the magnitude of the hotspot.

Directional responses of F measured for alfalfa (plagiophile) and chickpea (planophile) are similar to each other (Fig. 10). This can be explained by comparable LAI ($7 - 8 \text{ m}^2 \text{ m}^{-2}$) and sI (0.01). The shape of the F distributions for these species conforms to the modelling results (Fig. S3), however, the measured hotspot is wider than the modelled one due to the averaging effect of the sensor's FOV, which integrates the signal over 25° rather than in an infinitesimal solid angle as in SCOPE (Schaepman-Strub, Schaepman, Painter, Dangel, & Martonchik, 2006). Considering variability within a plane, field observations showed higher $ANIX$ compared to modelling results (Table S1, S9) affected by quicker decrease in the forward scatter direction (Fig. 10). F_{687} directional response for alfalfa and chickpea canopies, which are similar in C_{ab} and LAI , exhibited higher difference in absolute values and specifically in the hotspot compared to F_{760} . Having a little higher C_{ab} and a little lower LAI , one would expect to observe lower or identical values for F_{687} for alfalfa compared to chickpea due to F_{687} reabsorption. However, the results showed higher values of F_{687} for alfalfa, which might be explained by its heliotropic leaf movements (Walter-Shea et al., 1997; Strub et al., 2003) resulting in high amount of sunlit leaves, especially in the backscatter direction of the SPP.

2.4.3. Fluorescence apparent yield and $sPRI$ daily variations as a function of VZA and RAA: Implications for the ground measurements

In this work we performed a quantitative evaluation of the impact of anisotropy on Fy^* and $sPRI$. We found, that for the homogenous and mature canopies of planophile type (chickpea) off-nadir acquisitions result in lower Fy^* at all RAAs except the backscatter direction in the solar principal plane ($RAA = 0^\circ$), where Fy^* increased by 20 - 67% compared to nadir acquisitions. For all other RAAs ($90^\circ, 180^\circ, 270^\circ$), Fy^* values measured with the sensor's inclination of 15° decreased by 3 - 20%. With an increase of observation angle ($VZA = 30^\circ - 45^\circ$), Fy^*_{760} decreased by 10 - 35% and Fy^*_{687} by 10 - 45%. The same pattern was observed for $sPRI$, where the biggest discrepancies occurred in the backscatter direction of the SPP at high VZA. Therefore, an optimal setup for continuous measurements of F and PRI should have a nadir VZA in order to minimize the directional effects, with an acceptable inclination of up to $5 - 10^\circ$, which, in the case of F signal measured over grass (spherical canopy type), results in less than 3% difference. Balzaro et al. (2011) suggested using oblique viewing angles to increase the footprint of the measurements of vegetation reflectance, however, based on the current analysis we do not recommend adopting this strategy for continuous F measurements. For tower installation we foster the use of a sufficiently long horizontal arm that can carry the optical fibers at the necessary distance from the tower structure. When this would not be possible, a correction scheme for the signal directionality should be considered.

Multi-angular observations, like the ones presented here, can help building or validating these correction schemes (e.g. based on near-infrared reflectance of vegetation (NIRv) and kernel-driven models), as well as properly interpreting remote observations taken under varying solar-view geometries (e.g., at different latitudes within a satellite orbit). Moreover, multi-angular measurements can provide a complete characterization of F signal and help to acquire meaningful F values in the case of, for example, sparse canopy of erectophile type, when nadir observations are

confounded by a significant portion of soil background. Nevertheless, the deployment of field goniometers is demanding and limited to relatively short canopies. In this regard, continuous observations by means of automated, tower-based scanning systems (Leuning, Hughes, Daniel, Coops, & Newnham, 2006; Hilker et al. 2007; Corp et al., 2010) may complement nadir-looking systems towards a complete characterization of the canopy reflectance and fluorescence signals.

2.5. Conclusions

In this study we present a unique dataset of multi-angular observations of F , R and $sPRI$ over four different vegetated targets measured in two main planes — the SPP and the CPP — during a day, as well as the angular distribution of F , R and $sPRI$ over the hemisphere at midday, coupled with SCOPE simulations of spectro-directional response of F under varying structural and biochemical parameters.

Radiative transfer theory and observations agreed that the shape of F bidirectional distribution is controlled by $LIDF$: a bowl-like shape with a deep decrease at nadir is typical for erectophile canopy type, a smooth bowl-like shape for spherical canopy with $LAI < 3 \text{ m}^2 \text{ m}^{-2}$, a dome-like shape with a pronounced hotspot for planophile canopy type. The magnitude and the shape of the hotspot is controlled by LAI and sl : a combination of low sl and high LAI determine a stronger and more pronounced hotspot effect. Both F and $sPRI$ showed significant directional variability for all the studied canopies, with the highest $ANIX$ of F within the SPP observed for rice. F_{687} is characterized by higher anisotropy compared to F_{760} due to prevailing re-absorption process in this spectral region. The $sPRI$ directional response is characterized by an increase in the backscatter direction and a decrease in the forward scatter direction driven by different contribution of sunlit-shaded fractions of vegetation to the measured signal.

Overall, for homogenous canopies, off-nadir measurements resulted in lower values of F and $sPRI$ compared to nadir observations, at all RAAs except in the backscatter direction in the SPP, where, on the contrary, the values were higher. Based on a quantitative evaluation of the impact of canopy anisotropy and solar-view geometry on F and $sPRI$ spectro-directional response, we recommend maintaining nadir viewing geometry in automated proximal sensing systems, with an acceptable inclination up to 5 - 10°. Nevertheless, UAV, airborne and satellite observations may be forced by design to observe the target at higher VZAs, and under different illumination conditions (i.e. different SZAs). In order to properly account for the effects of the canopy anisotropy on F and PRI observations, a proper correction scheme should be developed and tested against multi-angular measurements.

The results presented in this study demonstrate that the anisotropic response of F and $sPRI$ and the corresponding R do not totally covary and that the angular configuration plays an important role in relative contribution of F and $sPRI$ compared to reference R . The analysis of differences between physiologically relevant signals (F_{760} , F_{687} and $sPRI$) and reflectance factors of close bands (R_{750} , R_{680} and R_{570} , respectively) showed that the contribution of the physiological component is relatively higher in homogeneous canopies (i.e. chickpea and grass) under all SZA and VZA combinations except extreme angles ($>50^\circ$). This suggests, that when measured under hight SZA, physiological information contained in F and PRI might be masked out by directional effect.

The characterization of these anisotropic responses along the daily cycle (i.e., under varying SZA and SAA) may also prove useful for evaluating the plant response to the different relative illumination conditions that appear along long-term time series, within a satellite orbit, or in general for different geographical locations and times within a validation framework.

2.6. Supplementary material

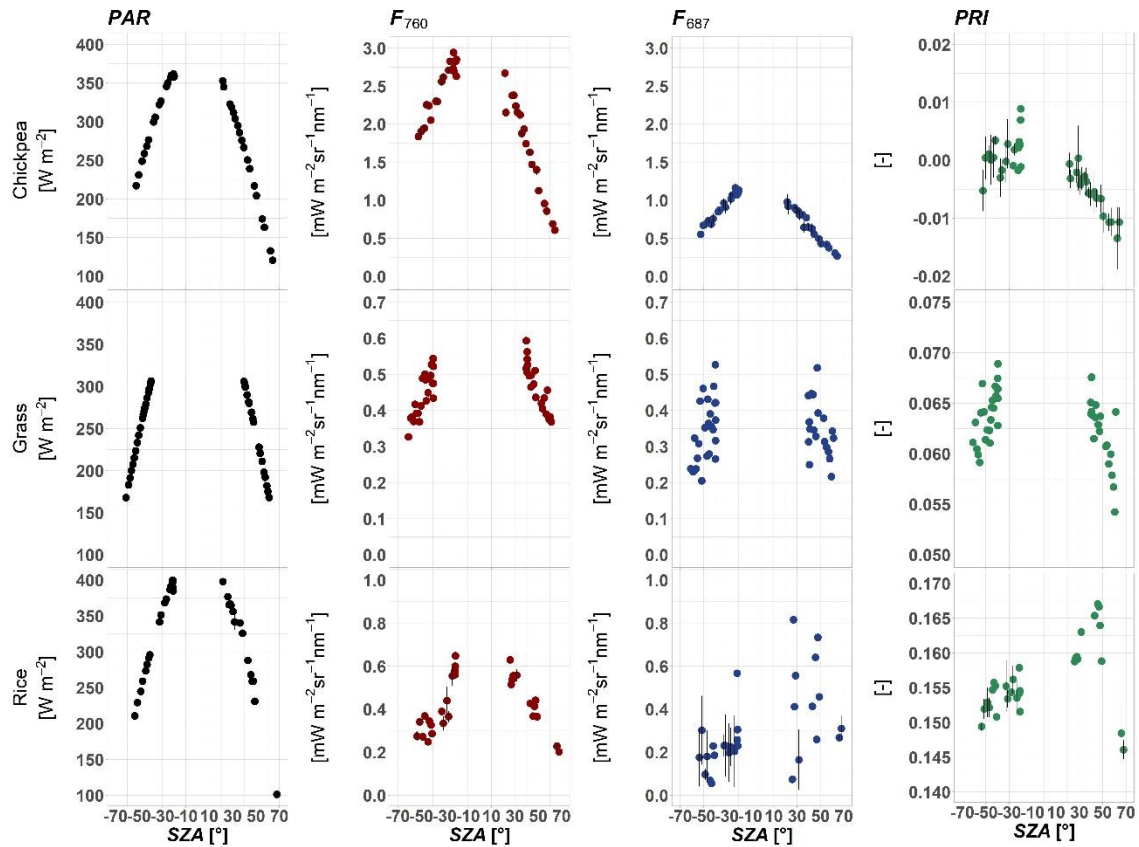


Figure S1. Diurnal cycles of PAR, F_{760} , F_{687} and PRI acquired from a nadir-viewing direction for chickpea (row 1), grass (row 2) and rice (row 3). Error bars for chickpea and rice indicate standard deviation ($n = 3$). Measurements over the grass were collected as a single acquisition ($n = 1$). Negative values of SZA correspond to the cycles acquired before midday, positive - after midday.

SZA (°)	F_{760_ANIX}	F_{687_ANIX}	$sPRI_ANIX$
-52	1.968	3.862	1.0279
-47	1.770	3.224	1.0258
-43	1.734	2.730	1.0166
-37	1.776	2.347	1.0253
-32	1.635	2.450	1.0215
-26	1.649	2.152	1.0175
-23	1.660	2.266	1.0298
-20	1.671	2.345	1.0279
22	1.942	2.216	1.0204
28	2.999	3.135	1.021
31	2.468	3.555	1.0226
35	3.255	4.198	1.0198
39	3.626	4.320	1.0205
44	3.048	4.354	1.0179
49	2.835	4.205	1.013
56	2.536	4.702	1.0197
63	1.930	4.397	1.0227

Table S1. ANIX calculated for F_{760} , F_{687} and sPRI measured in the SPP over chickpea.

SZA (°)	F_{760_ANIX}	F_{687_ANIX}	$sPRI_ANIX$
-50	1.135	1.299	1.0198
-45	1.186	1.275	1.016
-41	1.170	1.299	1.0161
-36	1.209	1.299	1.0124
-31	1.187	1.396	1.0147
-25	1.288	1.398	1.0139
-21	1.579	1.96	1.0337
-20	1.819	1.919	1.0195
23	1.38	1.464	1.0116
30	1.289	1.49	1.0087
33	1.300	1.337	1.0114
37	1.257	1.178	1.0046
40	1.268	1.619	1.017
45	1.270	1.286	1.0102
51	1.438	1.296	1.0152
58	1.360	1.316	1.0124
65	1.326	1.176	1.0223

Table S2. ANIX calculated for F_{760} , F_{687} and $sPRI$ measured in the CPP over chickpea.

SZA (°)	F_{760_ANIX}	F_{687_ANIX}	$sPRI_ANIX$
-60	1.547	2.812	1.0106
-57	1.638	2.104	1.0137
-55	1.711	3.432	1.0141
-52	1.907	3.34	1.0146
-50	1.775	2.408	1.0139
-47	1.671	1.807	1.0167
-44	1.892	3.526	1.0108
-42	1.762	2.068	1.0141
-40	1.876	2.178	1.0105
-39	1.984	3.352	1.0102
41	1.880	2.565	1.0085
43	1.932	2.696	1.01
47	2.096	2.609	1.0101
53	1.867	1.895	1.0142
56	2.446	2.077	1.0163
60	1.652	2.907	1.013

Table S3. ANIX calculated for F_{760} , F_{687} and sPRI measured in the SPP over grass.

SZA (°)	<i>F</i> ₇₆₀ _ANIX	<i>F</i> ₆₈₇ _ANIX	<i>sPRI</i> _ANIX
-58	1.368	2.035	1.0112
-56	1.554	2.343	1.0141
-54	1.387	1.525	1.0075
-51	1.443	2.149	1.0099
-48	1.515	1.435	1.0101
-46	1.344	1.325	1.0094
-43	1.329	2.845	1.0118
-41	1.370	2.247	1.0116
-40	1.371	2.83	1.0103
-39	1.383	1.57	1.0055
41	1.337	2.227	1.0071
54	1.528	1.982	1.0078

Table S4. ANIX calculated for *F*₇₆₀, *F*₆₈₇ and *sPRI* measured in the CPP over grass.

SZA (°)	<i>F</i> ₇₆₀ _ANIX	<i>F</i> ₆₈₇ _ANIX	<i>sPRI</i> _ANIX
-53	2.615	3.165	1.0177
-48	3.197	4.532	1.0225
-43	3.547	8.86	1.0246
-32	3.144	4.205	1.0172
-26	2.690	4.189	1.015
-23	2.356	3.479	1.0174
-21	3.031	34.639	1.0246
26	3.335	8.767	1.0232
31	3.207	2.86	1.0198
37	5.068	3.829	1.0136
44	2.656	13.745	1.0172
46	2.725	4.334	1.0188
67	2.429	2.179	1.0181

Table S5. ANIX calculated for *F*₇₆₀, *F*₆₈₇ and *sPRI* measured in the SPP over rice.

SZA ($^{\circ}$)	F_{760_ANIX}	F_{687_ANIX}	$sPRI_ANIX$
-51	2.692	2.915	1.0168
-46	2.508	4.124	1.0147
-31	2.684	3.446	1.0098
-28	1.721	6.423	1.0107
-22	1.345	4.299	1.0106
27	3.682	65.169	1.0182
32	2.397	5.435	1.0147
39	3.528	2.265	1.0123
68	1.814	1.984	1.0152

Table S6. ANIX calculated for F_{760} , F_{687} and sPRI measured in the AR over rice.

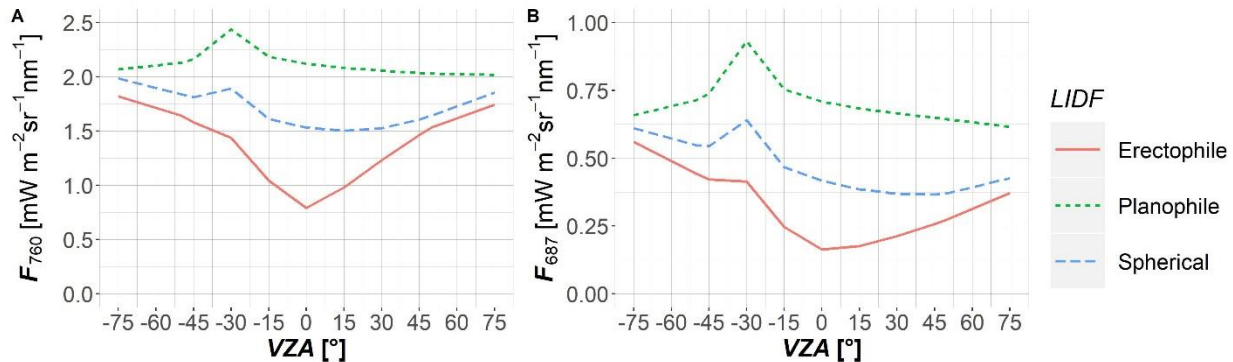


Figure S2. Distribution of multi-angular F_{760} (A) and F_{687} (B) in the solar principal plane (SPP) as a function of view zenith angle (VZA) and LIDF (erectophile, planophile and spherical) simulated with the SCOPE model. LAI = 3 $\text{m}^2 \text{m}^{-2}$, SZA = 0°, C_{ab} = 40 $\mu\text{g cm}^{-2}$, hc = 0.5 m, lw = 0.05 m. Negative values of VZAs represent the backscatter direction, positive – the forward scatter direction within a plane.

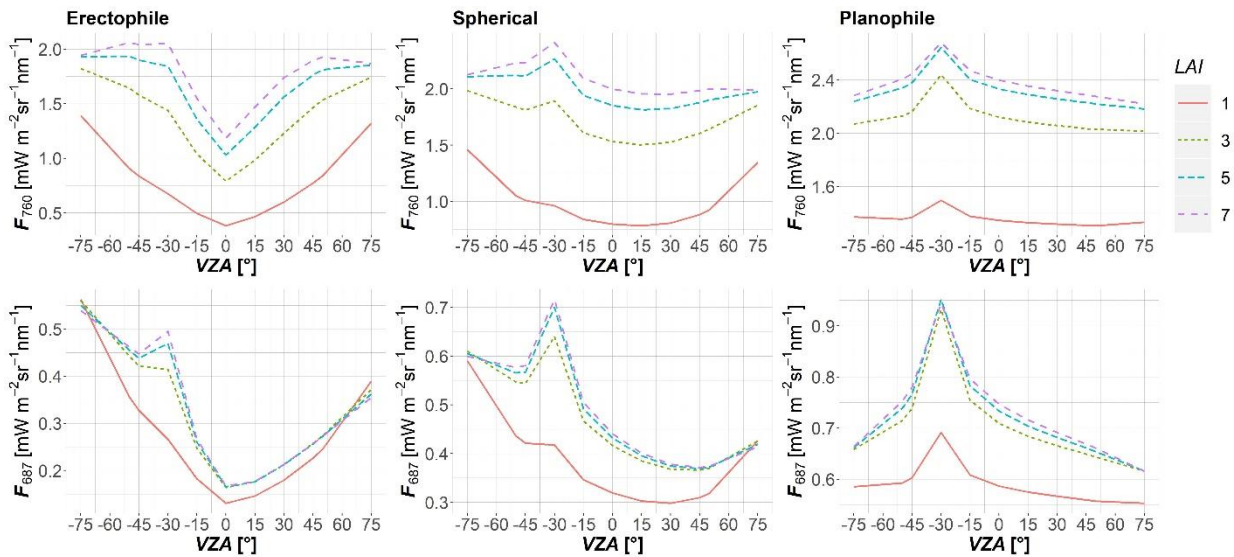


Figure S3. Distribution of multi-angular F_{760} (top) and F_{687} (bottom) in the solar principal plane (SPP) as a function of view zenith angle (VZA) and LAI simulated with the SCOPE model for erectophile (left), spherical (middle) and planophile (right) canopy types. $SZA = 30^\circ$, $C_{ab} = 40 \text{ ug cm}^{-2}$, $hc = 0.5 \text{ m}$, $lw = 0.05 \text{ m}$. Negative values of VZAs represent the backscatter direction, positive – the forward scatter direction within a plane.

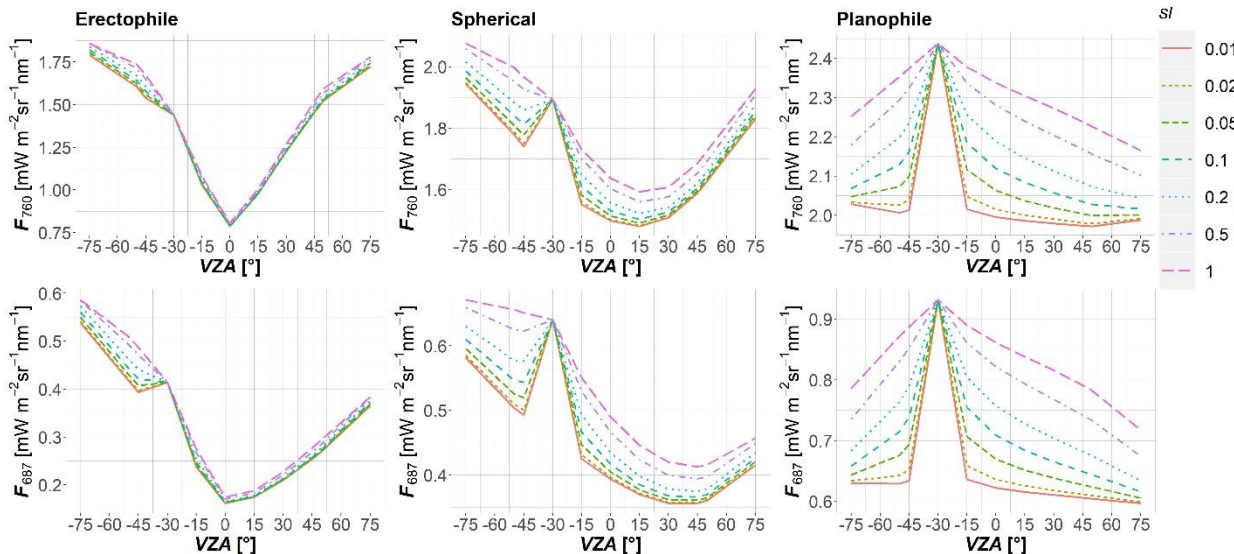


Figure S4. Distribution of multi-angular F_{760} (top) and F_{687} (bottom) in the solar principal plane (SPP) as a function of view zenith angle (VZA) and sl simulated with the SCOPE model for erectophile (left), spherical (middle) and planophile (right) canopy types. $LAI = 3 \text{ m}^2 \text{ m}^{-2}$, $SZA = 30^\circ$, $C_{ab} = 40 \text{ ug cm}^{-2}$. Negative values of VZAs represent the backscatter direction, positive - the forward scatter direction within a plane.

<i>LIDF</i>	C_{ab} ($\mu\text{g cm}^{-2}$)	<i>LAI</i> ($\text{m}^2 \text{m}^{-2}$)	<i>hc</i> (m)	<i>lw</i> (m)	SZA ($^\circ$)	F_{760_ANIX}	F_{687_ANIX}
erectophile	40	1	0.5	0.05	30	3.677	4.3761
erectophile	40	3	0.5	0.05	30	2.336	3.5383
erectophile	40	5	0.5	0.05	30	1.926	3.4654
erectophile	40	7	0.5	0.05	30	1.783	3.3834
spherical	40	1	0.5	0.05	30	1.893	2.0301
spherical	40	3	0.5	0.05	30	1.359	1.7913
spherical	40	5	0.5	0.05	30	1.271	1.9671
spherical	40	7	0.5	0.05	30	1.26	2.0237
planophile	40	1	0.5	0.05	30	1.16	1.2665
planophile	40	3	0.5	0.05	30	1.232	1.5551
planophile	40	5	0.5	0.05	30	1.233	1.6129
planophile	40	7	0.5	0.05	30	1.235	1.6241

Table S7. ANIX calculated for F_{760} , F_{687} simulated by SCOPE with the input parameters: SZA = 30° , C_{ab} = $40 \mu\text{g cm}^{-2}$, hc = 0.5 m, lw = 0.05 m, LAI = 1, 3, 5, 7 $\text{m}^2 \text{m}^{-2}$ and *LIDF* corresponding to erectophile, spherical and planophile canopy types.

<i>LIDF</i>	C_{ab} ($\mu\text{g cm}^{-2}$)	<i>LAI</i> ($\text{m}^2 \text{ m}^{-2}$)	<i>sl</i>	<i>hc</i> (m)	<i>lw</i> (m)	<i>SZA</i> (°)	<i>F_{760_ANIX}</i>	<i>F_{687_ANIX}</i>
erectophile	40	3	0.1	0.1	0.01	30	2.352	3.578
erectophile	40	3	0.02	0.5	0.01	30	2.336	3.538
erectophile	40	3	0.01	1	0.01	30	2.314	3.466
erectophile	40	3	0.5	0.1	0.05	30	2.352	3.578
erectophile	40	3	0.1	0.5	0.05	30	2.336	3.538
erectophile	40	3	0.05	1	0.05	30	2.314	3.466
erectophile	40	3	1	0.1	0.1	30	2.352	3.578
erectophile	40	3	0.2	0.5	0.1	30	2.336	3.538
erectophile	40	3	0.1	1	0.1	30	2.314	3.466
planophile	40	3	0.1	0.1	0.01	30	1.209	1.512
planophile	40	3	0.02	0.5	0.01	30	1.232	1.555
planophile	40	3	0.01	1	0.01	30	1.236	1.561
planophile	40	3	0.5	0.1	0.05	30	1.209	1.512
planophile	40	3	0.1	0.5	0.05	30	1.232	1.555
planophile	40	3	0.05	1	0.05	30	1.236	1.561
planophile	40	3	1	0.1	0.1	30	1.209	1.512
planophile	40	3	0.2	0.5	0.1	30	1.232	1.555
planophile	40	3	0.1	1	0.1	30	1.236	1.561
spherical	40	3	0.1	0.1	0.01	30	1.381	1.834
spherical	40	3	0.02	0.5	0.01	30	1.359	1.791
spherical	40	3	0.01	1	0.01	30	1.341	1.797
spherical	40	3	0.5	0.1	0.05	30	1.381	1.834
spherical	40	3	0.1	0.5	0.05	30	1.359	1.791
spherical	40	3	0.05	1	0.05	30	1.341	1.797
spherical	40	3	1	0.1	0.1	30	1.381	1.834
spherical	40	3	0.2	0.5	0.1	30	1.359	1.791
spherical	40	3	0.1	1	0.1	30	1.341	1.797

Table S8. ANIX calculated for F_{760} , F_{687} simulated by SCOPE with the input parameters: $SZA = 30^\circ$, $C_{ab} = 40 \text{ ug cm}^{-2}$, $LAI = 3 \text{ m}^2 \text{ m}^{-2}$, $hc = 0.1, 0.5, 1 \text{ m}$, $lw = 0.01, 0.05, 0.1 \text{ m}$, $sl = 0.01, 0.02, 0.05, 0.1, 0.2, 0.5, 1$ and LIDF corresponding to erectophile, spherical and planophile canopy types.

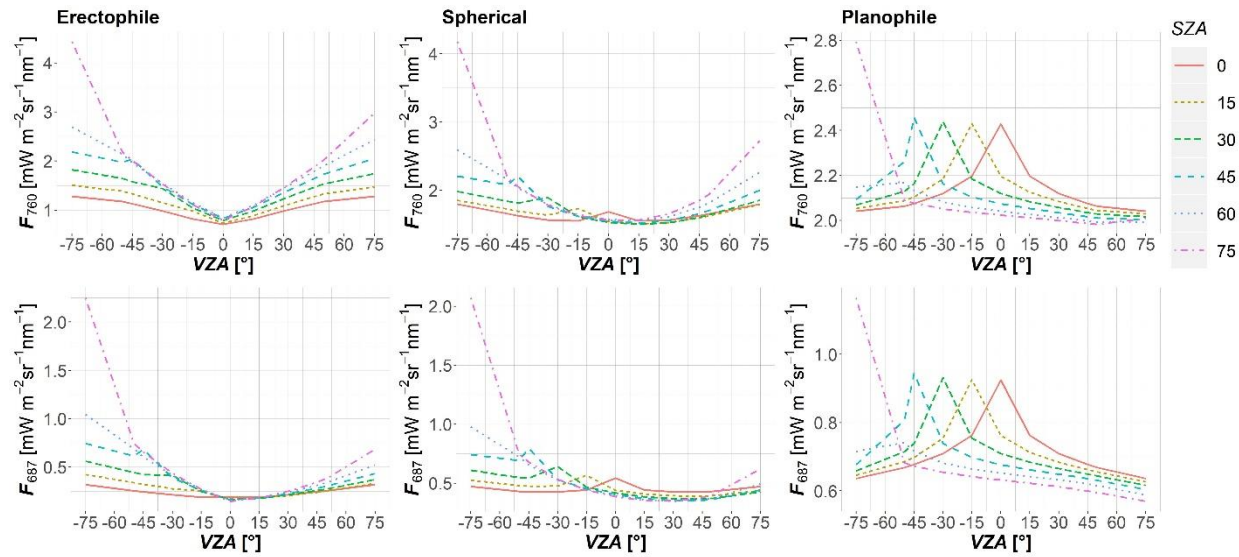


Figure S5. Distribution of multi-angular F_{760} (top) and F_{687} (bottom) in the solar principal plane (SPP) as a function of view zenith angle (VZA) and SZA simulated with the SCOPE model for erectophile (left), spherical (middle) and planophile (right) canopy types. $LAI = 3 \text{ m}^2 \text{ m}^{-2}$, $C_{ab} = 40 \text{ ug cm}^{-2}$, $hc = 0.5 \text{ m}$, $lw = 0.05 \text{ m}$. Negative values of VZAs represent the backscatter direction, positive – the forward scatter direction within a plane.

<i>LIDF</i>	C_{ab} (ug cm ²)	<i>LAI</i> (m ² m ⁻²)	<i>sl</i>	<i>hc</i> (m)	<i>lw</i> (m)	SZA (°)	F_{760_ANIX}	F_{687_ANIX}
erectophile	40	3	0.1	0.5	0.05	75	5.621	15.664
erectophile	40	3	0.1	0.5	0.05	60	3.335	7.268
erectophile	40	3	0.1	0.5	0.05	45	2.692	4.884
erectophile	40	3	0.1	0.5	0.05	30	2.336	3.538
erectophile	40	3	0.1	0.5	0.05	15	2.075	2.564
erectophile	40	3	0.1	0.5	0.05	0	1.807	1.709
planophile	40	3	0.1	0.5	0.05	75	1.425	2.083
planophile	40	3	0.1	0.5	0.05	60	1.143	1.379
planophile	40	3	0.1	0.5	0.05	45	1.248	1.606
planophile	40	3	0.1	0.5	0.05	30	1.232	1.555
planophile	40	3	0.1	0.5	0.05	15	1.222	1.523
planophile	40	3	0.1	0.5	0.05	0	1.216	1.501
spherical	40	3	0.1	0.5	0.05	75	2.707	6.087
spherical	40	3	0.1	0.5	0.05	60	1.744	3.092
spherical	40	3	0.1	0.5	0.05	45	1.499	2.32
spherical	40	3	0.1	0.5	0.05	30	1.359	1.791
spherical	40	3	0.1	0.5	0.05	15	1.266	1.494
spherical	40	3	0.1	0.5	0.05	0	1.205	1.339

Table S9. ANIX calculated for F_{760} , F_{687} simulated by SCOPE with the input parameters: SZA = 10°, 30°, 45°, 60°, 75°, C_{ab} = 40 ug cm⁻², LAI = 3 m² m⁻², hc = 0.5m, lw = 0.05 m and LIDF corresponding to erectophile, spherical and planophile canopy types.

3. Part 2. Extracting the vegetation physiological response from time series of solar-induced chlorophyll fluorescence and PRI using Singular Spectrum Analysis

Abstract

²Continuous ground-based spectral measurements of solar-induced chlorophyll fluorescence (F) and the Photochemical Reflectance Index (PRI) encode temporal dynamics of photosynthetic light-use efficiency (LUE) and vegetation responses to stress factors. However, these signals are modulated by the processes acting at different timescales. These processes include evolution of pigment pools at weekly to seasonal timescales, modulation of light use efficiency due to activation of xanthophyll cycle and downregulation of photosynthesis at shorter timescale, and directional effects induced by diurnally varying solar-view geometry. Disentangling of different sources of variability in time series to unambiguously link optical signal to vegetation functioning is still a challenging task.

Here we explore whether Singular Spectrum Analysis (SSA), a highly adaptive method of spectral time series decomposition, is capable to extract ecologically interpretable components from far-red F (F_{760}) and PRI time series of modelled data.

The proof of concept relies on half-hourly time series of synthetic data simulated with the Soil Canopy Observation, Photochemistry and Energy fluxes (SCOPE) radiative transfer model, which was parameterized using vegetation traits derived from field observations as well as one year of meteorological data from Mediterranean grassland. SCOPE models leaf-level F and PRI based on leaf physiology and modifies these signals via radiative transfer to the top of the canopy. We ran SCOPE with and without the explicit simulation of de-epoxidation of the xanthophyll cycle pigments as part of the non-photochemical quenching (NPQ). This allowed to compute PRI_0^{scope} , which represents the constitutive variability when NPQ is not activated (pigment pool modifications), and the total PRI ($PRI_{\text{xan}}^{\text{scope}}$) which includes both constitutive and facultative variability (pigments and NPQ processes). The difference between the two ($\Delta PRI^{\text{scope}}$) represents the variability of PRI at short timescale related to physiological modulation of photosynthesis at canopy scale. Similarly, F was simulated with and without the fluorescence amplification factor (ϕ_f') - F_{760}^{scope} and $F_{0,760}^{\text{scope}}$, respectively. Baseline fluorescence $F_{0,760}^{\text{scope}}$ corresponds to the emission under low light conditions, only affected by canopy biophysical properties and illumination conditions, and the difference between F_{760}^{scope} and $F_{0,760}^{\text{scope}}$ is a reference of fluorescence physiological emission ($\Delta F_{760}^{\text{scope}}$).

² The content of this part related to model-based study has been submitted to Journal of Geophysical Research: Biogeosciences as Biriukova, K., Pacheco-Labrador, J., Migliavacca, M., Mahecha, M., Gonzalez-Cascon, R., Martín, M.P., Rossini, M. (2020). Extracting the Vegetation Physiological Response From Time Series of Solar-Induced Chlorophyll Fluorescence and PRI Using Singular Spectrum Analysis: a Model-Based Study.

We applied SSA to deconvolve slow and fast variability in $PRI_{\text{xan}}^{\text{scope}}$, F_{760}^{scope} and far-red fluorescence apparent yield ($Fy_{760}^{*\text{scope}}$). The resulting slow SSA components of $PRI_{\text{xan}}^{\text{scope}}$ and $Fy_{760}^{*\text{scope}}$ showed high correlations with the reference constitutive variables ($R^2=0.97$; 0.96). Fast SSA components were compared to physiological variables – NPQ and light-use efficiency (LUE), computed as a ratio of gross primary production (GPP) to photosynthetically active radiation absorbed by chlorophyll ($aPAR_{\text{Cab}}$). The best results were archived for fast modes of $PRI_{\text{xan}}^{\text{ssa}}$, which exhibited linear relationship with LUE with distance correlation ($dCor$) varying in the range 0.7 - 0.95 for the most part of the year. Fast component of F_{760}^{ssa} was negatively correlated with LUE with $dCor$ 0.50 - 0.90 for leaf area index (LAI) higher than $1 \text{ m}^2\text{m}^{-2}$. The direction of relationship between LUE and fast varying component of $Fy_{760}^{*\text{ssa}}$, instead, was affected by NPQ . Under $NPQ < 0.1$ the correlation was negative ($R=-0.55$), while for NPQ varying between 0.1 and 2.5 the correlation was positive ($R=0.69$). The application of this methodology on a field dataset of spectral and flux time series collected in winter wheat field allowed to improve the correlation of fast components of F_{760} and PRI with fast component of LUE ($dCor=0.57$ and 0.66, respectively) in comparison with original time series.

We expect time series decomposition methods such as SSA to improve the information extracted from time series of high-resolution ground spectral measurements. Coupled with simultaneous carbon flux observations, these decomposed optical signals can provide better proxies of vegetation functioning.

3.1. Introduction

Remote and proximal sensing of vegetation pursuit accurate monitoring of plant physiology and photosynthesis. During the last two decades, the interest of the remote sensing community towards solar-induced chlorophyll fluorescence (F) and Photochemical Reflectance Index (PRI) (Gamon et al., 1992) has increased due to evidences of close relationship between plant physiological properties and these optical signals (Garbulsky et al., 2011; Meroni et al., 2009; Mohammed et al., 2019). The ability of plants to deal with environmental stress factors is maintained by a combination of different processes. Under optimal light conditions and adequate water and nutrients supply, photochemical reactions, including CO_2 assimilation and electron transport, occur at high efficiency. To avoid the damage of the reaction centres, excessive solar energy is emitted as F in the 650-850 nm spectral range or dissipated as heat as part of non-photochemical quenching (NPQ) (Demmig-Adams & Adams, 1992). Since all three mechanisms (carbon-fixation, F and NPQ) compete for the same absorbed energy, characterisation of both F and NPQ is required for an accurate inference of photosynthesis from optical signals (Frankenberg & Berry, 2018; Porcar-Castell et al., 2014). One of the mechanisms of NPQ thermal dissipation is de-epoxidation of xanthophyll cycle pigments (Demmig-Adams, 1990; Niyogi et al., 1997). The excess energy leads to interconversion of xanthophyll cycle pigments, violaxanthin to antheraxanthin and then to zeaxanthin, providing a sink for the excess energy (Vilfan et al., 2018). This process is quickly reversible and zeaxanthin is converted back to violaxanthin under low light conditions and during the night. Xanthophyll cycle pigments conversion results in an increase in light absorptance at 531 nm, which is detectable by PRI (Gamon et al., 1992; Garbulsky et al., 2011).

Based on the conceptual light-use efficiency framework introduced in Monteith (1972), gross primary production (*GPP*) is a product of photosynthetically active radiation absorbed by chlorophyll ($aPAR_{Cab}$) and efficiency with which this absorbed light is converted to fixed carbon (light-use efficiency, *LUE*):

$$GPP = aPAR_{Cab} \cdot LUE \quad (8)$$

Numerous studies have shown that canopy and ecosystem level *F* and *PRI* measured from a variety of tower-based (e.g. Hilker et al., 2010a; Perez-Priego et al., 2015; Zhang et al., 2015), airborne (e.g. Middleton et al., 2017; Rascher et al., 2015; Rossini et al., 2015; Tagliabue et al., 2019) and spaceborne platforms (e.g. Middleton et al., 2016; Sun et al., 2018) can successfully track variations in *GPP* and/or *LUE*. However, canopy scale *F* and *PRI* are not exclusively driven by plant physiology. A combination of processes acting at different timescales can affect the resulting *F* and *PRI* signal. Slow variability includes seasonal variations related to phenology, which are manifested in changing pigment pools and canopy structure (e.g. leaf area index, *LAI*). Fast variability includes both diurnal cycles driven by directionally varying incoming radiation, and sub-diurnal physiological responses induced by variations in meteorological and stress conditions (e.g. high vapour pressure deficit, *VPD*).

At seasonal scale, *PRI* was shown to be sensitive to leaf properties, especially to pigment pool modifications due to slow varying environmental factors, such as increasing or decreasing sun exposure, aging process, chronic stress (Filella et al., 2009). Those irreversible changes are termed constitutive properties of *PRI* (Gamon and Berry, 2012). Fast changes in *PRI*, in turn, are termed facultative, and include rapid reversible changes of the de-epoxidation state (DEPS) of xanthophylls as physiological response to illumination changes (Demmig-Adams & Adams, 1992).

Following the adaption of the *LUE* model (e.g. Lee et al., 2013) top of the canopy (TOC) *F* signal can be defined as:

$$F = aPAR_{Cab} \cdot \phi_f \cdot f_{esc} \quad (9)$$

where $aPAR_{Cab}$ is a function of the photosynthetically active radiation (*PAR*) and fraction of *PAR* absorbed by chlorophyll pigments ($f_{aPAR_{Cab}}$), ϕ_f is physiological *F* emission yield, f_{esc} is the fraction of all *F* photons that escape from the canopy. Both $f_{aPAR_{Cab}}$ and f_{esc} are determined by canopy structure and leaf biochemical properties (Migliavacca et al., 2017; Martini et al., 2019), which usually vary at slow (seasonal) timescale. Fluorescence yield ϕ_f , in turn, directly responds to the energy partitioning in the photosynthetic machinery, and its variability mostly occurs at fast timescales – diurnal and sub-diurnal – driven by the modulation of the physiological status of plants.

Despite major efforts of remote sensing community aiming at predicting vegetation functioning, the separation of physiological and the remaining sources of variability from these signals is still a challenge which hampers full exploitation of long-term data series collected by unattended spectroradiometric systems as those described in Porcar-Castell et al. (2015).

The Singular Spectrum Analysis (SSA) is a comprehensive methodology originally established by Broomhead and King (1986) and Fraedrich (1986) and later developed by Golyandina et al. (2001) and Ghil et al. (2002). SSA was proved to be a powerful tool for time series decomposition, reconstruction and forecasting of climatic time series (Ghil et al., 2002; Plaut et al., 1995; Yiou et al., 1996), as well as for characterizing dynamics of eddy covariance ecosystem-atmosphere fluxes (Mahecha et al., 2007; Mahecha et al., 2010a; Wang et al., 2012) and for the evaluation of terrestrial biosphere and semi- empirical model output performances at different timescales (Mahecha et al., 2010b; Migliavacca et al., 2015).

The main idea behind SSA is that time series can be described as a sum of superimposed subsignals, which can be extracted based on the characteristic scales of variability (Mahecha et al., 2010a). The main difference between one-dimensional SSA and other methods for time series analysis is that SSA is a non-parametric method, which does not require prior information about the number and/or frequencies of periodicities or a model for trend (Golyandina et al., 2018).

We extend the use of SSA to time series of optical signals related to physiology. To prove the suitability of SSA to decompose time series of *PRI*, far-red fluorescence (F_{760}) and far-red fluorescence apparent yield (F_{760}/PAR , Fy^*_{760}) into slow and fast varying components attributed to different sources of variability (i.e. structural vs physiological changes) we used a realistic synthetic dataset generated with the Soil Canopy Observation of Photochemistry and Energy fluxes (SCOPE) model (van der Tol et al., 2009). SCOPE was parameterized to reproduce the spectral behaviour of a Mediterranean grassland. The structural traits derived from field measurements, as well as meteorological data from the research station of Majadas de Tiétar (Cáceres, Spain), were used. A complete description of the study site can be found in Perez-Priego et al. (2017) or El-Madany et al. (2018). SCOPE simulates leaf-level physiology and the corresponding *PRI* and *F* signals, which are propagated to the TOC via radiative transfer. In order to evaluate whether extracted SSA components are related either to constitutive or facultative variability, SCOPE model was run in two different modes featuring and excluding physiological effects on *PRI* and *F* (i.e. the effect of xanthophyll cycles de-epoxidation on leaf absorption and fluorescence efficiency amplification factor (ϕ'_f) on *F*).

In this study, we aim to test the potential of SSA to decouple fast variability, attributed to physiological status, and slow variability, attributed to seasonally changing structural and biochemical vegetation properties, using half-hourly SCOPE-simulated and measured time series of *PRI*, F_{760} and Fy^*_{760} . We also evaluate the potential to predict *NPQ* and *LUE* with the fast components of the SSA-decomposed optical signals.

3.2. Theoretical background: Singular Spectrum Analysis

SSA is one of several potential time series decomposition techniques. It was chosen here because it is highly data-adaptive and allows for decomposing highly phase-modulated signals. The method can be described in four steps: embedding, decomposition, grouping and reconstruction (Nina Golyandina & Korobeynikov, 2014).

Step 1: Embedding. The original time series $Y = (f_1, \dots, f_N)$ of length N is transformed into a time-delay-embedding covariance matrix composed of a sequence of $K=N-L+1$ lagged vectors of length L (window length):

$$X_i = (x_i, \dots, x_{i+L-1})^T, i = 1, \dots, K. \quad (10)$$

Step 2: Decomposition. Singular value decomposition (SVD) leads to elementary matrices of rank 1:

$$X = X_1 + \dots + X_d \quad (11)$$

where d is a rank of X . Each elementary matrix X_i is defined by the eigentriple:

$$X_i = \sqrt{\lambda_i} U_i V_i^T \quad (12)$$

The eigentriple consists of a singular value $\sqrt{\lambda_i}$, the left eigenvector U_i and the right eigenvector V_i . The singular values of eigentriples are proportional to the fraction of explained variance corresponding to each eigentriple.

Step 3: Grouping. The grouping is performed by choosing the sets of eigentriples (eigentriple grouping) so that each set corresponds to an identifiable series component. The grouping procedure partitions the set of indices $\{1, \dots, d\}$ into m disjoint subsets I_1, \dots, I_m . The result of this step is the grouped matrix decomposition of the expansion (12):

$$X = X_{I_1} + \dots + X_{I_m} \quad (13)$$

Step 4: Reconstruction. In the last step each matrix of the grouped decomposition (7) is transformed into a new series of length N by diagonal averaging. As a result, the initial time series (f_1, \dots, f_N) is decomposed into a sum of m reconstructed series:

$$f_n = \sum_{k=1}^m \tilde{f}_n^{(k)}, n = 1, \dots, N. \quad (14)$$

Time series decomposition was implemented using R-packages *Rssa* (Golyandina et al., 2018; Korobeynikov et al., 2017) and *spectral.methods* (Buttlar et al., 2014). There are two parameters in SSA, which must be set by the analyst: the window length (L) and grouping of the eigentriples. The choice of L is dependent on the characteristics of the subsignal to be extracted. In general, $L \leq N/2$, and the higher the L , the more detailed the decomposition is. For the identification of trend, L should be large enough to be separable from periodic oscillations and noise. For the extraction of a periodic component with a period T , it is advisable to take L proportional to T . The periods of the harmonic components of the time series can be identified with the periodogram.

The grouping can be done either manually by analysing the graphs of eigenvectors and their frequencies, or automatically (Golyandina and Zhigljavsky, 2013). In this study we used the

automatic grouping implemented in *spectral.methods* R-package (Buttlar, 2015), which allows to group SSA components based on their common features. This method measures the commonality of components by means of the weighted correlations between the components: if weighted correlation is high, then the corresponding components have similar behaviours and should be included in one group (Golyandina et al., 2018).

3.3. Proof of the concept: a model-based study

3.3.1. Methods

3.3.1.1. SCOPE simulations

SCOPE version 1.73 was used to simulate one year time series of TOC reflectance factor (R), F , and fluxes with half-hourly time step (dataset can be found in Biriukova et al. (2020b)). Variations of leaf absorptance between 500 and 570 nm induced by violaxanthin into zeaxanthin and reverse conversions of the xanthophyll cycle were simulated by the leaf radiative transfer model (RTM) Fluspect (Fluspect-CX) (Vilfan et al., 2018). Fluorescence radiance was simulated by SCOPE using the fluorescence emission spectra characterised from FluoWat leaf clip measurements (fluorescence of photosystems I and II are not separated, SCOPE parameter “calc_PSI”=0) (Vilfan et al., 2016) and an empirical fluorescence model (van Der Tol et al., 2014) (SCOPE parameter “Fluorescence_model”=0).

The distribution of absorbed light into competitive pathways is controlled by the rate coefficients (K) which express the probability of the different fates of the excitations (C. van Der Tol et al., 2014). Rate constant for constitutive thermal dissipation that is present in dark adapted plants (K_d) was defined by leaf temperature (T) as $K_d = \max(0.8738, 0.0301 \cdot (T - 273.15) + 0.0773)$, rate constant for fluorescence (K_f) was set to 0.05, and rate constant for heat dissipation as part of NPQ (K_n) was defined as $K_n = K_{no} \cdot (1 + \text{beta}) \cdot x^{\alpha\text{pha}} / (\text{beta} + x^{\alpha\text{pha}})$, where K_{no} , alpha, beta are fitting parameters of the empirical model (equal to 5.01, 1.93, 10, respectively). Rate constant of photochemistry (K_p) was set to 4. Degree of light saturation (x , used for computation of K_n), steady-state fluorescence yield (F_s), and fluorescence efficiency amplification factor (ϕ'_f) are the output parameters of fluorescence module of SCOPE model. NPQ was computed as $K_n / (K_f + K_D)$. Steady-state fluorescence yield was computed as $F_s = F_m * (1 - \phi_p)$, where light-adapted fluorescence yield $F_m = K_f / (K_f + K_d + K_n)$, and photochemical yield $\phi_p = \phi_p^0 \cdot J_a / J_e$, where ϕ_p^0 is photochemical yield under dark adapted conditions, J_a is actual electron transport rate, J_e is potential electron transport rate (van Der Tol et al., 2014).

The simulations included temperature correction of the maximum carboxylation rate ($V_{c\text{max}}$, [$\mu\text{mol m}^{-2} \text{s}^{-1}$]) (SCOPE parameter “apply_T_corr”=1). Soil heat flux was defined as a constant fraction of soil net radiation (SCOPE parameter “soil_heat_method”=2).

SCOPE was parameterized using structural vegetation parameters as well as meteorological data from the research station of Majadas de Tiétar (39°56'24.68"N, 5°45'50.27"W) (Cáceres, Spain). The

station is located in a typical Mediterranean savanna ecosystem dominated by herbaceous stratum constituted by grasses, forbs, and legumes. The site is characterized by mean annual temperature of 16 °C with wet season from November to May and dry summer (Perez-Priego et al., 2015).

In order to realistically represent seasonal and intra-daily meteorological conditions we used half-hourly observations of forcing meteorological variables measured in 2016 (Perez-Priego et al., 2017). Down-welling short wave (R_{in} , [W m^{-2}]) and long wave (R_{li} , [W m^{-2}]) radiation, air temperature (T_{air} , [°C]), atmospheric vapour pressure (e_a , [hPa]), air pressure (p , [hPa]), relative humidity (RH , [%]) and wind speed (u , [m s^{-1}]) were recorded at 1.6 m height. VPD , ([hPa]) was computed from T_{air} , e_a , and RH . Sun zenith (SZA, [°]) and azimuth (SAA, [°]) angles were computed from site coordinates and timestamps using the algorithm of Reda and Andreas, 2004.

Soil moisture content (SM_p , [%]) averaged from 4 sensors at 5 cm depth was used to modulate soil R in the brightness-shape-moisture (BSM) sub-model of SCOPE (Verhoef et al., 2018). The parameterization of SCOPE was defined according to Pacheco-Labrador et al. (2019) in the same site. Soil resistance for evaporation from the pore space (r_{ss} , [s m^{-1}]) was estimated from SM_p as in Pacheco-Labrador et al. (2019).

Seasonal variability of leaf area index (LAI , [$\text{m}^2 \text{ m}^{-2}$]) and leaf chlorophyll (C_{ab} , [$\mu\text{g cm}^{-2}$]) and carotenoids contents (C_{ca} , [$\mu\text{g cm}^{-2}$]) was simulated from time series of midday Normalized Difference Vegetation Index ($NDVI$) (Tucker, 1979) measured during 2016 by Decagon SRS sensor (Decagon Devices, Pullman, WA, USA) on Majadas de Tiétar grassland (Luo et al., 2018). Therefore, these parameters varied daily. LAI was derived from empirical relationship with $NDVI$ (Martín et al., 2020). C_{ab} was predicted using a model fit from field spectral measurements and pigments content determined from destructive samples of 25 x 25 cm grass patches sampled in several campaigns between 2017 and 2019 (Martín et al., 2020; Melendo-Vega et al., 2018). C_{ab} was estimated as $C_{ab} = (0.007 - (0.0001 / NDVI) \cdot \log(1 + (NDVI / 0.0001))) \cdot 4443.0$ while C_{ca} was predicted as a function of C_{ab} , according to the linear model $C_{ca} = 0.24 \cdot C_{ab} + 0.67$ using field information from the same dataset. The ratio C_{ab} to C_{ca} of the simulated dataset ranged between 3.06 in autumn to 3.78 in spring. Other parameters were kept constant during the simulation. Leaf angle distribution was assumed spherical. V_{cmax} was set to 80 $\mu\text{mol m}^{-2} \text{ s}^{-1}$ and the slope (m , [-]) of the Ball-Berry model (Collatz et al., 1991) was set to 10. These parameters were kept constant to simplify the simulations, so that the variability of F and PRI was triggered only by switching on/off the effect of changes in the DEPS of xanthophyll cycle pigments on PRI and the ϕ'_f on F specifically.

During the simulation, a constant diffuse to global radiation ratio of 20 % was forced. Moreover, the variables from the biochemical model of SCOPE (e.g. NPQ , ϕ'_f , ϕ_p), which are not part of the default output of SCOPE, were also extracted. Similar to fluxes (e.g. GPP), these variables were computed as a weighted mean of all leaves inside the canopy considering leaf angle distribution and the relative depth of each leaf, which determine the amount of radiation that each leaf receives (C. van der Tol et al., 2009). However, unlike fluxes, biochemical variables were not scaled by LAI since they are leaf rather than canopy scale parameters.

PRI was computed as follows (Gamon et al., 1992):

$$PRI = \frac{R_{570} - R_{531}}{R_{570} + R_{531}} \quad (15)$$

where R_{531} is the reflectance factor of the xanthophyll-sensitive band at 531 nm and R_{570} is the reflectance factor of the reference band at 570 nm. With this formulation, PRI values can vary between -1 and 1 and are directly proportional to NPQ .

$PRI_{\text{xan}}^{\text{scope}}$ was simulated featuring the effect of changes in the DEPS of xanthophyll cycle pigments on leaf absorptance with Fluspect-CX module of SCOPE (Vilfan et al., 2018), whereas PRI_0^{scope} was computed from R where the effect of the conversion of violaxanthin into zeaxanthin in the xanthophyll cycle was not simulated (Fig. 12).

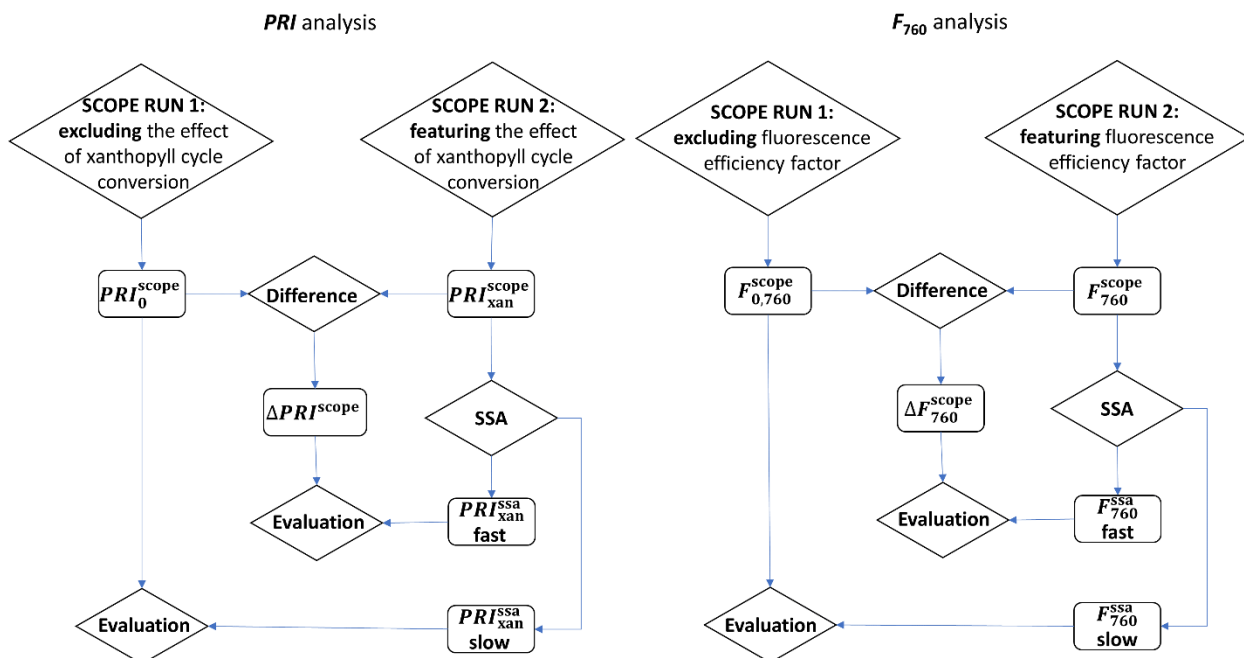


Figure 12. Schematic diagram of SCOPE simulations and SSA analysis.

Therefore, with $\Delta PRI^{\text{scope}}$, computed as the difference between $PRI_{\text{xan}}^{\text{scope}}$ and PRI_0^{scope} , we denote PRI variability induced only by physiological changes. Similarly, we simulated a baseline TOC fluorescence featuring (F_{760}^{scope}) and excluding ($F_{0,760}^{\text{scope}}$) ϕ'_f predicted by the photosynthesis-fluorescence model of SCOPE (van Der Tol et al., 2014) (Fig. 12). Baseline fluorescence corresponds to the emission under unstressed, low light conditions, only affected by canopy biophysical properties and illumination conditions, while the difference between F_{760}^{scope} and $F_{0,760}^{\text{scope}}$ ($\Delta F_{760}^{\text{scope}}$) is a reference for fluorescence physiological emission.

Fluorescence apparent yield variables ($Fy_{760}^{*\text{scope}}$, $Fy_{0,760}^{*\text{scope}}$) were computed as F normalized by photosynthetically active radiation (PAR). Since $aPAR_{\text{Cab}}$ is not easily obtainable from spectral measurements in many field set-ups, here we normalize F with PAR and not with $aPAR_{\text{Cab}}$ to test the applicability of the method on the metric usually available from field datasets. For validation of the SSA-decomposed physiology related component of $Fy_{760}^{*\text{scope}}$ we used a ratio $\Delta F_{760}^{\text{scope}}/\text{PAR}$. For the definition of the variables simulated with SCOPE and modelled with SSA refer to Table 5.

$PRI_{\text{xan}}^{\text{scope}}$	Total PRI featuring the effect of the xanthophyll cycle pigments conversion.
PRI_0^{scope}	Constitutive PRI excluding the effect of the xanthophyll cycle pigments conversion.
$\Delta PRI^{\text{scope}}$	Facultative PRI - the difference between $PRI_{\text{xan}}^{\text{scope}}$ and PRI_0^{scope} .
PRI_{ssa}	SSA decomposed components of total $PRI_{\text{xan}}^{\text{scope}}$.
F_{760}^{scope}	Far-red F featuring the fluorescence amplification factor (ϕ'_f).
$F_{0,760}^{\text{scope}}$	Far-red F yield excluding the fluorescence amplification factor (ϕ'_f).
$\Delta F_{760}^{\text{scope}}$	The difference between F_{760}^{scope} and $F_{0,760}^{\text{scope}}$.
F_{760}^{ssa}	SSA decomposed components of far-red F_{760}^{scope} .
$Fy^{*\text{scope}}_{760}$	Far-red F apparent yield featuring the fluorescence amplification factor (ϕ'_f)
$Fy^{*\text{scope}}_{0,760}$	Far-red F apparent yield excluding the fluorescence amplification factor (ϕ'_f).
$Fy^{*\text{ssa}}_{760}$	SSA decomposed components of far-red $Fy^{*\text{scope}}_{760}$.

Table 5. Definition of the variables simulated with SCOPE and modelled with SSA.

Only daytime data were simulated. Any situation where $R_{\text{in}} \leq 10 \text{ W m}^{-2}$ or $SZA \geq 85^\circ$ was considered night. Night-time values of different model outputs were linearly interpolated between the sunrise and sunset value. However, since R could strongly change due to small variations in SZA, sunrise and sunset were simulated differently in order to provide a smooth baseline. For these time steps we set $SZA = 85^\circ$ and used the forcing meteorological variables of the following or the previous time step, respectively. R was calculated for $R_{\text{in}} = 10 \text{ W m}^{-2}$ using the optical radiative transfer module of SCOPE only, so that no physiological effect was present and night-time baselines for both $PRI_{\text{xan}}^{\text{scope}}$ and PRI_0^{scope} were identical. The rest of model outputs were computed for $R_{\text{in}} = 0 \text{ W m}^{-2}$ using the full model. At these radiation levels, the effects of xanthophyll cycle on the R resulted negligible and was assumed that these could be representative of the simulation carried out with no light. Night-time interpolation is necessary since the subsequent time series analyses require continuous data. This gap filling is considered reasonable for parameters that are not expected to strongly vary during the night, such as F or R -based variables such as PRI . These assumptions might not completely hold due, for example, to physiological recovery. As PAR equals 0 at night, the night-time gaps in the series of $Fy^{*\text{scope}}_{760}$ were filled with the maximum daytime values selected in the moving window of 1 day. In order to simulate observational uncertainty, Gaussian noise was added to the time series of PRI , F_{760} and $Fy^{*\text{scope}}_{760}$ with mean (μ) equal 0 standard deviation (σ) equal 95% quantile of daytime data multiplied by 0.01.

LUE [$\mu\text{mol CO}_2 / \mu\text{mol photons absorbed}$] was computed as a ratio of simulated GPP to $aPAR_{\text{Cab}}$.

3.3.1.2. SSA decomposition

The SSA decomposition algorithm described in section 3.2 was run stepwise for each frequency interval (which are specified by “borders.wl” argument in Table 6). This allows adapting L for a particular frequency bin to be extracted. The choice of frequency bands is subjective and was determined here based on the time series length and temporal resolution (30 min). We divided time series into three intuitive frequency bins with an intention to test SSA component extracted in different bins and their relationships with reference signals (i.e. PRI_0^{scope} , $\Delta PRI^{\text{scope}}$, $F_{0,760}^{\text{scope}}$, $\Delta F_{760}^{\text{scope}}$). In particular, we defined the following classes: long-term or seasonal (2 weeks – 1 year), diurnal (7 hours – 2 weeks), sub-diurnal (30 min – 7 hours). For each frequency bin the corresponding window length was chosen: 2 months, 1 week and 1 day. The choice of window length was supported by the SSA theory (i.e. for the extraction of the long-term component the L was chosen large enough to be separable from periodic component, while for the extraction of diurnal oscillations, L was chosen proportional to the period of 1 day). The data associated with the output of SSA analysis can be found in Biriukova et al. (2020b).

SSA decomposition was applied on time series of $PRI_{\text{xan}}^{\text{scope}}$, PRI_0^{scope} , F_{760}^{scope} , $F_{0,760}^{\text{scope}}$, $Fy_{760}^{*\text{scope}}$, $Fy_{760}^{*\text{scope}}$. The parameters of the decomposition used in the function *filterTSeriesSSA* are reported in Table 6.

Argument	Description	Value
borders.wl	Borders of the different periodicity bands to extract. Units are the sampling frequency of the series (half-hourly observations).	1) 672, Inf (seasonal) 2) 14, 672 (diurnal) 3) 0, 14 (sub-diurnal)
M	Window length or embedding dimension. Units are the sampling frequency of the series (half-hourly observations).	Vector: (2880,336,48)
n.comp	Amount of SSA components to compute.	Vector: (20, 20, 20)
harmonics	How many harmonics to include in each component.	Vector: (0,0,0)
repeat. extr	How often to repeat the extraction.	Vector: (2,1,1)
center.series	Whether to center the series around zero prior to the computation.	TRUE
grouping	Method to use for grouping the individual SSA eigentriples.	grouping.auto
groupingMethod	Method for automatic grouping.	wcor
SSA. methods	Methods to use for the SSA computation.	"auto" - Automatic method selection depending on the series length, window length, SSA kind and number of eigenvalues requested.

Table 6. Parameters of *filterTSeriesSSA* (*spectral.methods* R-package (Buttlar, 2015)) function used for the decomposition of PRI_{xan}^{scope} , PRI_0^{scope} , F_{760}^{scope} , F_{760}^{*scope} , Fy_{760}^{*scope} , $Fy_{0,760}^{*scope}$.

3.3.1.3. Statistical analysis

To assess the relationship between decomposed and original variables we used distance correlation (*dCor*) (Székely et al., 2007). *dCor* varies between 0 and 1, and *dCor*=0 when variables are independent. The distance dependence measures are based on certain Euclidean distances between sample elements rather than sample moments as in Pearson's correlation. An advantage of distance correlation over Pearson's correlation is that it measures both linear and nonlinear association between two random variables or random vectors. *dCor* of two random variables is computed as a ratio of their distance covariance (*dCov*) to the product of their distance standard deviations (*dVar*).

3.3.2. Results

3.3.2.1. Seasonal cycles of simulated variables

Mediterranean climate is characterized by a strong seasonality mostly driven by radiation and precipitations (e.g. El-Madany et al., 2018) with a rainy period from late fall to early spring and a dry season in summer extended to early fall (Fig. 13C). Simulated biophysical parameters, fluxes and spectral variables are coherent with the typical phenology of the grassland at the site (Luo et al., 2020). According to the models based on *NDVI* observations, during green-up period from fall to winter, simulated *LAI* and *C_{ab}* increased from 0.5 up to 2.5 m² m⁻² and from 7.5 to 25 µg cm⁻², respectively (Fig. 13E). This variability is coherent with expected phenology and with the variability of *SM_p*. The peak of the growing season in Majadas de Tiétar occurs in spring (Luo et al., 2020), this is reproduced by simulated *GPP* and *F₇₆₀^{scope}*, which featured maximum values at the beginning of May (Fig. 13F, H). Early summer is characterised by a dry-down period, a transition to hot and dry season with a strongly inhibited photosynthesis associated with scarce precipitations and *T_{air}* reaching 40 °C and *VPD* of 75 hPa (Fig. 13A, B), which is also represented by the simulation.

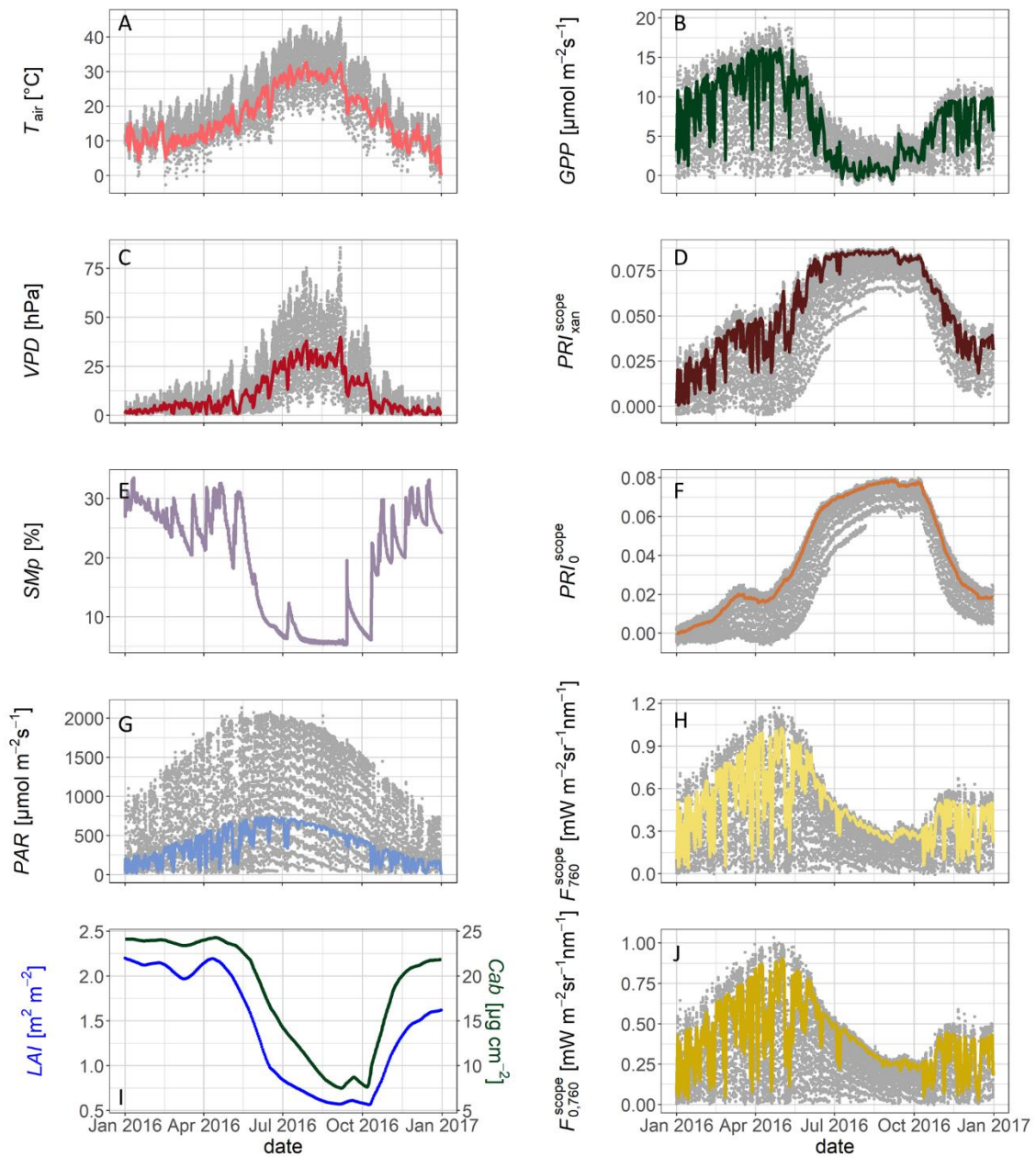


Figure 13. Time series of (A) air temperature (T_{air}), (C) vapor pressure deficit (VPD), (E) soil moisture content (SMP), (G) photosynthetically active radiation (PAR), (I) leaf area index (LAI) and chlorophyll content (C_{ab}), (B) gross primary production (GPP), (D and F) photochemical reflectance index affected and not affected by xanthophyll cycle de-epoxidation (PRI_{xan}^{scope} , PRI_0^{scope}) and (H and J) far-red fluorescence simulated with and without fluorescence amplification factor ϕ_f (F_{760}^{scope} , $F_{0,760}^{scope}$). Colour lines represent mean daily values for T_{air} , VPD and PAR, and mean daily values in the time interval between 10 and 3 pm for GPP, PRI_{xan}^{scope} , PRI_0^{scope} , F_{760}^{scope} , $F_{0,760}^{scope}$.

3.3.2.2. ΔPRI^{scope} and ΔF_{760}^{scope} as a function of vegetation physiological response

The difference between total PRI_{xan}^{scope} and constitutive PRI_0^{scope} denoted as ΔPRI^{scope} (Table 5) represents a facultative response of a plant to environmental conditions (e.g. changing irradiance) occurring at daily or shorter timescales. ΔPRI^{scope} can be considered a reliable proxy of the changing DEPS of xanthophyll cycle pigments as part of NPQ. The SCOPE-simulated weighted

average of all leaves NPQ linearly scales with ΔPRI^{scope} at short temporal scale when canopy structural parameters (LAI) do not vary significantly (Fig. 14B). The coefficient of determination (R^2) of the linear relationships between ΔPRI^{scope} and NPQ computed for classes of LAI of equal size (approx. 600 data points per class) varies within a range of 0.75 – 0.97.

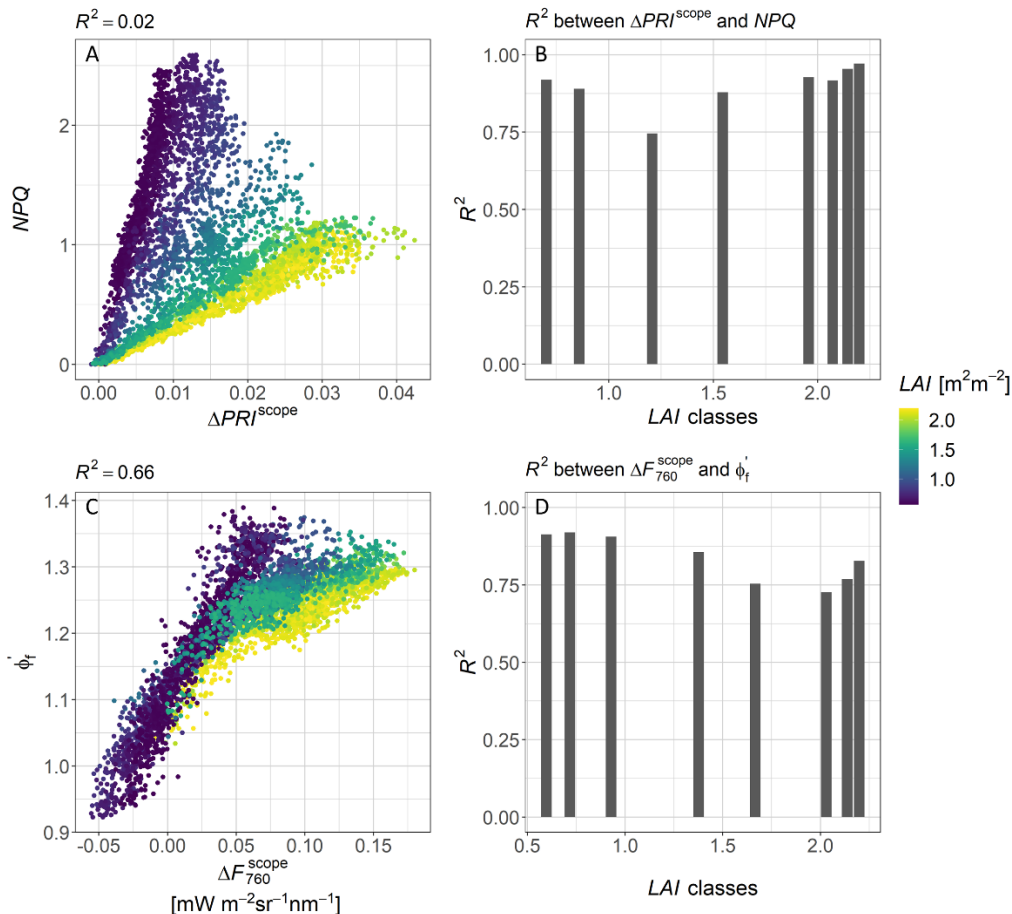


Figure 14. (A) Relationship between ΔPRI^{scope} and NPQ and (B) coefficients of determination (R^2) for linear relationships between ΔPRI^{scope} and NPQ aggregated by LAI classes of equal size. (C) Relationship between ΔF_{760}^{scope} and ϕ'_f and (D) coefficients of determination (R^2) for linear relationships between ΔF_{760}^{scope} and ϕ'_f aggregated by LAI classes of equal size. The data presented on the figure correspond to daytime data, $SZA \leq 80^\circ$ and the fraction of the day between 0.2 and 0.8.

In order to validate the decomposition of F_{760}^{scope} into components related either to biochemical or physiological properties, we used the difference (ΔF_{760}^{scope}) between F_{760}^{scope} and $F_{0,760}^{scope}$ as a reference for the physiological information contained in fluorescence signal. F_{760}^{scope} is scaled with fluorescence efficiency factor predicted by biochemical model according to the way $aPAR_{Cab}$ is dissipated in the photosynthetic machinery. Therefore, the remaining variability of ΔF_{760}^{scope} can be attributed to physiological regulation of fluorescence efficiency (Fig. 14C). R^2 of the linear relationships between ΔF_{760}^{scope} and ϕ'_f computed for classes of LAI of equal size (approx. 600 data points per class) varies within a range of 0.73 – 0.92 (Fig. 14D).

For the decomposition analysis we assume that the scaling of canopy-level parameters $\Delta PRI_{\text{scope}}$ and $\Delta F_{760}^{\text{scope}}$ to leaf-level NPQ and ϕ'_f is not necessary if the relationship between decomposed SSA-components and NPQ and ϕ'_f is assessed for different LAI classes.

3.3.2.3. Proof of concept : extraction of slow dynamics from $PRI_{\text{xan}}^{\text{scope}}$, F_{760}^{scope} and $Fy^{*\text{scope}}_{760}$ with SSA

Slow-varying component of $PRI_{\text{xan}}^{\text{ssa}}$ [seasonal] extracted with SSA showed a high correlation with PRI_0^{scope} ($R^2 = 0.97$) (Fig. 15A).

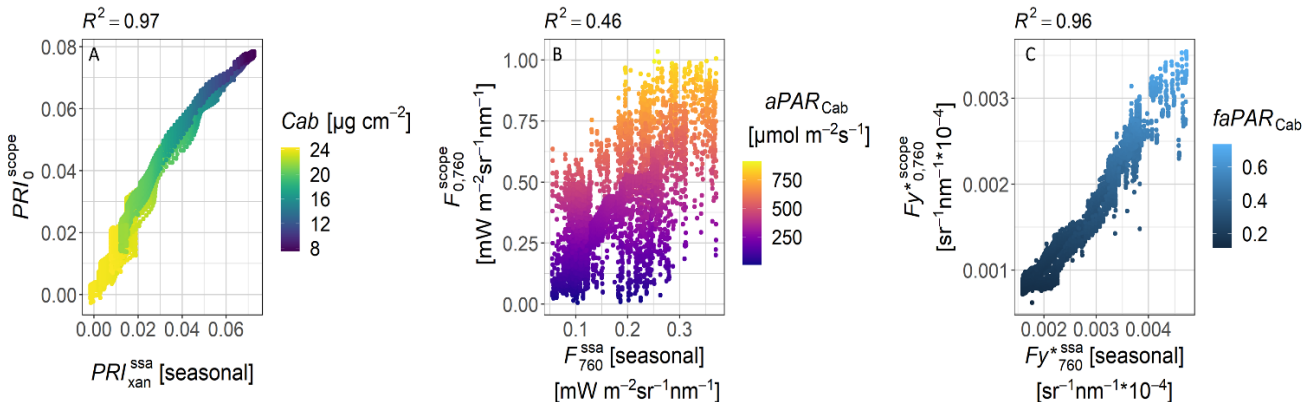


Figure 15. (A) Relationship between $PRI_{\text{xan}}^{\text{ssa}}$ [seasonal] and PRI_0^{scope} , (B) F_{760}^{ssa} [seasonal] and F_{760}^{scope} , and (C) $Fy^{*\text{ssa}}_{760}$ [seasonal] and $Fy^{*\text{scope}}_{760}$. The data presented on the figure correspond to daytime data, $SZA <= 80^\circ$ and the fraction of the day between 0.2 and 0.8.

This confirms that SSA was able to separate the long-term variability of $PRI_{\text{xan}}^{\text{scope}}$ induced by seasonally varying structural and biochemical vegetation properties (C_{ab}). The SSA extraction of the seasonal component from F_{760}^{scope} performed worse in comparison to $PRI_{\text{xan}}^{\text{scope}}$, with $R^2 = 0.46$ of the relationship between F_{760}^{ssa} and F_{760}^{scope} (Fig. 15B). Decomposition of $Fy^{*\text{scope}}_{760}$ allowed to separate seasonal cycle associated with the variability of $f\text{aPAR}_{\text{Cab}}$. High positive correlation was observed between $Fy^{*\text{ssa}}_{760}$ [seasonal] and $Fy^{*\text{scope}}_{760}$ ($R^2 = 0.96$) (Fig. 15C).

3.3.2.4. Proof of concept: extraction of fast variability from $PRI_{\text{xan}}^{\text{scope}}$, F_{760}^{scope} and $Fy^{*\text{scope}}_{760}$ with SSA

Fast-varying component of $PRI_{\text{xan}}^{\text{ssa}}$ [diurnal + sub-diurnal] showed a strong linear correlation with $\Delta PRI^{\text{scope}}$ ($R^2 = 0.78$) (Fig. 5A). In order to understand if the relationship found is not spurious, and if the information extracted by SSA is related to physiological responses of vegetation, we applied the same decomposition on PRI_0^{scope} , and found no significant correlation with $\Delta PRI^{\text{scope}}$ ($R^2 = 0.05$) (Fig. 17A). This supports the hypothesis that SSA can be useful for separating the fast variability of PRI attributed to the activation of xanthophyll cycle as part of the reversible NPQ . The fast SSA component F_{760}^{ssa} [diurnal + sub-diurnal] showed a significant correlation with $\Delta F_{760}^{\text{scope}}$ for LAI from 1.4 up to 2.2 $\text{m}^2 \text{m}^{-2}$ with R^2 ranging from 0.27 to 0.65 (Fig. 16B, E).

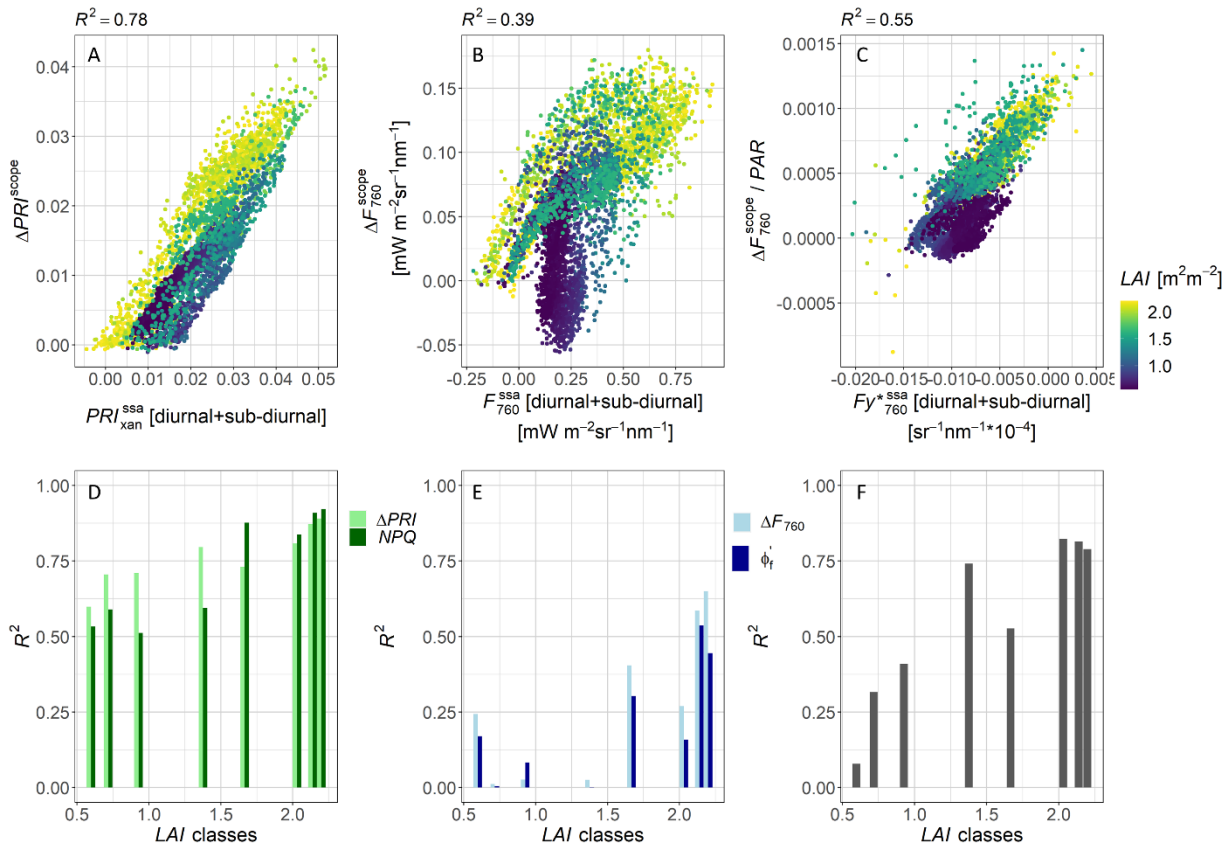


Figure 16. (A) Relationship between $PRI_{\text{xan}}^{\text{ssa}}$ [diurnal + sub-diurnal] and $\Delta PRI_{\text{scope}}$ and R^2 for linear relationships $PRI_{\text{xan}}^{\text{ssa}}$ [diurnal + sub-diurnal] vs PRI_{scope} and $PRI_{\text{xan}}^{\text{ssa}}$ (30 min – 1 week) vs NPQ aggregated by LAI classes of equal size (D); (B) F_{760}^{ssa} [diurnal + sub-diurnal] and $\Delta F_{760}^{\text{scope}}$ and R^2 for linear relationships aggregated by LAI classes of equal size (E); (C) $F_{760}^{*\text{ssa}}$ [diurnal + sub-diurnal] and $\Delta F_{760}^{\text{scope}} / \text{PAR}$ and R^2 for linear relationships aggregated by LAI classes of equal size (F). The data presented on the figure correspond to daytime data, SZA <= 80° and the fraction of the day between 0.2 and 0.8.

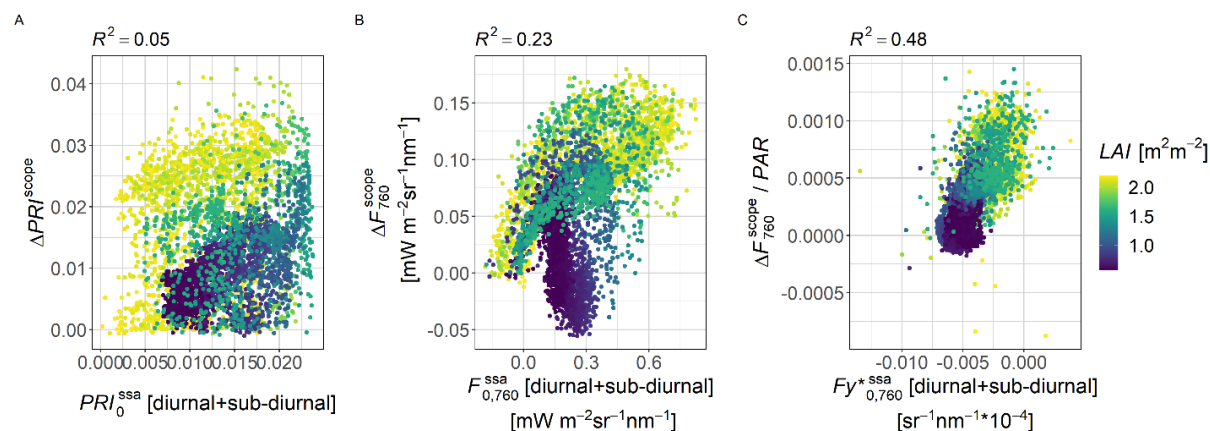


Figure 17. (A) Relationship between PRI_0^{ssa} [diurnal + sub-diurnal] and $\Delta PRI_{\text{scope}}$; (B) F_{760}^{ssa} [diurnal + sub-diurnal] and $\Delta F_{760}^{\text{scope}}$; (C) $F_{760}^{*\text{ssa}}$ [diurnal + sub-diurnal] and $\Delta F_{760}^{\text{scope}} / \text{PAR}$. The data presented on the figure correspond to daytime data, SZA <= 80° and the fraction of the day between 0.2 and 0.8.

During the periods associated with low LAI , which coincide also with high T_{air} and VPD , decomposition did not yield satisfying results. During summer months the diurnal cycles of $\Delta F_{760}^{\text{scope}}$ change shape, featuring minimum instead of maximum absolute values around midday (Fig. 18).

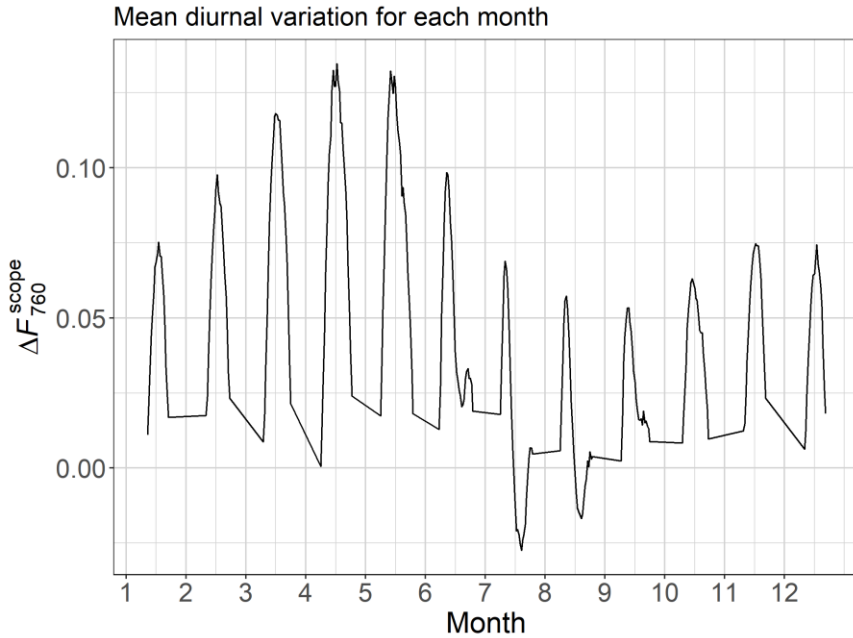


Figure 18. Mean diurnal variation of $\Delta F_{760}^{\text{scope}}$ computed for each month.

Negative values of $\Delta F_{760}^{\text{scope}}$ appear in the afternoon, which means that the model predicts lower fluorescence emission than the reference $F_{0,760}^{\text{scope}}$. This fact can be due to strong water stress and dissipation of the major part of the energy via NPQ . With SSA we are unable to extract this peculiar diurnal patter of $\Delta F_{760}^{\text{scope}}$ from F_{760}^{scope} . The fast component of Fy_{760}^{*ssa} [diurnal + sub-diurnal] linearly scales with $\Delta F_{760}^{\text{scope}} / PAR$ ($R^2=0.55$) (Fig. 16C). Unlike F_{760}^{scope} , fast component of Fy_{760}^{*ssa} exhibited strong correlation with $\Delta F_{760}^{\text{scope}} / PAR$ for all LAI classes varying from 0.32 for LAI between 0.6 and 0.7 $m^2 m^{-2}$ to 0.82 for $LAI > 2 m^2 m^{-2}$. To ascertain that Fy_{760}^{*ssa} [diurnal + sub-diurnal] is related to physiological response, we applied that same SSA decomposition on $Fy_{0,760}^{\text{scope}}$, and in this case the components of the same frequency showed lower correlation with $\Delta F_{760}^{\text{scope}} / PAR$ ($R^2=0.48$) (Fig. 17C).

3.3.2.5. Link between fast SSA components of $PRI_{\text{xan}}^{\text{scope}}$, F_{760}^{scope} , Fy_{760}^{*scope} and light-use efficiency
In order to evaluate whether SSA-decomposed fast components of optical signals are better related to physiological response of vegetation than the TOC raw signals, we examined their relationships with LUE . Extraction of the slow component from $PRI_{\text{xan}}^{\text{scope}}$ eliminated the effect of a strong variability of intercepts observed in the relationship between $PRI_{\text{xan}}^{\text{scope}}$ and LUE (Fig. 19A). The fast component PRI_{xan}^{ssa} [diurnal + sub-diurnal] better linearly correlates with LUE in comparison to undecomposed total $PRI_{\text{xan}}^{\text{scope}}$ when the relationships are considered for moving window of 20 days (Fig. 6C). The moving window of 20 days was chosen to account for variations in structural and biochemical properties as in (Soudani et al., 2014). $dCor$ between PRI_{xan}^{ssa} [diurnal + sub-diurnal] and

LUE computed over the moving window of 20 days shows that the values vary within a range of 0.70 - 0.95, except a decrease down to 0.30 at DOY 260 - 300 (Fig. 19C).

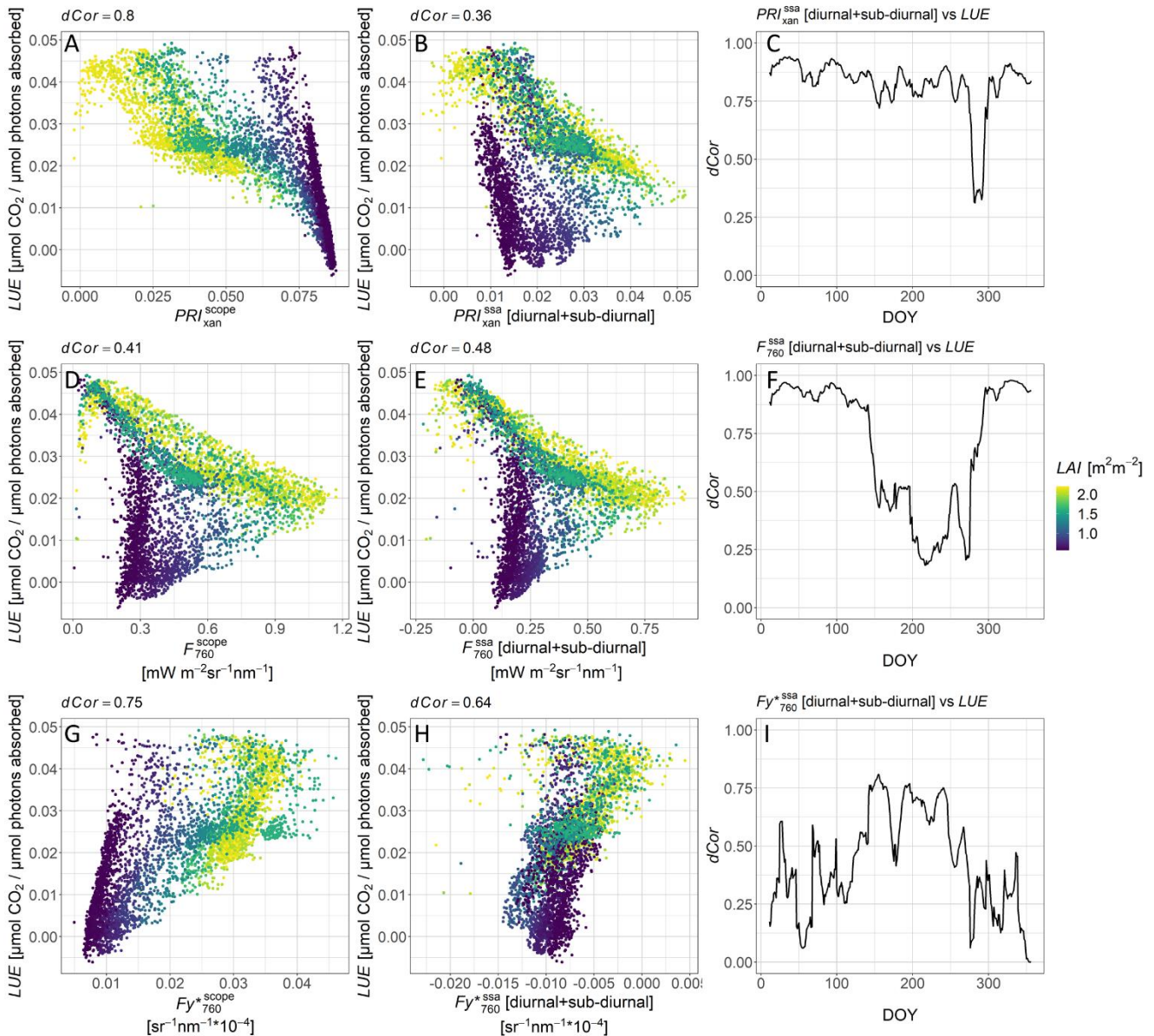


Figure 19. First row: relationships between PRI_{xan}^{scope} and LUE (A), PRI_{xan}^{ssa} [diurnal+sub-diurnal] and LUE (B) and distance correlation ($dCor$) between the two computed using moving window of 20 days (C). Second row: relationships between F_{760}^{scope} and LUE (D), F_{760}^{ssa} [diurnal+sub-diurnal] and LUE (E) and distance $dCor$ between the two computed using moving window of 20 days (F). Third row: relationships between Fy_{760}^{scope} and LUE (G), Fy_{760}^{ssa} [diurnal+sub-diurnal] and LUE (H) and $dCor$ between the two computed using moving window of 20 days (I).

The fast component extracted from F_{760}^{scope} - F_{760}^{ssa} [diurnal + sub-diurnal] – negatively correlates with LUE with high $dCor$ (0.50 - 0.90) during the periods characterized by high LAI (Fig. 19D-F). Time series of $dCor$ computed for moving window of 20 days (Fig. 19F) follows LAI and C_{ab} seasonal cycles (Fig. 13I), which implies that the SSA decomposition of F_{760}^{scope} is more robust for denser canopy. The decoupling of the Fy_{760}^{ssa} [diurnal + sub-diurnal] component from Fy_{760}^{scope} allowed to decrease the scatter in the relationship between Fy_{760}^{scope} and LUE (Fig. 19G, H). Time series of $dCor$ of the

relationships between Fy^{*scope}_{760} and LUE computed over 20 days moving average showed the pattern which follows major oscillations of NPQ seasonal cycle (Fig. 19I). The control of the NPQ over this relationship is evident when we consider two NPQ classes – lower and higher than 0.1. Under low $NPQ < 0.1$ associated with low light conditions the correlation is negative (Pearson correlation coefficient (R) = -0.55; $dCor=0.53$), (Fig. 20A), while for NPQ varying between 0.1 and 2.5 the correlation is positive ($R = 0.69$, $dCor=0.75$) (Fig. 20B).

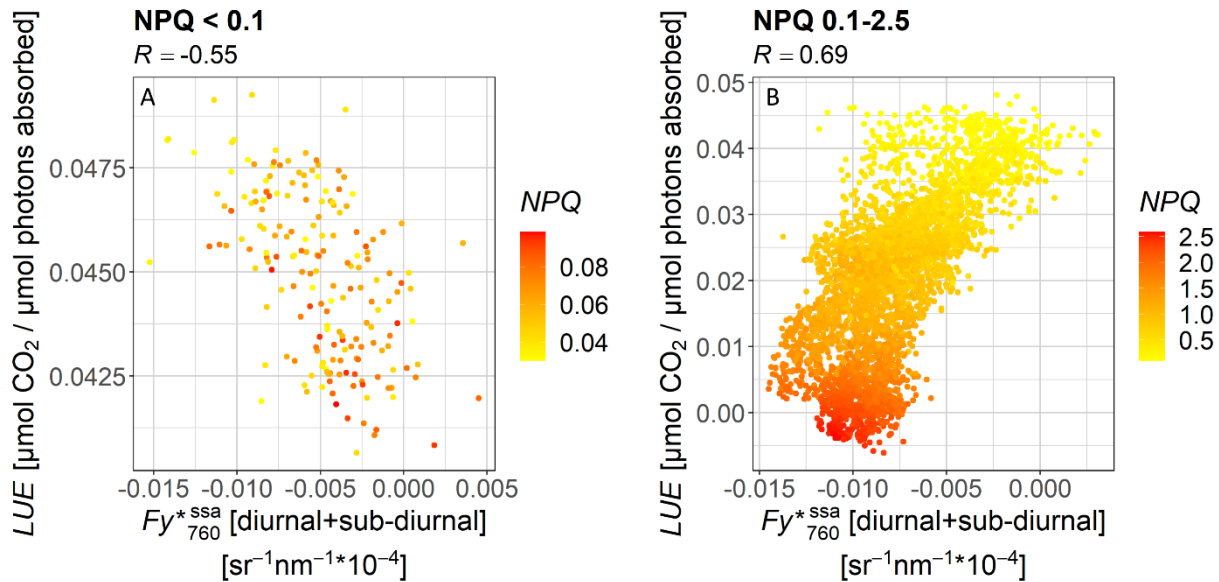


Figure 20. Relationship between Fy^{*ssa}_{760} [diurnal+sub-diurnal] and LUE computed for $NPQ < 0.1$ (A) and NPQ between 0.1 and 2.5 (B).

3.3.3. Discussion

3.3.3.1. Performance of SSA in separation of seasonal and fast dynamics in optical signals

With the increasing availability of high temporal resolution optical data collected simultaneously with CO₂ fluxes at eddy covariance stations (Balzarolo et al., 2011; Gamon, et al., 2006), it is pivotal to accurately interpret information provided by these datasets. Optical signal and particularly PRI and F are affected by confounding factors acting at different time scales (Gamon & Berry, 2012). To our knowledge, there were no previous attempts to use time series decomposition as tool to disentangle physiological information from these signals.

Our approach shows that SSA decomposition of PRI_{xan}^{scope} , F_{760}^{scope} and Fy^{*scope}_{760} simulated with SCOPE for a specific case study of Mediterranean grassland ecosystem allowed to separate slow and fast varying components with different levels of accuracy. Following the concept that there are two components of PRI variability – constitutive and facultative – introduced in Gamon and Berry (2012), we showed that these components can be successfully distinguished using highly data-adaptive SSA technique. The decomposed slow variability of the total PRI_{xan}^{scope} showed high correlation with constitutive PRI_0^{scope} (Fig. 15A), which is highly correlated with modified red-edge normalized difference index ($mNDI$) sensitive to chlorophyll content ($R^2=0.94$) (Sims & Gamon, 2002). This result is similar to the strong relationships emerging between PRI of perfectly dark adapted leaves and

mNDI obtained in Hmimina et al. (2014, 2015) and Merlier et al. (2015) at both leaf and canopy scales. The facultative variability $\Delta PRI^{\text{scope}}$ was well predicted by the fast component $PRI_{\text{xan}}^{\text{ssa}}$ extracted with SSA and varying at diurnal and sub-diurnal timescales (Fig. 16A). The physiological meaning of $PRI_{\text{xan}}^{\text{ssa}}$ [diurnal+sub-diurnal] was assessed by relating it to *NPQ* and *LUE*. Since *NPQ* is a leaf-level parameter, we computed the relationships with $PRI_{\text{xan}}^{\text{ssa}}$ [diurnal+sub-diurnal] based on *LAI* classes (Fig. 16D) to overcome the problem of downscaling from canopy- to leaf-level. The overall high R^2 (Fig. 16D) gradually increased from low to high *LAI* values. In the modelled dataset, summer season is characterized by low *LAI* and low water availability with highly variable *VPD* values (daily range of 0–75 hPa) (Fig. 13C) and *NPQ* (daily range of 0–2.6). Under these severe conditions, there is a lack of *PRI* response to increasing *PAR*, which might explain lower correlation between $PRI_{\text{xan}}^{\text{ssa}}$ [diurnal+sub-diurnal] and *NPQ* at this period of the year. As shown on (Fig. 19A), total $PRI_{\text{xan}}^{\text{ssa}}$ and *LUE* exhibit a non-linear relationship with variability in intercepts between *LAI* classes. Fast component of $PRI_{\text{xan}}^{\text{ssa}}$ [diurnal+sub-diurnal], in turn, linearly correlates with *LUE* when the relationships are considered for the periods of the stable canopy structure (Fig. 19B, C). In contrast to the works of Hmimina et al. (2014, 2015), where the evaluation of the relationships of total and pigment-corrected *PRI* with *LUE* were performed for short periods excluding sources of significant changes in the *LAI*, we assessed the SSA decomposition under varying *LAI*. The fast variability $PRI_{\text{xan}}^{\text{ssa}}$ [diurnal+sub-diurnal] may contain different sources of variation. On the one hand, $PRI_{\text{xan}}^{\text{ssa}}$ [diurnal+sub-diurnal] responds to diurnal and sub-diurnal variations of *NPQ* driven by instantaneous changes in light intensity (Krause & Weis, 1991) and modulated by *VPD* and T_{air} (Demmig-Adams & Adams, 1992); on the other hand, these are mixed with directional effects imposed on diurnal cycles of *PRI* (Biriukova et al., 2020a; Hall et al., 2008; Hilker et al., 2008). Both processes vary in the same frequency bin and only change in amplitude, and SSA is unable to separate these two components.

The applicability of SSA for the decoupling of slow and fast dynamics in *F* was evaluated for both F_{760}^{scope} and $Fy_{760}^{*\text{scope}}$. First, we attempted to disentangle *aPAR*-related and physiology-related variabilities in F_{760}^{scope} . *F* variability driven only by biophysical vegetation properties and irradiance ($F_{0,760}^{\text{scope}}$) was not accurately disentangled with F_{760}^{ssa} [seasonal] ($R^2=0.46$) (Fig. 15B). Fast physiological component was only extracted for the growing period where vegetation is more active, and *LAI* is larger than 2 m² m⁻² (Fig. 16B, E). The problem with decomposition of F_{760}^{scope} with SSA can be explained by the fact that both F_{760}^{scope} and $F_{0,760}^{\text{scope}}$ are strongly driven by *aPAR* and are highly correlated with each other ($R^2=0.98$). Therefore, the contribution of *aPAR*-related variability and physiology-related component is hard to decouple since both are driven by diurnal cycles of irradiance. By normalizing F_{760}^{scope} with *PAR* we remove a part of variability attributed to irradiance, and thus reduce the number of unknown variables in Eq. 9.

We hypothesized, that by decomposing $Fy_{760}^{*\text{scope}}$, we can remove a part of the variability attributed to *faPAR_{cab}* and to infer information related to fluorescence efficiency ϕ'_{f} . Seasonal variability, associated with *faPAR_{cab}* (R^2 of the relationship between $Fy_{0,760}^{*\text{scope}}$ and *faPAR_{cab}* is 0.99) was captured by the SSA-reconstructed $Fy_{760}^{*\text{ssa}}$ [seasonal] (Fig. 15C). The remaining variability attributed to physiological modulation of $\Delta F_{760}^{\text{scope}}$ normalized by *PAR* was considerably better predicted by

Fy^{*ssa}_{760} [diurnal+sub-diurnal] (Fig. 16C, F) in comparison to the relationship between F_{760}^{ssa} [diurnal+sub-diurnal] and ΔF_{760}^{scope} (Fig. 16B, E). Moreover, $dCor$ between Fy^{*ssa}_{760} [diurnal+sub-diurnal] and LUE computed using moving average of 20 days follows the major changes in NPQ times series (Fig. 19I). Under high light conditions, when NPQ is actively involved in $aPAR_{Cab}$ dissipation, it becomes a determinant factor in the relationship between ϕ_p and ϕ'_f . In contrast, under low light conditions, when NPQ is low and constant, the driving factor of this relationship is photochemical quenching (PQ) (Porcar-Castell et al., 2014). Decreasing PQ and increasing NPQ affect ϕ'_f in opposite ways (C. van Der Tol et al., 2014) and, as a result, the relationship between photochemical yield (and hence LUE) and ϕ'_f is positive under NPQ control and negative under PQ control. This behaviour, observed in the relationship between leaf-level parameters ϕ_p and ϕ'_f (Fig. 21), can be also seen in the relationship between SSA-decomposed fast Fy^{*ssa}_{760} [diurnal+sub-diurnal] and LUE (Fig. 20).

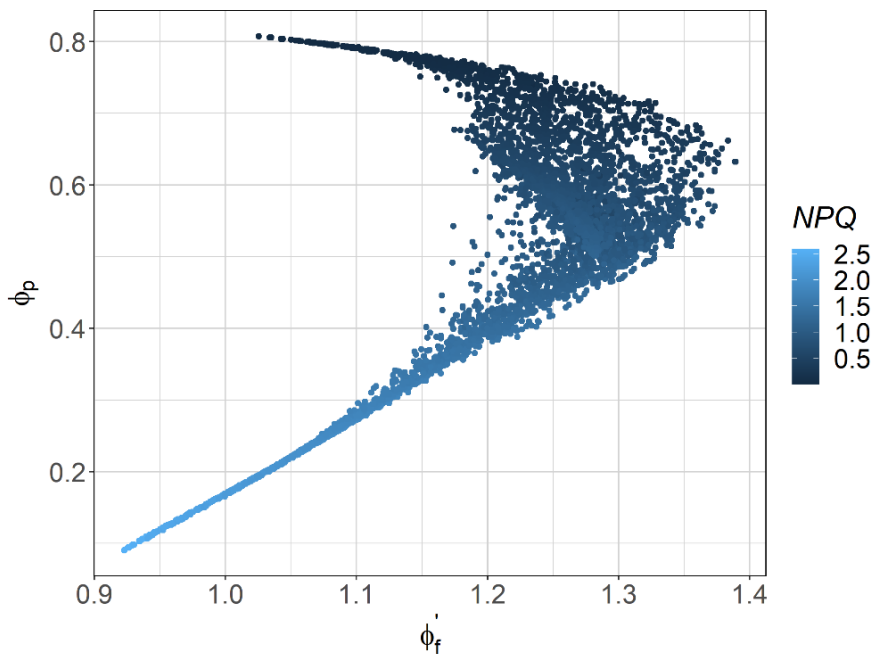


Figure 21. Relationship between fluorescence efficiency (ϕ'_f) and photochemical yield (ϕ_p). The data presented on the figure correspond to daytime data , with PAR values $\geq 500 \mu\text{mol m}^{-2} \text{s}^{-1}$, SZA $\leq 80^\circ$ and the fraction of the day between 0.2 and 0.8.

These results suggest that Fy^{*ssa}_{760} [diurnal+sub-diurnal] can be attributed to physiologically-related information contained in fluorescence signal. Previous works have proved the feasibility of ϕ'_f extraction from TOC F signal using radiative transfer model inversion (van der Tol et al., 2016; Celesti et al., 2018). SSA-based approach is a step forward in decoupling physiological information from optical variables measured with automated proximal systems without complex and computationally demanding model inversions.

The choice of SSA decomposition parameters plays an important role on the resulting reconstructed time series. The decomposition can be potentially improved by varying the “cut-offs” of the frequency bins (Table 6) in which we aim to extracting the subsignals. Here we tested different frequency bins of varying length and borders and have heuristically chosen broader bins covering three timescales interesting from ecological point of view – seasonal, diurnal, and sub-diurnal.

Depending on the time series length and temporal resolution, the borders of the frequency bins of interest might be expanded (e.g. if time series sampling frequency is lower there is no need detect sub-diurnal component) or narrowed (e.g. in case of sampling frequency higher than 30 min would be interesting to have several bins per day to explore the dynamics of the fast physiological response at different timescales during a day).

3.3.3.2. Limitations and applicability to field data

This study is a model-based proof of concept for decoupling slow dynamics related to biochemical composition and structural changes and fast physiological dynamics in TOC time series of F and PRI . We chose a model-based study because the data required for the evaluation of the proposed decomposition technique (i.e. a combination of canopy scale passive and leaf-level active measurements) are only sparsely available and prone to uncertainty related to the scaling from leaf-to canopy-level processes such as NPQ . In this context, with the use of a synthetic data generated by a state-of-the-art process-based model, we can evaluate if our method is able to disentangle the processes acting at different time scale as encoded in the model. This kind of model-based evaluation was already used for different problems but in similar condition where there was a lack of evaluation dataset (e.g. Nelson et al., 2018). However, it should be noted, that the SCOPE is not a dynamic model, which implies that some of the physiological responses (i.e. sustained NPQ) that can be observed in the field are not captured by the model. When analysing the links between decomposed PRI and NPQ , it should be taken into account that NPQ involves mechanisms operating at different temporal scales, such as reversible energy-dependant NPQ with over-night relaxation and sustained NPQ operating at longer timescales (Porcar-Castell, 2011). However, predicting NPQ based on PRI is only possible when reversible NPQ is dominating and sustained NPQ is insignificant (Alonso et al., 2017). In SCOPE simulations we kept a constant rate of sustained NPQ , so that modelled NPQ only includes the effect of xanthophyll cycles activation. Therefore, when applying SSA on field data, one should consider that decomposed fast components of PRI may not represent the full variability of NPQ . Additional considerations are associated with the parameterization of SCOPE fluorescence module with datasets limited to few species (i.e. cotton), which may also affect the accuracy of the representation of physiological response of the grassland. Nevertheless, we assume that for the purpose of the decomposition of slow and fast temporal dynamics of F and PRI with SSA, a simple simulation was reasonable.

Further, we discuss the applicability of the method to field data and associated limitations. SSA decomposition requires high temporal resolution data, acquired with at least 1 hour - 30 min interval to track fast physiological response of F and the activation of xanthophyll cycle, occurring at timescales of minutes after the change in light intensity (Müller et al., 2001). In general, the higher the temporal resolution of time series, the more accurate extraction of fast varying physiological components can be achieved. With the expanding network of automated proximal sensing systems (Aasen et al., 2019; Cogliati, Rossini, et al., 2015), continuous and high-resolution time series of F and R become increasingly available.

These systems can be used to acquire time series of PAR , PRI , and F , as well as normalized vegetation indices informing on vegetation structure. Often, these systems are installed close to eddy

covariance sites, which provide measurements of net ecosystem exchange (*NEE*), partitioned on *GPP* and respiration, and auxiliary abiotic variables (Rebmann et al., 2018) useful for the evaluation of the method's performance under different environmental conditions. Some eddy covariance sites also provide measurements of *aPAR*, but often this term has to be modelled from remote sensing observations, which is still challenging. Apparent *LUE* (*GPP/PAR*) and fluorescence yield Fy^* (F/PAR) are usually easier to obtain in comparison to metrics derived using *aPAR* or $aPAR_{\text{Cab}}$. As shown in Gitelson and Gamon (2015) *LUE* computed as *GPP/PAR* is the most confounded by canopy structure among other *LUE* formulations, while *LUE* computed as *GPP/aPAR_{cab}* mostly depends on the physiological status of vegetation. *aPAR* can be estimated using several downward and upward-facing quantum sensors installed above and below the canopy (Inoue et al., 2008; Jenkins et al., 2007) or using automated observation system based on LED sensors (Kim, Ryu, Jiang, & Hwang, 2019). $aPAR_{\text{Cab}}$ can be effectively retrieved from field spectral reflectance and transmittance measurements (Serrano et al., 2000), directly measured with destructive sampling, or approximated using vegetation greenness indices (e.g. *NDVI*), however, there is still no standard procedure that could be used to accurately estimate $aPAR_{\text{Cab}}$. In this study we showed the applicability of the SSA decomposition on commonly available Fy^*_{760} and evaluated its relationship with *LUE* computed as *GPP/aPAR_{cab}* in order to assess whether the fast component of Fy^*_{760} is related to physiological status of vegetation. In case $aPAR_{\text{Cab}}$ is not available from field observations, SSA decomposition of apparent *LUE* (*GPP/PAR*) can be used to decouple the influence of canopy biochemical and structural properties on *LUE*.

In addition to time series of optical variables, leaf-level pulse - PAM measurements of *NPQ*, ϕ_f and ϕ_p would be greatly beneficial for the validation of the decomposition results. For example, simultaneous installation of automated high spectral resolution devices (e.g. FloX system, JB Hyperspectral Devices UG, Germany) with micro-PAM (Atherton et al., 2016; Magney et al., 2017; Porcar-Castell et al., 2008) can provide a dataset for the validation of the method. However, the availability of these coupled datasets is still very limited.

Since SSA requires data continuity, gap filling should be applied to time series with missing values. For this purpose, SSA has been also successfully used as a gap-filling tool (Buttlar et al., 2014; Mahecha et al., 2007). The classical SSA algorithm was modified so that SSA components are estimated based on non-missing values only, and the values of the reconstructions are imputed to missing values (Golyandina and Osipov, 2007). For night-time data, a noisy baseline should be provided as well, for example, by linearly interpolating the last daytime observation of a day and the first daytime observation of the following day, or by applying moving window to smooth a baseline.

3.4. Case study: application of SSA to measured time series of optical signals

3.4.1. Methods

3.4.1.1. Study site

The study site is located near Gebesee in Thuringia, Germany ($51^{\circ}06'0.13''N$, $10^{\circ}54'51.9''E$) in the middle of an agricultural field of approximate area of 750 m by 850 m (Anthoni et al., 2004). Established in 2001, this site is the eldest cropland eddy covariance site in Europe (Kutsch, Brümmer, Don, Dechow, & Fuß, 2013), which was included in Integrated Carbon Observation System (ICOS) in 2013. Winter wheat (*Triticum aestivum*) was drilled on the 23^d of October 2018, emerged in the beginning of April 2019, and was harvested in the mid-July 2019.

3.4.1.2. Spectral measurements and data processing and F retrieval

Spectral measurements were acquired with the high-resolution fluorescence box (FloX) device (JB Hyperspectral Devices UG, Germany) specifically designed for retrieving F and vegetation indices in visible (VIS) and near-infrared (NIR) domains. The FloX contains two spectrometers – QE Pro (wavelength range of 650 - 813 nm, spectral sampling interval (SSI) of 0.15 nm and full width at half maximum (FWHM) of 0.3 nm), Flame (wavelength range of 340- 1020 nm, SSI = 0.65 nm, FWHM = 1.5 nm) (Ocean Optics, USA). Hereafter the variables acquired from QE Pro feature suffix “fluo”, and variables acquired from Flame feature suffix “full”. The up-welling radiance was measured with the field of view (FOV) of fiber optics of 25°. Down-welling irradiance was measured using cosine receptors with FOV of 180°. One acquisition cycle consisted of a series of measurements acquired sequentially by each spectrometer : 1) down-welling irradiance (E^{\downarrow}_1), 2) up-welling radiance (L^{\uparrow}), 3) down-welling irradiance (E^{\downarrow}_2), 4) dark current. The second measurement of down-welling irradiance allows to evaluate the stability of the illumination conditions and is used for following in data filtering procedure. Signal optimization is performed for each acquisition cycle for adaptation to varying light conditions allowing for maximized signal-to-noise ratio.

The FloX was installed on the pole of 2 m height pointing towards south-west (Fig. 22). The resulting radiometric footprint of approximately 90 cm in diameter. The FloX system was installed on the 10th of April 2019 and disassembled on the 17th of July 2019, covering the whole phenological cycle of winter wheat development from emergence to harvest. Measurements were acquired continuously from 9 am until 8 pm local time with an interval from 20 sec (under bright sunshine) to 60 sec (in overcast conditions).



Figure 22. The FloX installed over the winter wheat field in Gebesee, Germany. The photo is taken in the 3^d of June 2019.

Raw data processing was performed in R software (R Core Team, 2019) using open source packages “FieldSpectroscopyDP” and “FieldSpectroscopyCC” available on GitHub (<https://github.com/tommasojulitta>). Before further analysis, the quality check of the dataset was implemented following the criteria reported in Table 7.

Quality index	Description	Threshold for retained data
E stability index Full	percentage change between E^{\downarrow}_1 and E^{\downarrow}_2	<=1%
E stability index Fluo	percentage change between E^{\downarrow}_1 and E^{\downarrow}_2	<=2%
SZA	Solar Zenith Angle	<=70
Dynamic range for both E^{\downarrow} and L^{\uparrow} in Fluo and Full spectrometers	ratio of the maximum value of E (or L) to the saturation values in percent	>=20% and <=90%

Table 7. Data quality indices and their corresponding thresholds for which data are retained.

F was retrieved in O₂A absorption band (F_{760}) using spectral fitting method (SFM) (Cogliati, Verhoef, et al., 2015; Meroni et al., 2010; Meroni & Colombo, 2006). Far-red fluorescence apparent yield (Fy^*_{760}) was computed as a ratio of F_{760} to photosynthetically active radiation (PAR).

Photochemical Reflectance Index (PRI) (Gamon et al., 1992) was computed as:

$$PRI = \frac{R_{570} - R_{531}}{R_{570} + R_{531}} \quad (16)$$

where R_{531} is the reflectance factor of the xanthophyll-sensitive band at 531 nm and R_{570} is reflectance factor of the reference band at 570 nm. With this formulation, PRI values can vary

between -1 and 1 and are directly proportional to *NPQ*. Fraction of photosynthetically active radiation absorbed (*fPAR*) was computed as a ratio of absorbed photosynthetically active radiation (*aPAR_{Li&Moreau}*) to *PAR*. *aPAR_{Li&Moreau}* was estimated following the formulation presented in Li and Moreau (1996) as the difference between incoming and reflected *PAR* multiplied by the proportion of canopy absorption (*RAPAR*):

$$aPAR_{Li\&Moreau} = (PAR_{inc} - PAR_{refl}) \times RAPAR \quad (17)$$

Where *RAPAR* was calculated as:

$$RAPAR = 0.105 - 0.323 \times NDVI + 1.468 \times NDVI^2 \quad (18)$$

Chlorophyll red-edge index (*CIre*) (Gitelson, Gritz, & Merzlyak, 2003) was computed as:

$$CIre = (R_{740}/R_{720}) - 1 \quad (19)$$

3.4.1.3. Eddy covariance flux measurements and meteorological data

CO_2 and water fluxes between vegetation and atmosphere were measured with eddy covariance (EC) technique (e.g. Baldocchi et al., 1996). Fluxes were measured with a gas analyzer LI-COR LI7200 (LI-COR Inc, Lincoln NE, USA), wind velocity was measured with an anemometer Gill HS-50 (Gill Instruments Ltd., Lymington, UK) both installed at 3 m height. Along with EC fluxes, the meteorological parameters were measured, such as air pressure (p , [hPa]) with pressure transmitter PTB101B (Vaisala), air temperature (T_{air} , [$^{\circ}\text{C}$]) and humidity (RH , [%]) with temperature-humidity-sensor HMP45D, (Vaisala, Vantaa, Finland), precipitation using heated tipping bucket rain gauge (Adolf Thies GmbH & Co. KG, Göttingen, Germany), *PAR* [$\mu\text{mol m}^{-2} \text{s}^{-1}$] with quantum sensor PQS1 (Kipp & Zonen B.V., Delft, The Netherlands). The vapor pressure deficit (*VPD*) was computed from T_{air} and RH . Soil water content (*SWC*, [$\text{m}^3 \text{m}^{-3}$]) was measured with soil moisture probes ML-2x, Delta-T (Delta-T Devices Ltd, Cambridge, UK).

Data gap-filling was performed with marginal distribution sampling (MDS) and the fluxes night-time partitioning was done based on the method described in Reichstein et al., 2005 implemented in Tovi software (www.tovi.io). The footprint of eddy covariance flux measurements was determined based on two-dimensional parameterization method described in Kljun et al., 2015 and implemented in Tovi (Fig. 23). The FloX was installed approximately 35 m away from the eddy tower (Fig. 23).

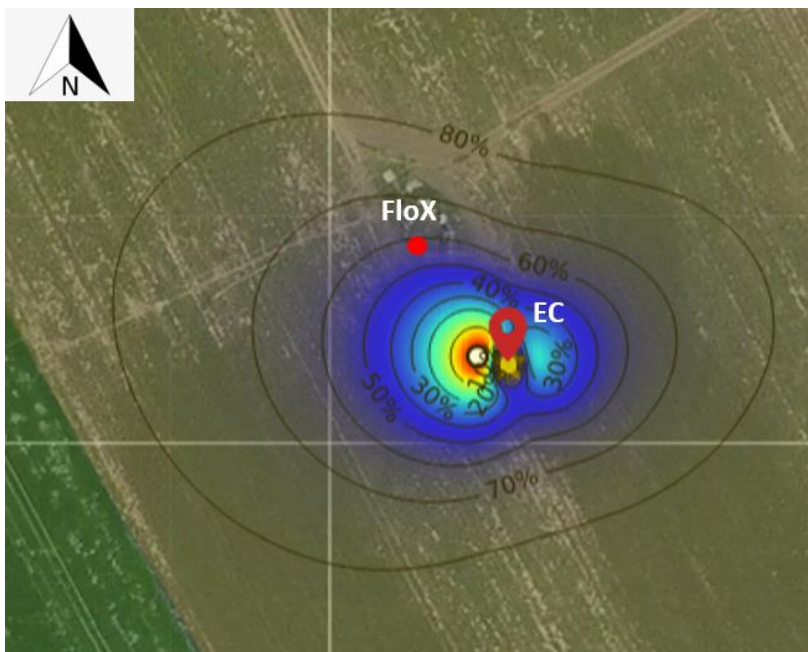


Figure 23. Site map with distribution of the peak flux footprint. The isolines and colours represent the percentiles of the distribution of the peak flux footprint in a particular sector.

Net ecosystem exchange (NEE , [$\mu\text{mol CO}_2 \text{ m}^{-2} \text{ s}^{-1}$]) was partitioned on gross primary production (GPP , [$\mu\text{mol CO}_2 \text{ m}^{-2} \text{ s}^{-1}$]) and ecosystem respiration (R_{eco} [$\mu\text{mol CO}_2 \text{ m}^{-2} \text{ s}^{-1}$]) using nighttime-based method (Reichstein et al., 2005). Based on the light-use efficiency model introduced by Monteith, 1972, GPP is a function of absorbed photosynthetically active radiation ($a\text{PAR}$) and light-use efficiency (LUE):

$$GPP = a\text{PAR} \times LUE \quad (20)$$

$a\text{PAR}$ is a product of PAR and the fraction of the fraction of photosynthetically active radiation absorbed ($fa\text{PAR}$). Since $a\text{PAR}$ is a parameter, which is not always measured at eddy covariance sites, we computed apparent LUE^* [$\mu\text{mol CO}_2 / \mu\text{mol photos of PAR}$] as ratio of GPP to PAR . Such definition is commonly adopted in remote sensing literature (e.g. Barton and North, 2001), however, LUE^* should be used with caution since is strongly influenced by seasonal patterns of leaf area index (LAI) and chlorophyll content (C_{ab}) (Gitelson & Gamon, 2015).

3.4.1.4. Acquisition of biochemical and structural parameters

At the beginning of the growing season (10th and 30th of April 2019), LAI was estimated via destructive sampling method. Wheat samples were collected from 25 x 25 cm quadrants and scanned with area meter (LI-3100C, LI-COR Inc, Lincoln NE, USA). Later in the growing season (5th and 24th of June and 10th of July 2019), LAI was measured with plant canopy analyzer LAI-2000 (LI-3100C, LI-COR Inc, Lincoln NE, USA). A single LAI value was calculated by averaging 3 measurements excluding 5th ring from the analysis.

During the same day as LAI measurements, we also estimated C_{ab} , [$\mu\text{g cm}^{-2}$], flavonols and anthocyanins content in relative absorbance units (varying from 0 to 3 for flavonols and 0 to 1.5 for anthocyanins) and Nitrogen Balanced Index, (NBI) computed as a ratio of C_{ab} to flavonols content using a leaf clip Dualex A (Force A, Orsay Cedex, France).

3.4.1.5. SSA decomposition

Prior to SSA decomposition, time series of spectral data was aggregated based on 30 min interval and matched with fluxes observations. Only 30 min intervals containing more than one observation were retained. Missing daytime data points were linearly interpolated for time series of *PRI*, F_{760} , Fy^*_{760} and *LUE**. Values at night-time gaps in time series of F_{760} were set to zero. Night-time baseline for *PRI*, F_{760} and *LUE** were filled with the minimum (for *PRI*) and maximum (for Fy^*_{760} and *LUE**) daytime values selected in the moving window of 1 day. Gaussian noise was added to the night-time data points in time series of *PRI*, F_{760} , Fy^*_{760} and *LUE** with mean (μ) equal 0 and standard deviation (σ) equal 95% quantile of daytime data multiplied by 0.01.

Similarly to model-based study, *PRI*, F_{760} , Fy^*_{760} and *LUE** were decomposed into three time-dependant components with SSA: long-term component varying in the frequency bin between 2 week and the length of the time series (82 days), diurnal component varying in the frequency bin between 7 hours and 2 weeks, and sub-diurnal component varying in the frequency bin between 30 min and 7 hours. The parameters of the decomposition used in the function *filterTSeriesSSA* are reported in the Table 8.

Argument	Description	Value
borders.wl	Borders of the different periodicity bands to extract. Units are the sampling frequency of the series (half-hourly observations).	4) 672, Inf (seasonal) 5) 14, 672 (diurnal) 6) 0, 14 (sub-diurnal)
M	Window length or embedding dimension. Units are the sampling frequency of the series (half-hourly observations).	Vector: (672,336,48)
n.comp	Amount of SSA components to compute.	Vector: (20, 20, 20)
harmonics	How many harmonics to include in each component.	Vector: (0,0,0)
repeat. extr	How often to repeat the extraction.	Vector: (2,1,1)
center.series	Whether to center the series around zero prior to the computation.	TRUE
grouping	Method to use for grouping the individual SSA eigentriples.	grouping.auto
groupingMethod	Method for automatic grouping.	wcor
SSA. methods	Methods to use for the SSA computation.	"auto" - Automatic method selection depending on the series length, window length, SSA kind and number of eigenvalues requested.

*Table 8. Parameters of filterTSeriesSSA (spectral.methods R-package (Jannis V Buttlar, 2015)) function used for the decomposition of PRI, F_{760} , Fy^*_{760} and LUE*.*

3.4.2. Results and discussion

3.4.2.1. Overview of seasonal cycles

During the period of measurements (Fig. 24), a strong gradient of daytime T_{air} was observed varying from -2°C in early April to 36°C in the end of July (Fig. 24A). While April and May were rather wet, in

summer SWC started to decline and VPD started to increase from 20 hPa to 67 hPa (Fig.24C, E) The peak of the wheat growing season occurred in the of May associated with the highest *GPP* of 60 [$\mu\text{mol m}^{-2} \text{s}^{-1}$] (Fig.24I). F_{760} generally followed the seasonal pattern of *GPP*, but the peak values were shifted a bit towards the first week of June (Fig.24H). *PRI* showed a strong seasonal cycle with sharply increasing values starting from the 10th of June (Fig.24F). *LUE** and Fy^*_{760} showed a decreasing trend starting from the beginning of summer (Fig.24D,J).

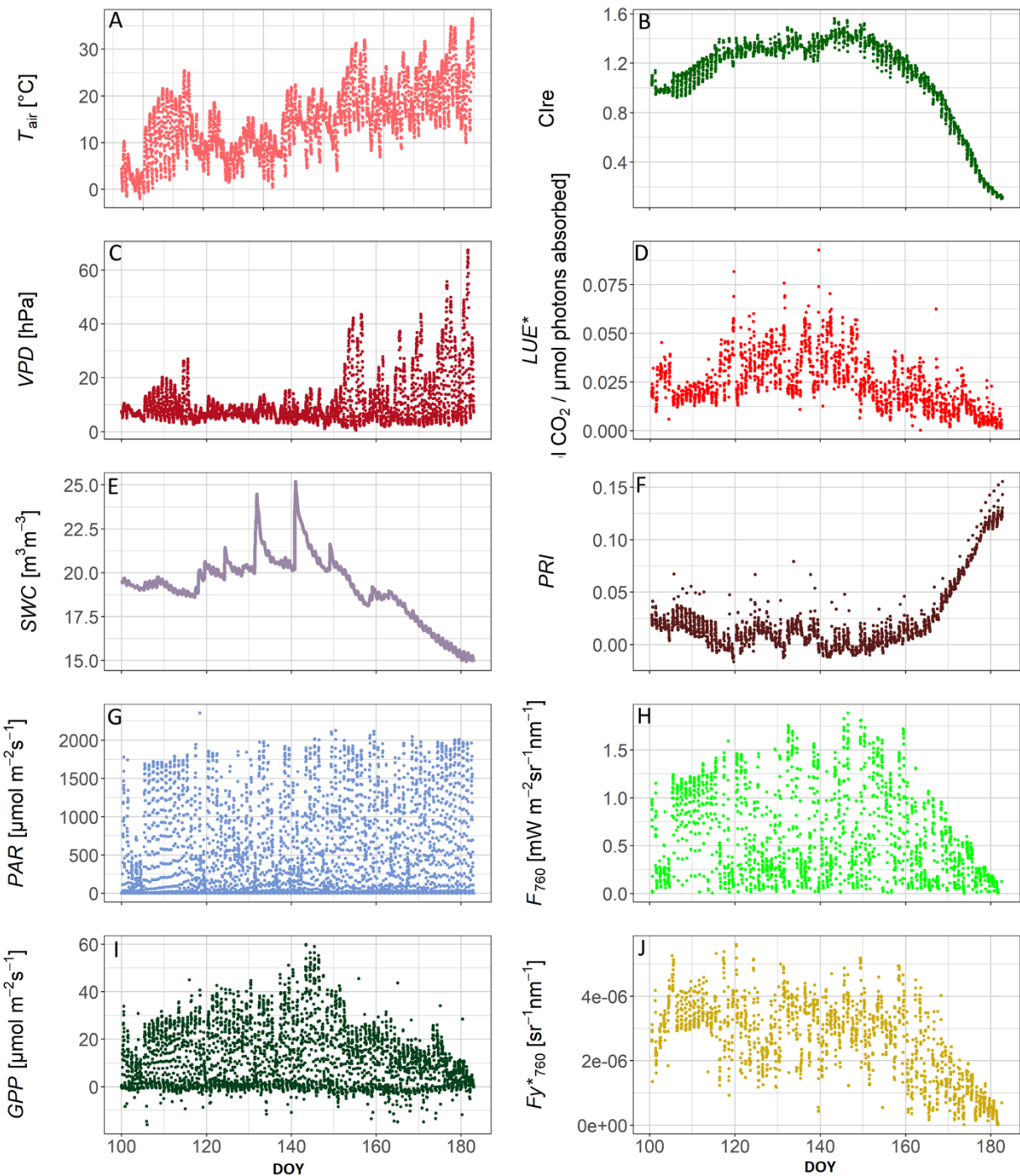


Figure 24. Time series of (A) air temperature (T_{air} [°C]), (C) vapour pressure deficit (VPD [hPa]), (E) soil water content (SWC [$\text{m}^3 \text{m}^{-3}$]), (G) photosynthetically active radiation (PAR [$\mu\text{mol m}^{-2} \text{s}^{-1}$]), (I) gross primary production (GPP [$\mu\text{mol m}^{-2} \text{s}^{-1}$]), (B) chlorophyll red-edge index (Clre), (D) light-use efficiency (LUE* [$\mu\text{mol CO}_2 / \mu\text{mol photons of PAR}$]), (F) Photochemical Reflectance Index (PRI), (H) far-red fluorescence (F_{760} [$\text{mW m}^{-2} \text{sr}^{-1} \text{nm}^{-1}$]), and (J) Fy^*_{760} [$\text{sr}^{-1} \text{nm}^{-1}$].

red fluorescence (F_{760} [$\text{mW m}^{-2} \text{sr}^{-1} \text{nm}^{-1}$]), (J) far-red apparent fluorescence yield (Fy^*_{760} [$\text{sr}^{-1} \text{nm}^{-1}$]) measured over winter wheat during a period from 10th of April until 30th of June 2019.

3.4.2.2. Extraction of seasonal dynamics from PRI , LUE^* , F_{760} and Fy^*_{760}

Slow varying components of PRI , LUE^* , F_{760} and Fy^*_{760} were extracted with SSA in [seasonal] frequency bin (Table 8). In order to evaluate whether slow varying SSA-components are related to structural and biochemical variability affecting PRI , LUE^* , F_{760} and Fy^*_{760} , we explored the relationship between these variables and $faPAR$ (Fig. 25). A strong linear correlation was observed between PRI^{ssa} and $faPAR$ ($R^2=0.96$) (Fig. 25A) and between Fy^{*ssa}_{760} and $faPAR$ ($R^2=0.88$) (Fig. 25C). Relationships between slow varying components of F_{760}^{ssa} and LUE^{*ssa} vs. $faPAR$ showed weaker linear correlation ($R^2=0.62$ and 0.54) (Fig. 25B, D) due to $faPAR$ saturation.

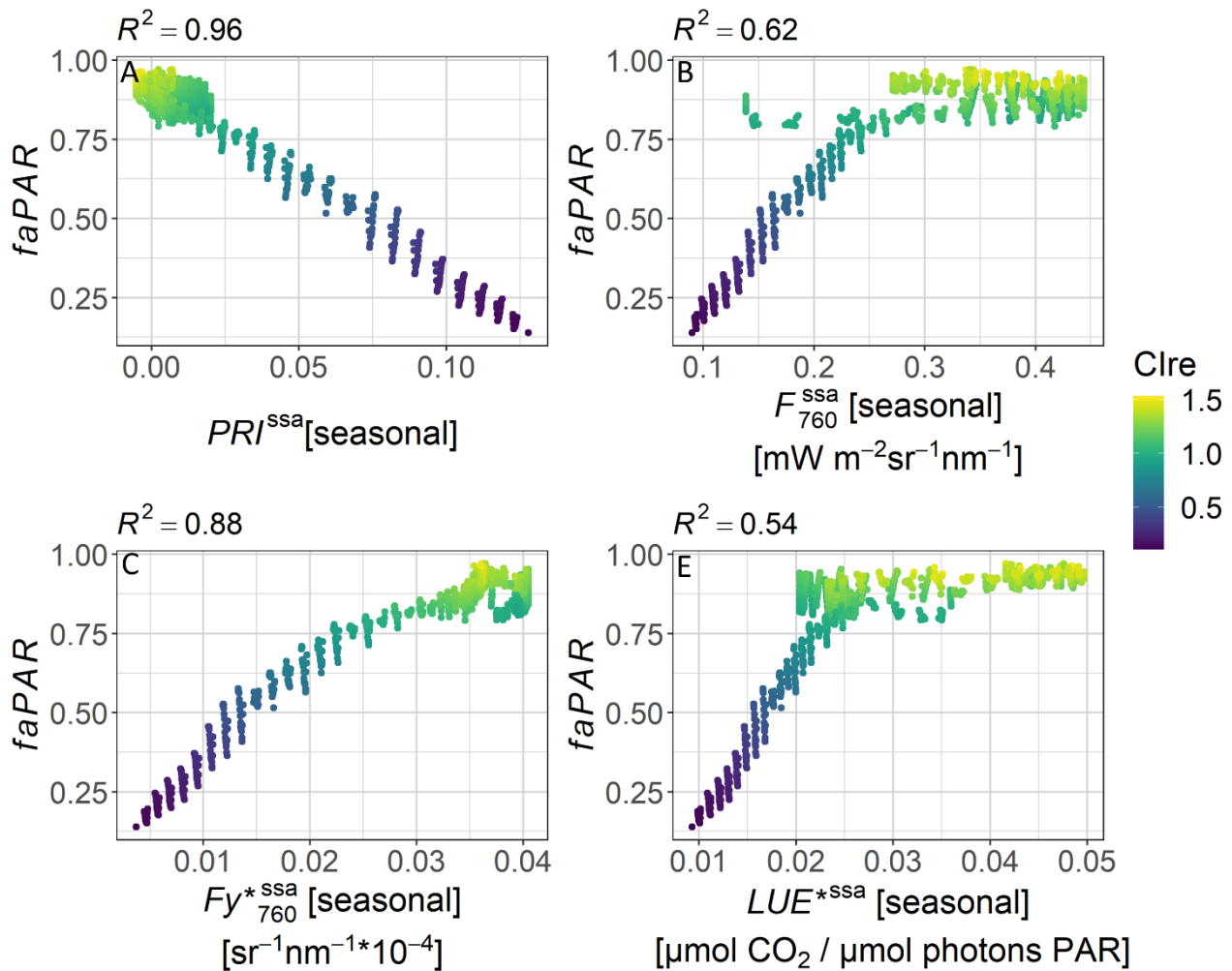


Figure 25. Linear relationships: (A) PRI^{ssa} [seasonal] vs $faPAR$, (B) F_{760}^{ssa} [seasonal] vs $faPAR$, (C) Fy^{*ssa}_{760} [seasonal] vs $faPAR$, (D) LUE^{*ssa} [seasonal] vs $faPAR$. Colour-coded with chlorophyll red-edge index ($Clre$).

3.4.2.3. Extraction of fast variability from PRI , LUE^* , F_{760} and Fy^*_{760}

Diurnal and sub-diurnal components of PRI , F_{760} , Fy^*_{760} and LUE^* , were summed up and considered together a fast component. In order to assess if the fast components PRI^{ssa} [diurnal+sub-diurnal],

F_{760}^{ssa} [diurnal+sub-diurnal] and $Fy^*_{760}^{ssa}$ [diurnal+sub-diurnal] are linked to physiological response of vegetation, we evaluated their relationships with LUE^{*ssa} [diurnal+sub-diurnal]. Similar to the results of the theoretical study, the relationship between PRI and LUE^* is stratified by structural/biochemical properties of the canopy as shown by colour-coding it with C/re (Fig. 26A). As was shown in the previous section, both PRI and LUE^* contained slow variability attributed to canopy structural/biochemical effects. In case of PRI , this is a pigments-related constitutive variability (Gamon & Berry, 2012), which obscures a functional link with LUE^* (Filella, Peñuelas, Llorens, & Estiarte, 2004; Hmimina et al., 2014). In case of LUE^* , computed as a ratio of GPP to PAR , it combines green canopy structure and light absorption and confounds it with physiology (Gitelson & Gamon, 2015). The negative relationship observed between PRI^{ssa} [diurnal+sub-diurnal] and LUE^{*ssa} [diurnal+sub-diurnal] is less scattered and shows a clear linear correlation (Fig. 26B). When the relationship is considered for moving window of 20 days (Fig. 26C), overall high $dCor$ (0.60-0.72) is observed at DOY 122-165 with lower values in the beginning and the end of time series (Fig. 26D). A decrease of $dCor$ around DOY 110-120 can be associated with an increase of T_{air} and VPD during these days (Fig. 24A, C), while an decrease after DOY 165 is most probably driven by degradation of chlorophyll at the end of the growing season (Fig. 24B).

The relationship between F_{760}^{ssa} [diurnal+sub-diurnal] and LUE_{par}^{ssa} [diurnal+sub-diurnal] significantly improved (Fig. 26E, $dCor = 0.66$) over the relationship between original variables (Fig. 26D, $dCor = 0.44$). The negative relationship observed here is similar to the result obtained in the theoretical study for $LAI > 1$ (Fig. 20A). Time series of $dCor$ between decomposed variables computed over the moving window of 20 days (Fig. 26F) follows the pattern of C/re (Fig. 24B), which also indicates the similarity to the model-based study, where $dCor$ between F_{760}^{ssa} [diurnal+sub-diurnal] and LUE follows LAI and C_{ab} seasonal cycles (Fig. 19F).

SSA-decomposition of Fy^*_{760} into [diurnal+sub-diurnal] component did not improve the relationship between LUE^* and Fy^*_{760} (Fig. 26G, H). However, for different T_{air} ranges (optimal T_{air} range of 10°-25° and sub-optimal T_{air} lower than 10° or higher than 25°), the relationships between $Fy^*_{760}^{ssa}$ [diurnal+sub-diurnal] and LUE^{*ssa} [diurnal+sub-diurnal] show clearer correlations with negative sign for optimal T_{air} range of 10°-25° (Fig. 27A) and positive sign for sub-optimal T_{air} lower than 10° or higher than 25° (Fig. 27B). Although the correlation coefficients are lower ($R = -0.28, 0.27$) in comparison to model-based relationships binned by NPQ classes (Fig. 20), these changes in the direction of the relationship might be also driven by alternating NPQ and PQ control due to different levels of stress (e.g. under low or high T_{air} photosynthesis is downregulated and NPQ increases resulting in positive relationship $Fy^*_{760}^{ssa}$ [diurnal+sub-diurnal] and LUE^{*ssa} [diurnal+sub-diurnal] analogously similar to the relationship between leaf-level parameters ϕ_p and ϕ'_f in the modelled time series (Fig. 21)).

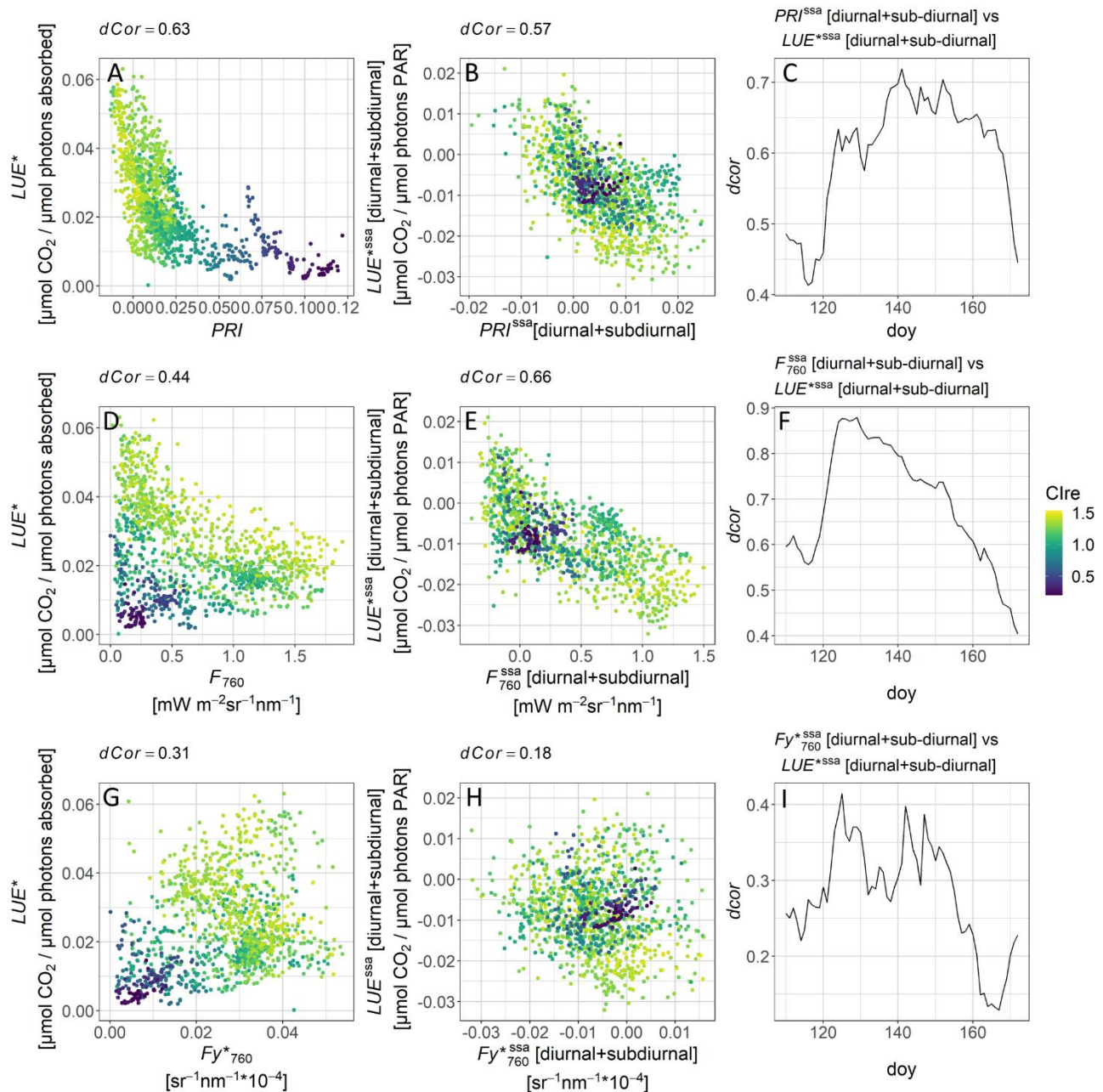


Figure 26. First row: relationships between PRI and LUE^* (A), PRI^{ssa} [diurnal+sub-diurnal] and LUE^{ssa} [diurnal+sub-diurnal] (B) and distance correlation ($dCor$) between the two computed using moving window of 20 days (C). Second row: relationships between F_{760} and LUE^* (D), F_{760}^{ssa} [diurnal+sub-diurnal] and LUE^{ssa} [diurnal+sub-diurnal] (E) and distance $dCor$ between the two computed using moving window of 20 days (F). Third row: relationships between Fy^{*760} and LUE^* (G), Fy^{*760}^{ssa} [diurnal+sub-diurnal] and LUE^{ssa} [diurnal+sub-diurnal] (H) and $dCor$ between the two computed using moving window of 20 days (I).

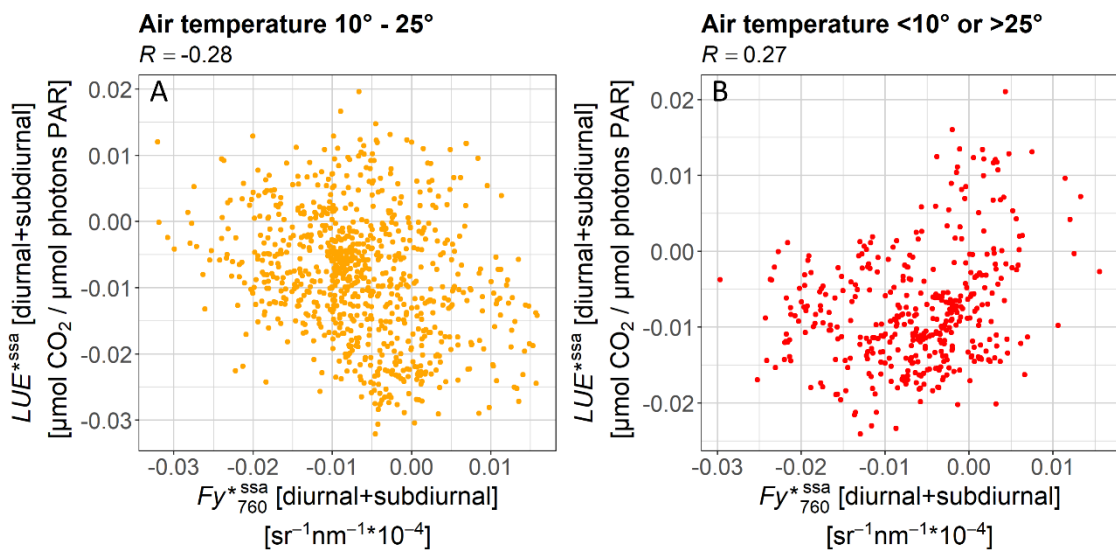


Figure 27. Relationship between Fy^{*ssa}_{760} [diurnal+sub-diurnal] and LUE^{*ssa} computed for T_{air} between 10° and 25° (A) and T_{air} lower than 10° or higher than 25° (B).

3.5. Conclusions

Automated proximal sensing is a powerful complement of ecosystem stations monitoring water and carbon fluxes. It provides spectral signals (F and PRI) encompassing information on light-use in the photosynthetic machinery and can, therefore, contribute to improve our understanding of ecosystem function variability in time. However, these signals are affected by confounding additional factors operating at different temporal scales. We demonstrated the capability of SSA to separate the components related to canopy structural/biochemical properties and physiology of these signals from a simulated realistic time series of spectral and physiological variables. This decomposition was especially successful in the case of PRI, whose relationship with light-use efficiency was still dependent on leaf area index. We also tested SSA approach on spectral and flux data collected during the whole growing season of winter wheat. The results showed that relationship between PRI and LUE (GPP/PAR) and F_{760} and LUE can be significantly improved if the slow variability associated with canopy structural/biochemical properties is removed from both variables. Moreover, in simulated and field datasets the direction of relationship between fast component of Fy^{*ssa}_{760} and LUE was shown to be controlled by competing photochemical and non-photochemical quenching processes determined by changing environmental conditions (i.e. T_{air} and VPD). We expect that the application of this method to automated continuous measurements will foster the exploitation of proximal sensing to monitoring and characterization of ecosystem functional properties.

4. Thesis Summary and Conclusions

The main aim of this research was to exploit the methods of proximal sensing of vegetation to elucidate a link between continuous hyperspectral measurements of optical indicators related to plant physiology and vegetation functioning. In particular, I focused on using multi-angular spectral measurements and high spectral and temporal resolution times series of solar-induced chlorophyll fluorescence (F) and photochemical reflectance index (PRI) to characterize the effects of anisotropy on these signals and to decouple slow and fast vegetation dynamics with Singular Spectrum Analysis technique.

4.1. Main results

4.1.1. Part 1.

Far-red fluorescence (F_{760}), red fluorescence (F_{687}) and PRI exhibit strong anisotropic response under varying solar-view geometry driven by the interactions between emitted/reflected light and canopy structure

The results of the Part 1, aimed at the investigation of the effects of varying solar-view geometry and canopy structure on F and PRI , showed that multi-angular measurements provide valuable information on spectro-directional response of vegetation targets. The findings of this study showed that the angular distribution of F , PRI and reflectance (R) is different for each canopy type in terms of observed patterns, the magnitude of the anisotropic response (anisotropy index, ANIX) and the sensitivity to geometric effects inside the canopy. The qualitative analysis of the differences between scaled F , PRI and the corresponding R measured in the nearby band revealed that their anisotropic response do not totally covary and that the angular configuration plays an important role. This suggests that while some studies have used reflectance-based metrics (or kernel-driven models parameterized with R observations) to correct directional F , these should be applied with caution since the nature of the two signals is very different (i.e. emission and reflection), and the directional confounding effects may intervene with physiological response of F and PRI . In the future studies, the characterization of the physiological status of leaves at different layers inside the canopy by means of, for example, FluoWat should be performed concurrently with multi-angular measurements to disentangle the contribution of physiology from directional effects. To minimize the complexity brought by off-nadir configurations of the set-ups for continuous measurements, a correction scheme for the signal directionality should be considered.

4.1.2. Part 2.

Singular Spectrum Analysis was successfully applied to decompose fast variability, attributed to physiological status, and slow variability, attributed to seasonally changing structural and biochemical vegetation properties in time series of far-red fluorescence (F_{760}) and PRI

This study (Part 2) aimed at disentangling time-scale dependent vegetation processes from time series of simulated and experimentally acquired time series of far-red fluorescence (F_{760}), fluorescence apparent yield (Fy^*) and PRI . The proof of concept tested on SOPCE-simulated time

series showed that the most effective was the deconvolution of constitutive (slow) and facultative components (fast) of *PRI* variability. The fast SSA-decomposed component of *PRI* varying in the frequency bin 30 min – 1 week showed a better relationship with non-photochemical quenching (*NPQ*) and photosynthetic light-use efficiency (*LUE*) in comparison to undecomposed *PRI*. The decomposition of F_{760} into slow (driven by $aPAR_{cab}$) and fast (driven by physiology) components was more effective during the growing period ($LAI > 1$), while the decomposed fast component of Fy^*_{760} was able to track changes in the reference fluorescence physiological variable ($\Delta F_{760}^{scope} / PAR$) for the whole time series. Interestingly, the direction of the relationship between fast Fy^*_{760} and light-use efficiency (*LUE*) was regulated by *NPQ* values – negative for $NPQ < 0.1$ and positive for *NPQ* range 0.1–2.5, suggesting the physiological meaning behind fast Fy^*_{760} . The application of the SSA on the field dataset collected in winter wheat field allowed to improve the correlation between fast components of F_{760} and *PRI* with apparent *LUE* (*GPP/PAR*) in comparison with original time series. Overall, the time series decomposition methods of spectral-domain can foster the use of continuous spectral measurements of high temporal resolution. The simultaneous installation of automated high spectral resolution devices with micro-PAM can provide the dataset of spectral and physiological variables for the validation of the decomposition.

4.2. Concluding remarks

Overall, the results of this thesis reinforce the importance of careful characterization of the factors, which confound the physiological meaning of solar-induced chlorophyll fluorescence (*F*) and photochemical reflectance index (*PRI*). Solar-view geometry is a major source of uncertainty, which has been shown to significantly alter the values of both *F* and *PRI* and complicate the interpretation of the relationships between these optical signal and estimations of gross primary production (*GPP*) and photosynthetic light-use efficiency (*LUE*). Multi-angular measurements of *F* and *PRI* can be used in conjunction with presented here SSA-based approach of decoupling slow and fast variability in time series of optical signals. Since SSA is not fully effective in distinguishing between directional effects imposed on diurnal cycles of *F* and *PRI* (as both directional effects and fast physiological responses can vary in the same frequency), the multi-angular measurements can provide valuable source of information to correct for anisotropy. However, the deployment of field goniometers is demanding and limited to relatively short canopies. Therefore, automatic tower-based scanning systems observing the canopy from different viewing angles can complement nadir-looking set-ups.

In the view of increasing amount of RS data available from a variety of platforms (UAV, airborne, satellite) capable of distinguishing small changes in vegetation spectrum associated with *F* and *NPQ*, a robust methodology for minimization of confounding effect should be developed. The results of this thesis represent a step forward in this direction.

5. Bibliography

- Aasen, H., Van Wittenberghe, S., Medina, N. S., Damm, A., Goulas, Y., Wieneke, S., ... Arthur, A. Mac. (2019). Sun-induced chlorophyll fluorescence II: Review of passive measurement setups, protocols, and their application at the leaf to canopy level. *Remote Sensing*, 11(8), 1–32. <https://doi.org/10.3390/rs11080956>
- Alonso, L., Gómez-Chova, L., Vila-Francés, J., Amorós-López, J., Guanter, L., Calpe, J., & Moreno, J. (2008). Improved fraunhofer line discrimination method for vegetation fluorescence quantification. *IEEE Geoscience and Remote Sensing Letters*, 5(4), 620–624. <https://doi.org/10.1109/LGRS.2008.2001180>
- Alonso, L., Van Wittenberghe, S., Amorós-López, J., Vila-Francés, J., Gómez-Chova, L., & Moreno, J. (2017). Diurnal cycle relationships between passive fluorescence, PRI and NPQ of vegetation in a controlled stress experiment. *Remote Sensing*, 9(8). <https://doi.org/10.3390/rs9080770>
- Anthoni, P. M., Knohl, A., Rebmann, C., Freibauer, A., Mund, M., Ziegler, W., ... Schulze, E. D. (2004). Forest and agricultural land-use-dependent CO₂ exchange in Thuringia, Germany. *Global Change Biology*, 10(12), 2005–2019. <https://doi.org/10.1111/j.1365-2486.2004.00863.x>
- Arneth, A., Harrison, S. P., Zaehle, S., Tsigaridis, K., Menon, S., Bartlein, P. J., ... Vesala, T. (2010). Terrestrial biogeochemical feedbacks in the climate system. *Nature Geoscience*, 3(8), 525–532. <https://doi.org/10.1038/ngeo905>
- Asner, G. P., Martin, R. E., Tupayachi, R., Emerson, R., Martinez, P., Sinca, F., ... Lugo, A. E. (2011). Taxonomy and remote sensing of leaf mass per area (LMA) in humid tropical forests. *Ecological Applications*, 21(1), 85–98. <https://doi.org/10.1890/09-1999.1>
- Atherton, J., Nichol, C. J., & Porcar-Castell, A. (2016). Using spectral chlorophyll fluorescence and the photochemical reflectance index to predict physiological dynamics. *Remote Sensing of Environment*, 176, 17–30. <https://doi.org/10.1016/j.rse.2015.12.036>
- Baker, N. R. (2008). Chlorophyll Fluorescence: A Probe of Photosynthesis In Vivo. *Annual Review of Plant Biology*, 59(1), 89–113. <https://doi.org/10.1146/annurev.arplant.59.032607.092759>
- Baldocchi, D., Valentini, R., Running, S., Oechel, W., & Dahlman, R. (1996). Strategies for measuring and modelling carbon dioxide and water vapour fluxes over terrestrial ecosystems. *Global Change Biology*, 2(3). <https://doi.org/10.1111/j.1365-2486.1996.tb00069.x>
- Balzarolo, M., Anderson, K., Nichol, C., Rossini, M., Vescovo, L., Arriga, N., ... Martín, M. P. (2011). Ground-Based Optical Measurements at European Flux Sites: A Review of Methods, Instruments and Current Controversies. *Sensors*, 11(8), 7954–7981. <https://doi.org/10.3390/s110807954>
- Barber, J., & Andersson, B. (1992). Too much of a good thing: light can be bad for photosynthesis. *Trends in Biochemical Sciences*, 17(2), 61–66. [https://doi.org/10.1016/0968-0004\(92\)90503-2](https://doi.org/10.1016/0968-0004(92)90503-2)
- Barton, C. V. M., & North, P. R. J. (2001). Remote sensing of canopy light use efficiency using the photochemical reflectance index model and sensitivity analysis. *Remote Sensing of Environment*, 78(3), 264–273. [https://doi.org/10.1016/S0034-4257\(01\)00224-3](https://doi.org/10.1016/S0034-4257(01)00224-3)
- Biriukova, K., Celesti, M., Evdokimov, A., Pacheco-Labrador, J., Julitta, T., Migliavacca, M., ... Rossini, M. (2020a). Effects of varying solar-view geometry and canopy structure on solar-induced

- chlorophyll fluorescence and PRI. *International Journal of Applied Earth Observation and Geoinformation*, 89(September 2019), 102069. <https://doi.org/10.1016/j.jag.2020.102069>
- Biriukova, K., Pacheco-Labrador, J., Migliavacca, M., Mahecha, M., Gonzalez-Cascon, R., Martin Isabel, M. P., & Rossini, M.. (2020b). *Time series of fluxes, biochemical and spectral variables simulated with SCOPE model for Singular Spectrum Analysis*. doi: 10.6084/m9.figshare.13190858
- Broomhead, D. S., & King, G. P. (1986). Extracting qualitative dynamics from experimental data. *Physica D: Nonlinear Phenomena*, 20(2–3), 217–236. [https://doi.org/10.1016/0167-2789\(86\)90031-X](https://doi.org/10.1016/0167-2789(86)90031-X)
- Buschmann, C. (2007). Variability and application of the chlorophyll fluorescence emission ratio red/far-red of leaves. *Photosynthesis Research*, 92(2), 261–271. <https://doi.org/10.1007/s11120-007-9187-8>
- Butler, W. L. (1978). Energy Distribution in the Photochemical Apparatus of Photosynthesis. *Annual Review of Plant Physiology*, 29(1), 345–378. <https://doi.org/10.1146/annurev.pp.29.060178.002021>
- Buttlar, J. V., Zscheischler, J., & Mahecha, M. D. (2014). An extended approach for spatiotemporal gapfilling: Dealing with large and systematic gaps in geoscientific datasets. *Nonlinear Processes in Geophysics*, 21(1), 203–215. <https://doi.org/10.5194/npg-21-203-2014>
- Buttlar, Jannis V. (2015). Package ‘spectral.methods,’ 29.
- Campbell, P. K. E., Huemmrich, K. F., Middleton, E. M., Ward, L. A., Julitta, T., Daughtry, C. S. T., ... Kustas, W. P. (2019). Diurnal and seasonal variations in chlorophyll fluorescence associated with photosynthesis at leaf and canopy scales. *Remote Sensing*, 11(5). <https://doi.org/10.3390/rs11050488>
- Celesti, M., van der Tol, C., Cogliati, S., Panigada, C., Yang, P., Pinto, F., ... Rossini, M. (2018). Exploring the physiological information of Sun-induced chlorophyll fluorescence through radiative transfer model inversion. *Remote Sensing of Environment*, 215(June), 97–108. <https://doi.org/10.1016/j.rse.2018.05.013>
- Cendrero-Mateo, M. P., Wieneke, S., Damm, A., Alonso, L., Pinto, F., Moreno, J., ... Arthur, A. Mac. (2019). Sun-induced chlorophyll fluorescence III: Benchmarking retrieval methods and sensor characteristics for proximal sensing. *Remote Sensing*, 11(8), 962. <https://doi.org/10.3390/rs11080921>
- Cheng, Y. Ben, Middleton, E. M., Huemmrich, K. F., Zhang, Q., Campbell, P. K. E., Corp, L. A., ... Kustas, W. P. (2010). Utilizing in situ directional hyperspectral measurements to validate bio-indicator simulations for a corn crop canopy. *Ecological Informatics*, 5(5), 330–338. <https://doi.org/10.1016/j.ecoinf.2010.03.001>
- Cheng, Y. Ben, Middleton, E. M., Zhang, Q., Corp, L. A., Dandois, J., & Kustas, W. P. (2012). The photochemical reflectance index from directional cornfield reflectances: Observations and simulations. *Remote Sensing of Environment*, 124, 444–453. <https://doi.org/10.1016/j.rse.2012.05.030>
- Cogliati, S., Rossini, M., Julitta, T., Meroni, M., Schickling, A., Burkart, A., ... Colombo, R. (2015a). Continuous and long-term measurements of reflectance and sun-induced chlorophyll fluorescence

- by using novel automated field spectroscopy systems. *Remote Sensing of Environment*, 164, 270–281. <https://doi.org/10.1016/j.rse.2015.03.027>
- Cogliati, S., Verhoef, W., Kraft, S., Sabater, N., Alonso, L., Vicent, J., ... Colombo, R. (2015b). Retrieval of sun-induced fluorescence using advanced spectral fitting methods. *Remote Sensing of Environment*, 169, 344–357. <https://doi.org/10.1016/j.rse.2015.08.022>
- Cogliati, S., Celesti, M., Cesana, I., Miglietta, F., Genesio, L., Julitta, T., ... Colombo, R. (2019). A spectral fitting algorithm to retrieve the fluorescence spectrum from canopy radiance. *Remote Sensing*, 11(16). <https://doi.org/10.3390/rs11161840>
- Collatz, G. J., Ball, J. T., Grivet, C., & Berry, J. A. (1991). Physiological and environmental regulation of stomatal conductance, photosynthesis and transpiration: a model that includes a laminar boundary layer. *Agricultural and Forest Meteorology*, 54(2–4), 107–136. [https://doi.org/10.1016/0168-1923\(91\)90002-8](https://doi.org/10.1016/0168-1923(91)90002-8)
- Colombo, R., Meroni, M., Marchesi, A., Busetto, L., Rossini, M., Giardino, C., & Panigada, C. (2008). Estimation of leaf and canopy water content in poplar plantations by means of hyperspectral indices and inverse modeling. *Remote Sensing of Environment*, 112(4), 1820–1834. <https://doi.org/10.1016/j.rse.2007.09.005>
- Colombo, R., Celesti, M., Bianchi, R., Campbell, P. K. E., Cogliati, S., Cook, B. D., ... Schickling, A. (2018). Variability of sun-induced chlorophyll fluorescence according to stand age-related processes in a managed loblolly pine forest. *Global Change Biology*, 24(7), 2980–2996. <https://doi.org/10.1111/gcb.14097>
- Coops, N. C., Hilker, T., Hall, F. G., Nichol, C. J., & Drolet, G. G. (2010). Estimation of Light-use Efficiency of Terrestrial Ecosystems from Space: A Status Report. *BioScience*, 60(10), 788–797. <https://doi.org/10.1525/bio.2010.60.10.5>
- Corp, L. A., Cook, B. D., Middleton, E. M., Cheng, Y. Ben, Huemmrich, K. F., & Campbell, P. K. E. (2010). Fusion: A fully ultraportable system for imaging objects in nature. *International Geoscience and Remote Sensing Symposium (IGARSS)*, 1671–1674. <https://doi.org/10.1109/IGARSS.2010.5652788>
- Damm, A., Guanter, L., Verhoef, W., Schläpfer, D., Garbari, S., & Schaepman, M. E. (2015). Impact of varying irradiance on vegetation indices and chlorophyll fluorescence derived from spectroscopy data. *Remote Sensing of Environment*, 156, 202–215. <https://doi.org/10.1016/j.rse.2014.09.031>
- Daumard, F., Champagne, S., Fournier, A., Goulas, Y., Ounis, A., Hanocq, J. F., & Moya, I. (2010). A field platform for continuous measurement of canopy fluorescence. *IEEE Transactions on Geoscience and Remote Sensing*, 48(9), 3358–3368. <https://doi.org/10.1109/TGRS.2010.2046420>
- De Wit, C. T. (1965). Photosynthesis of leaf canopies. *Agricultural Research Reports*, (663), 1–54. <https://doi.org/10.2172/4289474>
- Demmig-Adams, B., & Adams, W. W. (1992). Photoprotection and other responses of plants to high light stress. *Annual Review of Plant Physiology and Plant Molecular Biology*, 43(1), 599–626. <https://doi.org/10.1146/annurev.pp.43.060192.003123>
- Demmig-Adams, B. (1990). Carotenoids and photoprotection in plants: A role for the xanthophyll zeaxanthin. *BBA - Bioenergetics*. [https://doi.org/10.1016/0005-2728\(90\)90088-L](https://doi.org/10.1016/0005-2728(90)90088-L)

- Drolet, G. G., Huemmrich, K. F., Hall, F. G., Middleton, E. M., Black, T. A., Barr, A. G., & Margolis, H. A. (2005). A MODIS-derived photochemical reflectance index to detect inter-annual variations in the photosynthetic light-use efficiency of a boreal deciduous forest. *Remote Sensing of Environment*, 98(2–3), 212–224. <https://doi.org/10.1016/j.rse.2005.07.006>
- Drusch, M., Moreno, J., Del Bello, U., Franco, R., Goulas, Y., Huth, A., ... Verhoef, W. (2017). The FLuorescence EXplorer Mission Concept-ESA's Earth Explorer 8. *IEEE Transactions on Geoscience and Remote Sensing*, 55(3), 1273–1284. <https://doi.org/10.1109/TGRS.2016.2621820>
- El-Madany, T. S., Reichstein, M., Perez-Priego, O., Carrara, A., Moreno, G., Pilar Martín, M., ... Migliavacca, M. (2018). Drivers of spatio-temporal variability of carbon dioxide and energy fluxes in a Mediterranean savanna ecosystem. *Agricultural and Forest Meteorology*, 262(July 2017), 258–278. <https://doi.org/10.1016/j.agrformet.2018.07.010>
- Filella, I., Porcar-Castell, A., Munné-Bosch, S., Bäck, J., Garbulsky, M. F., & Peñuelas, J. (2009). PRI assessment of long-term changes in carotenoids/chlorophyll ratio and short-term changes in de-epoxidation state of the xanthophyll cycle. *International Journal of Remote Sensing*, 30(17), 4443–4455. <https://doi.org/10.1080/01431160802575661>
- Filella, I., Amaro, T., Araus, J. L., & Peñuelas, J. (1996). Relationship between photosynthetic radiation-use efficiency of barley canopies and the photochemical reflectance index (PRI). *Physiologia Plantarum*, 96(2), 211–216. <https://doi.org/10.1111/j.1399-3054.1996.tb00204.x>
- Filella, I., Peñuelas, J., Llorens, L., & Estiarte, M. (2004). Reflectance assessment of seasonal and annual changes in biomass and CO₂ uptake of a Mediterranean shrubland submitted to experimental warming and drought. *Remote Sensing of Environment*, 90(3), 308–318. <https://doi.org/10.1016/j.rse.2004.01.010>
- Fournier, A., Daumard, F., Champagne, S., Ounis, A., Goulas, Y., & Moya, I. (2012). Effect of canopy structure on sun-induced chlorophyll fluorescence. *ISPRS Journal of Photogrammetry and Remote Sensing*, 68(1), 112–120. <https://doi.org/10.1016/j.isprsjprs.2012.01.003>
- Fraedrich, K. (1986). Estimating the Dimensions of Weather and Climate Attractors. *Journal of the Atmospheric Sciences*. [https://doi.org/10.1175/1520-0469\(1986\)043<0419:etdowa>2.0.co;2](https://doi.org/10.1175/1520-0469(1986)043<0419:etdowa>2.0.co;2)
- Frankenberg, C., & Berry, J. (2018). *Solar Induced Chlorophyll Fluorescence: Origins, Relation to Photosynthesis and Retrieval. Comprehensive Remote Sensing*. Elsevier. <https://doi.org/10.1016/b978-0-12-409548-9.10632-3>
- Gamon, J. A. (2015). Reviews and Syntheses: Optical sampling of the flux tower footprint. *Biogeosciences*, 12(14), 4509–4523. <https://doi.org/10.5194/bg-12-4509-2015>
- Gamon, J. A., Peñuelas, J., & Field, C. B. (1992). A narrow-waveband spectral index that tracks diurnal changes in photosynthetic efficiency. *Remote Sensing of Environment*, 41(1), 35–44. [https://doi.org/10.1016/0034-4257\(92\)90059-S](https://doi.org/10.1016/0034-4257(92)90059-S)
- Gamon, J. A., Rahman, A. F., Dungan, J. L., Schildhauer, M., & Huemmrich, K. F. (2006). Spectral Network (SpecNet)-What is it and why do we need it? *Remote Sensing of Environment*, 103(3), 227–235. <https://doi.org/10.1016/j.rse.2006.04.003>

- Gamon, J. A., & Berry, J. A. (2012). Facultative and constitutive pigment effects on the Photochemical Reflectance Index (PRI) in sun and shade conifer needles. *Israel Journal of Plant Sciences*, 60(1–2), 85–95. <https://doi.org/10.1560/IJPS.60.1-2.85>
- Garbulsky, M. F., Peñuelas, J., Gamon, J., Inoue, Y., & Filella, I. (2011). The photochemical reflectance index (PRI) and the remote sensing of leaf, canopy and ecosystem radiation use efficiencies. A review and meta-analysis. *Remote Sensing of Environment*, 115(2), 281–297. <https://doi.org/10.1016/j.rse.2010.08.023>
- Garbulsky, M. F., Peñuelas, J., Ogaya, R., & Filella, I. (2013). Leaf and stand-level carbon uptake of a Mediterranean forest estimated using the satellite-derived reflectance indices EVI and PRI. *International Journal of Remote Sensing*, 34(4), 1282–1296. <https://doi.org/10.1080/01431161.2012.718457>
- Garzonio, R., di Mauro, B., Colombo, R., & Cogliati, S. (2017). Surface reflectance and sun-induced fluorescence spectroscopy measurements using a small hyperspectral UAS. *Remote Sensing*, 9(5), 472. <https://doi.org/10.3390/rs9050472>
- Genty, B., Briantais, J. M., & Baker, N. R. (1989). The relationship between the quantum yield of photosynthetic electron transport and quenching of chlorophyll fluorescence. *Biochimica et Biophysica Acta - General Subjects*, 990(1). [https://doi.org/10.1016/S0304-4165\(89\)80016-9](https://doi.org/10.1016/S0304-4165(89)80016-9)
- Ghil, M., Allen, M. R., Dettinger, M. D., Ide, K., Kondrashov, D., Mann, M. E., ... Yiou, P. (2002). Advanced spectral methods for climatic time series. *Reviews of Geophysics*, 40(1). <https://doi.org/10.1029/2000RG000092>
- Giardino, C., & Brivio, P. A. (2003). The application of a dedicated device to acquire bidirectional reflectance factors over natural surfaces. *International Journal of Remote Sensing*, 24(14), 2989–2995. <https://doi.org/10.1080/0143116031000094782>
- Gitelson, A. A., Buschmann, C., & Lichtenthaler, H. K. (1999). The chlorophyll fluorescence ratio F735F700 as an accurate measure of the chlorophyll content in plants. *Remote Sensing of Environment*, 69(3), 296–302. [https://doi.org/10.1016/S0034-4257\(99\)00023-1](https://doi.org/10.1016/S0034-4257(99)00023-1)
- Gitelson, A. A., & Gamon, J. A. (2015). The need for a common basis for defining light-use efficiency: Implications for productivity estimation. *Remote Sensing of Environment*, 156, 196–201. <https://doi.org/10.1016/j.rse.2014.09.017>
- Gitelson, A. A., Gritz, Y., & Merzlyak, M. N. (2003). Relationships between leaf chlorophyll content and spectral reflectance and algorithms for non-destructive chlorophyll assessment in higher plant leaves. *Journal of Plant Physiology*, 160(3), 271–282. <https://doi.org/10.1078/0176-1617-00887>
- Golyandina, N., & Osipov, E. (2007). The “Caterpillar”-SSA method for analysis of time series with missing values. *Journal of Statistical Planning and Inference*, 137(8), 2642–2653. <https://doi.org/10.1016/j.jspi.2006.05.014>
- Golyandina, N. & Korobeynikov, A. (2014). Basic Singular Spectrum Analysis and forecasting with R. *Computational Statistics and Data Analysis*, 71, 934–954. <https://doi.org/10.1016/j.csda.2013.04.009>

- Golyandina, N., Korobeynikov, A., & Zhigljavsky, A. (2018). *Singular Spectrum Analysis with R. Singular Spectrum Analysis*. Berlin, Heidelberg: Springer Berlin Heidelberg. <https://doi.org/10.1007/978-3-662-57380-8>
- Golyandina, N., Nekrutkin, V., & Zhigljavsky, A. (2001). Analysis of Time Series Structure: SSA and Related Techniques. *CHAPMAN & HALL/CRC*, 97(460), 1207–1208. <https://doi.org/10.1198/jasa.2002.s239>
- Golyandina, N., & Zhigljavsky, A. (2013). *Singular Spectrum Analysis for Time Series*. <https://doi.org/10.1007/978-3-642-34913-3>
- Gonzalez-Cascón, R., Martín, M.P., 2018. Protocol for Pigment Content Quantification in Herbaceous Covers: Sampling and Analysis. *protocols.io*. dx.doi.org/10.17504/ protocols.io.qs6dwhe.
- Grace, J., Nichol, C., Disney, M., Lewis, P., Quaife, T., & Bowyer, P. (2007). Can we measure terrestrial photosynthesis from space directly, using spectral reflectance and fluorescence? *Global Change Biology*, 13(7), 1484–1497. <https://doi.org/10.1111/j.1365-2486.2007.01352.x>
- Guan, K., Berry, J. A., Zhang, Y., Joiner, J., Guanter, L., Badgley, G., & Lobell, D. B. (2016). Improving the monitoring of crop productivity using spaceborne solar-induced fluorescence. *Global Change Biology*, 22(2), 716–726. <https://doi.org/10.1111/gcb.13136>
- Guanter, L., Zhang, Y., Jung, M., Joiner, J., Voigt, M., Berry, J. A., ... Griffis, T. J. (2014). Global and time-resolved monitoring of crop photosynthesis with chlorophyll fluorescence. *Proceedings of the National Academy of Sciences of the United States of America*, 111(14), E1327–E1333. <https://doi.org/10.1073/pnas.1320008111>
- Hall, F. G., Hilker, T., & Coops, N. C. (2011). PHOTOSYNTHESIS, photosynthesis from space: Theoretical foundations of a satellite concept and validation from tower and spaceborne data. *Remote Sensing of Environment*, 115(8), 1918–1925. <https://doi.org/10.1016/j.rse.2011.03.014>
- Hall, F. G., Hilker, T., Coops, N. C., Lyapustin, A., Huemmrich, K. F., Middleton, E., ... Black, T. A. (2008). Multi-angle remote sensing of forest light use efficiency by observing PRI variation with canopy shadow fraction. *Remote Sensing of Environment*, 112(7), 3201–3211. <https://doi.org/10.1016/j.rse.2008.03.015>
- He, L., Magney, T., Dutta, D., Yin, Y., Köhler, P., Grossmann, K., ... Frankenberg, C. (2020). From the Ground to Space: Using Solar-Induced Chlorophyll Fluorescence to Estimate Crop Productivity. *Geophysical Research Letters*, 47(7), 1–12. <https://doi.org/10.1029/2020GL087474>
- Heimann, M., & Reichstein, M. (2008). Terrestrial ecosystem carbon dynamics and climate feedbacks. *Nature*, 451(7176), 289–292. <https://doi.org/10.1038/nature06591>
- Hilker, T., Coops, N. C., Hall, F. G., Black, T. A., Wulder, M. A., Nesic, Z., & Krishnan, P. (2008). Separating physiologically and directionally induced changes in PRI using BRDF models. *Remote Sensing of Environment*, 112(6), 2777–2788. <https://doi.org/10.1016/j.rse.2008.01.011>
- Hilker, T., Gitelson, A., Coops, N. C., Hall, F. G., & Black, T. A. (2011). Tracking plant physiological properties from multi-angular tower-based remote sensing. *Oecologia*, 165(4), 865–876. <https://doi.org/10.1007/s00442-010-1901-0>

- Hilker, T., Nesic, Z., Coops, N. C., & Lessard, D. (2010a). A new, automated, multiangular radiometer instrument for tower-based observations of canopy reflectance (AMSPEC II). *Instrumentation Science and Technology*, 38(5), 319–340. <https://doi.org/10.1080/10739149.2010.508357>
- Hilker, T., Hall, F. G., Coops, N. C., Lyapustin, A., Wang, Y., Nesic, Z., ... Chasmer, L. (2010b). Remote sensing of photosynthetic light-use efficiency across two forested biomes: Spatial scaling. *Remote Sensing of Environment*, 114(12), 2863–2874. <https://doi.org/10.1016/j.rse.2010.07.004>
- Hmimina, G., Dufrêne, E., & Soudani, K. (2014). Relationship between photochemical reflectance index and leaf ecophysiological and biochemical parameters under two different water statuses: Towards a rapid and efficient correction method using real-time measurements. *Plant, Cell and Environment*, 37(2), 473–487. <https://doi.org/10.1111/pce.12171>
- Hmimina, G., Merlier, E., Dufrêne, E., & Soudani, K. (2015). Deconvolution of pigment and physiologically related photochemical reflectance index variability at the canopy scale over an entire growing season. *Plant, Cell and Environment*, 38(8), 1578–1590. <https://doi.org/10.1111/pce.12509>
- Homolová, L., Malenovský, Z., Clevers, J. G. P. W., García-Santos, G., & Schaepman, M. E. (2013). Review of optical-based remote sensing for plant trait mapping. *Ecological Complexity*, 15, 1–16. <https://doi.org/10.1016/j.ecocom.2013.06.003>
- Huang, N. E., Shen, Z., Long, S. R., Wu, M. C., Shih, H. H., Yen, N., ... Liu, H. H. (1996). The empirical mode decomposition and the Hilbert spectrum for nonlinear and non-stationary time series analysis. *Proceedings of the Royal Society A*, 454(1971).
- Inoue, Y., Peñuelas, J., Miyata, A., & Mano, M. (2008). Normalized difference spectral indices for estimating photosynthetic efficiency and capacity at a canopy scale derived from hyperspectral and CO₂ flux measurements in rice. *Remote Sensing of Environment*, 112(1), 156–172. <https://doi.org/10.1016/j.rse.2007.04.011>
- Jenkins, J. P., Richardson, A. D., Braswell, B. H., Ollinger, S. V., Hollinger, D. Y., & Smith, M. L. (2007). Refining light-use efficiency calculations for a deciduous forest canopy using simultaneous tower-based carbon flux and radiometric measurements. *Agricultural and Forest Meteorology*, 143(1–2), 64–79. <https://doi.org/10.1016/j.agrformet.2006.11.008>
- Julitta, T., Burkart, A., Colombo, R., Rossini, M., Schickling, A., Migliavacca, M., Cogliati, S., Wutzler, T., Rascher, U., 2017. Accurate measurements of fluorescence in the O2A 855 and O2B band using the FloX spectroscopy system – results and prospects. In:Potsdam 856 GHG Workshop. From Photosystems to Ecosystems. 24-26 October 2017, Postdam, 857. Germany.
- Jupp, D. L. B., & Strahler, A. H. (1991). A hotspot model for leaf canopies. *Remote Sensing of Environment*, 38(3), 193–210. [https://doi.org/10.1016/0034-4257\(91\)90089-O](https://doi.org/10.1016/0034-4257(91)90089-O)
- Kergoat, L., Lafont, S., Arneth, A., Le Dantec, V., & Saugier, B. (2008). Nitrogen controls plant canopy light-use efficiency in temperate and boreal ecosystems. *Journal of Geophysical Research: Biogeosciences*, 113(4). <https://doi.org/10.1029/2007JG000676>
- Kim, J., Ryu, Y., Jiang, C., & Hwang, Y. (2019). Continuous observation of vegetation canopy dynamics using an integrated low-cost, near-surface remote sensing system. *Agricultural and Forest Meteorology*, 264(March 2018), 164–177. <https://doi.org/10.1016/j.agrformet.2018.09.014>

- Kljun, N., Calanca, P., Rotach, M. W., & Schmid, H. P. (2015). A simple two-dimensional parameterisation for Flux Footprint Prediction (FFP). *Geoscientific Model Development*, 8(11), 3695–3713. <https://doi.org/10.5194/gmd-8-3695-2015>
- Knauer, J., Zaehle, S., Medlyn, B. E., Reichstein, M., Williams, C. A., Migliavacca, M., ... Linderson, M. L. (2018). Towards physiologically meaningful water-use efficiency estimates from eddy covariance data. *Global Change Biology*, 24(2), 694–710. <https://doi.org/10.1111/gcb.13893>
- Knyazikhin, Y., Schull, M. A., Stenberg, P., Möttus, M., Rautiainen, M., Yang, Y., ... Myneni, R. B. (2013). Hyperspectral remote sensing of foliar nitrogen content. *Proceedings of the National Academy of Sciences of the United States of America*, 110(3), 1–8. <https://doi.org/10.1073/pnas.1210196109>
- Köhler, P., Guanter, L., Kobayashi, H., Walther, S., & Yang, W. (2018). Assessing the potential of sun-induced fluorescence and the canopy scattering coefficient to track large-scale vegetation dynamics in Amazon forests. *Remote Sensing of Environment*, 204(April 2016), 769–785. <https://doi.org/10.1016/j.rse.2017.09.025>
- Korobeynikov, A. A., Shlemov, A., Usevich, K., Golyandina, N., & Korobeynikov, M. A. (2017). *Title A Collection of Methods for Singular Spectrum Analysis*. Retrieved from <http://github.com/asl/rss>
- Krause, G. H., & Weis, E. (1991). Chlorophyll fluorescence and photosynthesis: The basics. *Annual Review of Plant Physiology and Plant Molecular Biology*, 42(1), 313–349. <https://doi.org/10.1146/annurev.pp.42.060191.001525>
- Kutsch, W. L., Brümmer, C., Don, C., Dechow, R., & Fuß, R. (2013). The full GHG balance over two crop rotations at an agricultural site near, 15, 12481.
- Lavorel, S., & Garnier, E. (2002). Predicting changes in community composition and ecosystem functioning from plant traits: Revisiting the Holy Grail. *Functional Ecology*, 16(5), 545–556. <https://doi.org/10.1046/j.1365-2435.2002.00664.x>
- Lee, J. E., Frankenberg, C., Van Der Tol, C., Berry, J. A., Guanter, L., Boyce, C. K., ... Saatchi, S. (2013). Forest productivity and water stress in Amazonia: Observations from GOSAT chlorophyll fluorescence. *Tohoku Journal of Experimental Medicine*, 230(1). <https://doi.org/10.1098/rspb.2013.0171>
- Leuning, R., Hughes, D., Daniel, P., Coops, N. C., & Newnham, G. (2006). A multi-angle spectrometer for automatic measurement of plant canopy reflectance spectra. *Remote Sensing of Environment*, 103(3), 236–245. <https://doi.org/10.1016/j.rse.2005.06.016>
- Li, Z., & Moreau, L. (1996). A new approach for remote sensing of canopy-absorbed photosynthetically active radiation. I: Total surface absorption. *Remote Sensing of Environment*, 55(3), 175–191. [https://doi.org/10.1016/S0034-4257\(95\)00097-6](https://doi.org/10.1016/S0034-4257(95)00097-6)
- Lichtenthaler, Hartmut K., Buschmann, Claus, 2001. Chlorophylls and carotenoids: measurement and characterization by UV-vis spectroscopy. *Curr. Protoc. Food Anal. Chem.* F4.3.1-F4 (Suppl. 1), 1–8.
- Liu, L., Liu, X., Wang, Z., & Zhang, B. (2016). Measurement and Analysis of Bidirectional SIF Emissions in Wheat Canopies. *IEEE Transactions on Geoscience and Remote Sensing*, 54(5), 2640–2651. <https://doi.org/10.1109/TGRS.2015.2504089>

- Luo, Y., El-Madany, T. S., Filippa, G., Ma, X., Ahrens, B., Carrara, A., ... Migliavacca, M. (2018). Using near-infrared-enabled digital repeat photography to track structural and physiological phenology in Mediterranean tree-grass ecosystems. *Remote Sensing*, 10(8). <https://doi.org/10.3390/rs10081293>
- Luo, Y., El-Madany, T., Ma, X., Nair, R., Jung, M., Weber, U., ... Migliavacca, M. (2020). Nutrients and water availability constrain the seasonality of vegetation activity in a Mediterranean ecosystem. *Global Change Biology*, (April), 1–22. <https://doi.org/10.1111/gcb.15138>
- Luus, K. A., Commane, R., Parazoo, N. C., Benmergui, J., Euskirchen, E. S., Frankenberg, C., ... Lin, J. C. (2017). Tundra photosynthesis captured by satellite-observed solar-induced chlorophyll fluorescence. *Geophysical Research Letters*, 44(3), 1564–1573. <https://doi.org/10.1002/2016GL070842>
- Magney, T. S., Frankenberg, C., Fisher, J. B., Sun, Y., North, G. B., Davis, T. S., ... Siebke, K. (2017). Connecting active to passive fluorescence with photosynthesis: a method for evaluating remote sensing measurements of Chl fluorescence. *New Phytologist*, 215(4), 1594–1608. <https://doi.org/10.1111/nph.14662>
- Mahecha, M. D., Reichstein, M., Jung, M., Seneviratne, S. I., Zaehle, S., Beer, C., ... Moors, E. (2010). Comparing observations and process-based simulations of biosphere-atmosphere exchanges on multiple timescales. *Journal of Geophysical Research: Biogeosciences*, 115(2), 1–21. <https://doi.org/10.1029/2009JG001016>
- Mahecha, M. D., Reichstein, M., Lange, H., Carvalhais, N., Bernhofer, C., Grünwald, T., ... Seufert, G. (2007). Characterizing ecosystem-atmosphere interactions from short to interannual time scales. *Biogeosciences*, 4(5), 743–758. <https://doi.org/10.5194/bg-4-743-2007>
- Mahecha, M. D., Reichstein, M., Carvalhais, N., Lasslop, G., Lange, H., Seneviratne, S. I., ... Richardson, A. D. (2010). Global convergence in the temperature sensitivity of respiration at ecosystem level. *Science*, 329(5993), 838–840. <https://doi.org/10.1126/science.1189587>
- Martín, M. P., Pacheco-Labrador, J., González-Cascón, R., Moreno, G., Migliavacca, M., García, M., ... Riaño, D. (2020). Estimation of essential vegetation variables in a dehesa ecosystem using reflectance factors simulated at different phenological stages. *Revista de Teledetección*, (55), 31. <https://doi.org/10.4995/raet.2020.13394>
- Martini, D., Pacheco-Labrador, J., Perez-Priego, O., van der Tol, C., El-Madany, T. S., Julitta, T., ... Migliavacca, M. (2019). Nitrogen and phosphorus effect on sun-induced fluorescence and gross primary productivity in mediterranean grassland. *Remote Sensing*, 11(21). <https://doi.org/10.3390/rs11212562>
- Melendo-Vega, J. R., Martín, M. P., Pacheco-Labrador, J., González-Cascón, R., Moreno, G., Pérez, F., ... Riaño, D. (2018). Improving the performance of 3-D radiative transfer model FLIGHT to simulate optical properties of a tree-grass ecosystem. *Remote Sensing*, 10(12). <https://doi.org/10.3390/rs10122061>
- Merlier, E., Hmimina, G., Dufrêne, E., & Soudani, K. (2015). Explaining the variability of the photochemical reflectance index (PRI) at the canopy-scale: Disentangling the effects of phenological and physiological changes. *Journal of Photochemistry and Photobiology B: Biology*, 151, 161–171. <https://doi.org/10.1016/j.jphotobiol.2015.08.006>

- Meroni, M., Busetto, L., Colombo, R., Guanter, L., Moreno, J., & Verhoef, W. (2010). Performance of Spectral Fitting Methods for vegetation fluorescence quantification. *Remote Sensing of Environment*, 114(2), 363–374. <https://doi.org/10.1016/j.rse.2009.09.010>
- Meroni, M., & Colombo, R. (2006). Leaf level detection of solar induced chlorophyll fluorescence by means of a subnanometer resolution spectroradiometer. *Remote Sensing of Environment*, 103(4), 438–448. <https://doi.org/10.1016/j.rse.2006.03.016>
- Meroni, M., Rossini, M., Guanter, L., Alonso, L., Rascher, U., Colombo, R., & Moreno, J. (2009). Remote sensing of solar-induced chlorophyll fluorescence: Review of methods and applications. *Remote Sensing of Environment*. <https://doi.org/10.1016/j.rse.2009.05.003>
- Middleton, E. M., Huemmrich, K. F., Landis, D. R., Black, T. A., Barr, A. G., & McCaughey, J. H. (2016). Photosynthetic efficiency of northern forest ecosystems using a MODIS-derived Photochemical Reflectance Index (PRI). *Remote Sensing of Environment*, 187, 345–366. <https://doi.org/10.1016/j.rse.2016.10.021>
- Middleton, E. M., Cheng, Y. Ben, Hilker, T., Black, T. A., Krishnan, P., Coops, N. C., & Huemmrich, K. F. (2009a). Linking foliage spectral responses to canopy-level ecosystem photosynthetic light-use efficiency at a douglas-fir forest in canada. *Canadian Journal of Remote Sensing*, 35(2), 166–188. <https://doi.org/10.5589/m09-008>
- Middleton, E. M., Cheng, Y.-B., Corp, L. A., Huemmrich, K. F., Campbell, P. K. E., Zhang, Q.-Y., ... Russ, A. L. (2009b). Diurnal and seasonal dynamics of canopy-level solar-induced chlorophyll fluorescence and spectral reflectance indices in a cornfield. *6th European Association of Remote Sensing Laboratories (EARSeL) SIG Imaging Spectroscopy Workshop*. Retrieved from <https://pdfs.semanticscholar.org/d01b/193b4a25cc6c849dd51966a46f00bc4d9ca8.pdf>
- Middleton, E. M., Cheng, Y. Ben, Corp, L. A., Campbell, P. K. E., Huemmrich, K. F., Zhang, Q., & Kustas, W. P. (2012). Canopy level Chlorophyll Fluorescence and the PRI in a cornfield. *International Geoscience and Remote Sensing Symposium (IGARSS)*, 7117–7120. <https://doi.org/10.1109/IGARSS.2012.6352022>
- Middleton, E. M., Rascher, U., Corp, L. A., Huemmrich, K. F., Cook, B. D., Noormets, A., ... Bianchi, R. (2017). The 2013 FLEX-US airborne campaign at the parker tract loblolly pine plantation in North Carolina, USA. *Remote Sensing*, 9(6), 1–31. <https://doi.org/10.3390/rs9060612>
- Migliavacca, M., Perez-Priego, O., Rossini, M., El-Madany, T. S., Moreno, G., van der Tol, C., ... Reichstein, M. (2017). Plant functional traits and canopy structure control the relationship between photosynthetic CO₂ uptake and far-red sun-induced fluorescence in a Mediterranean grassland under different nutrient availability. *New Phytologist*, 214(3), 1078–1091. <https://doi.org/10.1111/nph.14437>
- Migliavacca, M., Reichstein, M., Richardson, A. D., Mahecha, M. D., Cremonese, E., Delpierre, N., ... Cescatti, A. (2015). Influence of physiological phenology on the seasonal pattern of ecosystem respiration in deciduous forests. *Global Change Biology*, 21(1), 363–376. <https://doi.org/10.1111/gcb.12671>
- Mohammed, G. H., Colombo, R., Middleton, E. M., Rascher, U., van der Tol, C., Nedbal, L., ... Zarco-Tejada, P. J. (2019). Remote sensing of solar-induced chlorophyll fluorescence (SIF) in vegetation:

- 50 years of progress. *Remote Sensing of Environment*, 231(February), 111177. <https://doi.org/10.1016/j.rse.2019.04.030>
- Monteith, J. L. (1972). Solar Radiation and Productivity in Tropical Ecosystems. *The Journal of Applied Ecology*, 9(3), 747. <https://doi.org/10.2307/2401901>
- Müller, P., Li, X. P., & Niyogi, K. K. (2001). Non-photochemical quenching. A response to excess light energy. *Plant Physiology*, 125(4), 1558–1566. <https://doi.org/10.1104/pp.125.4.1558>
- Musavi, T., Mahecha, M. D., Migliavacca, M., Reichstein, M., van de Weg, M. J., van Bodegom, P. M., ... Kattge, J. (2015). The imprint of plants on ecosystem functioning: A data-driven approach. *International Journal of Applied Earth Observation and Geoinformation*, 43, 119–131. <https://doi.org/10.1016/j.jag.2015.05.009>
- Musavi, T., Migliavacca, M., van de Weg, M. J., Kattge, J., Wohlfahrt, G., van Bodegom, P. M., ... Mahecha, M. D. (2016). Potential and limitations of inferring ecosystem photosynthetic capacity from leaf functional traits. *Ecology and Evolution*, 6(20), 7352–7366. <https://doi.org/10.1002/ece3.2479>
- Nelson, J. A., Carvalhais, N., Cuntz, M., Delpierre, N., Knauer, J., Ogée, J., ... Jung, M. (2018). Coupling Water and Carbon Fluxes to Constrain Estimates of Transpiration: The TEA Algorithm. *Journal of Geophysical Research: Biogeosciences*, 123(12), 3617–3632. <https://doi.org/10.1029/2018JG004727>
- Niyogi, K. K., Björkman, O., & Grossman, A. R. (1997). The roles of specific xanthophylls in photoprotection. *Proceedings of the National Academy of Sciences of the United States of America*, 94(25), 14162–14167. <https://doi.org/10.1073/pnas.94.25.14162>
- Pacheco-Labrador, J., Hueni, A., Mihai, L., Sakowska, K., Julitta, T., Kuusk, J., ... Arthur, A. Mac. (2019). Sun-induced chlorophyll fluorescence I: Instrumental considerations for proximal spectroradiometers. *Remote Sensing*, 11(8). <https://doi.org/10.3390/rs11080923>
- Pacheco-Labrador, J., Perez-Priego, O., El-Madany, T. S., Julitta, T., Rossini, M., Guan, J., ... Migliavacca, M. (2019). Multiple-constraint inversion of SCOPE. Evaluating the potential of GPP and SIF for the retrieval of plant functional traits. *Remote Sensing of Environment*, 234(October), 111362. <https://doi.org/10.1016/j.rse.2019.111362>
- Paul-Limoges, E., Damm, A., Hueni, A., Liebisch, F., Eugster, W., Schaepman, M. E., & Buchmann, N. (2018). Effect of environmental conditions on sun-induced fluorescence in a mixed forest and a cropland. *Remote Sensing of Environment*, 219(November 2017), 310–323. <https://doi.org/10.1016/j.rse.2018.10.018>
- Peñuelas, J., Filella, I., & Gamon, J. A. (1995). Assessment of photosynthetic radiation-use efficiency with spectral reflectance. *New Phytologist*, 131(3), 291–296. <https://doi.org/10.1111/j.1469-8137.1995.tb03064.x>
- Perez-Priego, O., Guan, J., Rossini, M., Fava, F., Wutzler, T., Moreno, G., ... Migliavacca, M. (2015). Sun-induced chlorophyll fluorescence and photochemical reflectance index improve remote-sensing gross primary production estimates under varying nutrient availability in a typical Mediterranean savanna ecosystem. *Biogeosciences*, 12(21), 6351–6367. <https://doi.org/10.5194/bg-12-6351-2015>

- Perez-Priego, O., El-Madany, T. S., Migliavaca, M., Kowalski, A. S., Jung, M., Carrara, A., ... Reichstein, M. (2017). Evaluation of eddy covariance latent heat fluxes with independent lysimeter and sapflow estimates in a Mediterranean savannah ecosystem. *Agricultural and Forest Meteorology*, 236, 87–99. <https://doi.org/10.1016/j.agrformet.2017.01.009>
- Pinto, F., Müller-Linow, M., Schickling, A., Cendrero-Mateo, M. P., Ballvora, A., & Rascher, U. (2017). Multiangular observation of canopy sun-induced chlorophyll fluorescence by combining imaging spectroscopy and stereoscopy. *Remote Sensing*, 9(5). <https://doi.org/10.3390/rs9050415>
- Plascyk, J. A. (1975). The MK II Fraunhofer Line Discriminator (FLD-II) for Airborne and Orbital Remote Sensing of Solar-Stimulated Luminescence. *Optical Engineering*, 14(4). <https://doi.org/10.1117/12.7971842>
- Plascyk, J. A., & Gabriel, F. C. (1975). The Fraunhofer Line Discriminator MKII-An Airborne Instrument for Precise and Standardized Ecological Luminescence Measurement. *IEEE Transactions on Instrumentation and Measurement*, 24(4). <https://doi.org/10.1109/TIM.1975.4314448>
- Plaut, G., Ghil, M., & Vautard, R. (1995). Interannual and interdecadal variability in 335 years of central England temperatures. *Science*, 268(5211), 710–713. <https://doi.org/10.1126/science.268.5211.710>
- Porcar-Castell, A., Mac Arthur, A., Rossini, M., Eklundh, L., Pacheco-Labrador, J., Anderson, K., ... Vescovo, L. (2015). EUROSPEC: At the interface between remote-sensing and ecosystem CO₂ flux measurements in Europe. *Biogeosciences*, 12(20), 6103–6124. <https://doi.org/10.5194/bg-12-6103-2015>
- Porcar-Castell, A. (2011). A high-resolution portrait of the annual dynamics of photochemical and non-photochemical quenching in needles of *Pinus sylvestris*. *Physiologia Plantarum*, 143(2), 139–153. <https://doi.org/10.1111/j.1399-3054.2011.01488.x>
- Porcar-Castell, A., Pfundel, E., Korhonen, J. F. J., & Juurula, E. (2008). A new monitoring PAM fluorometer (MONI-PAM) to study the short- and long-term acclimation of photosystem II in field conditions. *Photosynthesis Research*, 96(2), 173–179. <https://doi.org/10.1007/s11120-008-9292-3>
- Porcar-Castell, A., Tyystjärvi, E., Atherton, J., Van Der Tol, C., Flexas, J., Pfundel, E. E., ... Berry, J. A. (2014). Linking chlorophyll a fluorescence to photosynthesis for remote sensing applications: Mechanisms and challenges. *Journal of Experimental Botany*. <https://doi.org/10.1093/jxb/eru191>
- Quirós Vargas, J., Bendig, J., Arthur, A. Mac, Burkart, A., Julitta, T., Maseyk, K., ... Rascher, U. (2020). Unmanned aerial systems (UAS)-based methods for solar induced chlorophyll fluorescence (SIF) retrieval with non-imaging spectrometers: State of the art. *Remote Sensing*, 12(10). <https://doi.org/10.3390/rs12101624>
- Rahman, A. F., Gamon, J. A., Fuentes, D. A., Roberts, D. A., & Prentiss, D. (2001). Modeling spatially distributed ecosystem flux of boreal forest using hyperspectral indices from AVIRIS imagery. *Journal of Geophysical Research Atmospheres*, 106(D24), 33579–33591. <https://doi.org/10.1029/2001JD900157>
- Rascher, U., Agati, G., Alonso, L., Cecchi, G., Champagne, S., Colombo, R., ... Zaldei, A. (2009). CEFLES2: The remote sensing component to quantify photosynthetic efficiency from the leaf to the

- region by measuring sun-induced fluorescence in the oxygen absorption bands. *Biogeosciences*, 6(7), 1181–1198. <https://doi.org/10.5194/bg-6-1181-2009>
- Rascher, U., Alonso, L., Burkart, A., Cilia, C., Cogliati, S., Colombo, R., ... Zemek, F. (2015). Sun-induced fluorescence - a new probe of photosynthesis: First maps from the imaging spectrometer HyPlant. *Global Change Biology*, 21(12), 4673–4684. <https://doi.org/10.1111/gcb.13017>
- Rebmann, C., Aubinet, M., Schmid, H., Arriga, N., Aurela, M., Burba, G., ... Franz, D. (2018). ICOS eddy covariance flux-station site setup: A review. *International Agrophysics*, 32(4), 471–494. <https://doi.org/10.1515/intag-2017-0044>
- Reda, I., & Andreas, A. (2004). Solar position algorithm for solar radiation applications. *Solar Energy*, 76(5), 577–589. <https://doi.org/10.1016/j.solener.2003.12.003>
- Reichstein, M., Bahn, M., Mahecha, M. D., Kattge, J., & Baldocchi, D. D. (2014). Linking plant and ecosystem functional biogeography. *Proceedings of the National Academy of Sciences of the United States of America*, 111(38), 13697–13702. <https://doi.org/10.1073/pnas.1216065111>
- Reichstein, M., Falge, E., Baldocchi, D., Papale, D., Aubinet, M., Berbigier, P., ... Valentini, R. (2005). On the separation of net ecosystem exchange into assimilation and ecosystem respiration: Review and improved algorithm. *Global Change Biology*, 11(9), 1424–1439. <https://doi.org/10.1111/j.1365-2486.2005.001002.x>
- Rocchini, D., Balkenhol, N., Carter, G. A., Foody, G. M., Gillespie, T. W., He, K. S., ... Neteler, M. (2010). Remotely sensed spectral heterogeneity as a proxy of species diversity: Recent advances and open challenges. *Ecological Informatics*, 5(5), 318–329. <https://doi.org/10.1016/j.ecoinf.2010.06.001>
- Roelofsen, H. D., van Bodegom, P. M., Kooistra, L., & Witte, J. P. M. (2014). Predicting leaf traits of herbaceous species from their spectral characteristics. *Ecology and Evolution*, 4(6), 706–719. <https://doi.org/10.1002/ece3.932>
- Rossini, M., Fava, F., Cogliati, S., Meroni, M., Marchesi, A., Panigada, C., ... Colombo, R. (2013). Assessing canopy PRI from airborne imagery to map water stress in maize. *ISPRS Journal of Photogrammetry and Remote Sensing*, 86, 168–177. <https://doi.org/10.1016/j.isprsjprs.2013.10.002>
- Rossini, M., Nedbal, L., Guanter, L., Ač, A., Alonso, L., Burkart, A., ... Rascher, U. (2015). Red and far red Sun-induced chlorophyll fluorescence as a measure of plant photosynthesis. *Geophysical Research Letters*, 42(6), 1632–1639. <https://doi.org/10.1002/2014GL062943>
- Rossini, M., Meroni, M., Celesti, M., Cogliati, S., Julitta, T., Panigada, C., ... Colombo, R. (2016). Analysis of red and far-red sun-induced chlorophyll fluorescence and their ratio in different canopies based on observed and modeled data. *Remote Sensing*, 8(5). <https://doi.org/10.3390/rs8050412>
- Rossini, M., Meroni, M., Migliavacca, M., Manca, G., Cogliati, S., Busetto, L., ... Colombo, R. (2010). High resolution field spectroscopy measurements for estimating gross ecosystem production in a rice field. *Agricultural and Forest Meteorology*, 150(9), 1283–1296. <https://doi.org/10.1016/j.agrformet.2010.05.011>
- Roujean, J. L., Leroy, M., & Deschamps, P. Y. (1992). A bidirectional reflectance model of the Earth's surface for the correction of remote sensing data. *Journal of Geophysical Research*, 97(D18), 20,455–20,468. <https://doi.org/10.1029/92jd01411>

93 | Bibliography

- Running, S. W., Nemani, R. R., Heinsch, F. A., Zhao, M., Reeves, M., & Hashimoto, H. (2004). A continuous satellite-derived measure of global terrestrial primary production. *BioScience*, 54(6), 547–560. [https://doi.org/10.1641/0006-3568\(2004\)054\[0547:ACSMOG\]2.0.CO;2](https://doi.org/10.1641/0006-3568(2004)054[0547:ACSMOG]2.0.CO;2)
- Sandmeier, S., Müller, C., Hosgood, B., & Andreoli, G. (1998). Physical mechanisms in hyperspectral BRDF data of grass and watercress. *Remote Sensing of Environment*, 66(2), 222–233. [https://doi.org/10.1016/S0034-4257\(98\)00060-1](https://doi.org/10.1016/S0034-4257(98)00060-1)
- Schaepman-Strub, G., Schaepman, M. E., Painter, T. H., Dangel, S., & Martonchik, J. V. (2006). Reflectance quantities in optical remote sensing—definitions and case studies. *Remote Sensing of Environment*, 103(1), 27–42. <https://doi.org/10.1016/j.rse.2006.03.002>
- Schaepman, M. E. (2007). Spectrodirectional remote sensing: From pixels to processes. *International Journal of Applied Earth Observation and Geoinformation*, 9(2), 204–223. <https://doi.org/10.1016/j.jag.2006.09.003>
- Schickling, A., Matveeva, M., Damm, A., Schween, J. H., Wahner, A., Graf, A., ... Rascher, U. (2016). Combining sun-induced chlorophyll fluorescence and photochemical reflectance index improves diurnal modeling of gross primary productivity. *Remote Sensing*, 8(7). <https://doi.org/10.3390/rs8070574>
- Serrano, L., Gamon, J. A., & Penuelas, J. (2000). Estimation of canopy photosynthetic and nonphotosynthetic components from spectral transmittance. *Ecology*, 81(11), 3149–3162. [https://doi.org/10.1890/0012-9658\(2000\)081\[3149:EOCPAN\]2.0.CO;2](https://doi.org/10.1890/0012-9658(2000)081[3149:EOCPAN]2.0.CO;2)
- Sims, D. A., & Gamon, J. A. (2002). Relationships between leaf pigment content and spectral reflectance across a wide range of species, leaf structures and developmental stages. *Remote Sensing of Environment*, 81(2–3), 337–354. [https://doi.org/10.1016/S0034-4257\(02\)00010-X](https://doi.org/10.1016/S0034-4257(02)00010-X)
- Soudani, K., Hmimina, G., Dufrêne, E., Berveiller, D., Delpierre, N., Ourcival, J. M., ... Joffre, R. (2014). Relationships between photochemical reflectance index and light-use efficiency in deciduous and evergreen broadleaf forests. *Remote Sensing of Environment*, 144, 73–84. <https://doi.org/10.1016/j.rse.2014.01.017>
- Stagakis, S., Markos, N., Sykoti, O., & Kyparissis, A. (2014). Tracking seasonal changes of leaf and canopy light use efficiency in a *Phlomis fruticosa* Mediterranean ecosystem using field measurements and multi-angular satellite hyperspectral imagery. *ISPRS Journal of Photogrammetry and Remote Sensing*, 97, 138–151. <https://doi.org/10.1016/j.isprsjprs.2014.08.012>
- Steinbrenner, J., & Linden, H. (2001). Regulation of two carotenoid biosynthesis genes coding for phytoene synthase and carotenoid hydroxylase during stress-induced astaxanthin formation in the green alga *Haematococcus pluvialis*. *Plant Physiology*, 125(2), 810–817. <https://doi.org/10.1104/pp.125.2.810>
- Strub, G., Schaepman, M. E., Knyazikhin, Y., & Itten, K. I. (2003). Evaluation of spectrodirectional Alfalfa canopy data acquired during DAISEX'99. *IEEE Transactions on Geoscience and Remote Sensing*, 41(5 PART 1), 1034–1042. <https://doi.org/10.1109/TGRS.2003.811555>
- Sun, Y., Frankenberg, C., Jung, M., Joiner, J., Guanter, L., Köhler, P., & Magney, T. (2018). Overview of Solar-Induced chlorophyll Fluorescence (SIF) from the Orbiting Carbon Observatory-2: Retrieval,

- cross-mission comparison, and global monitoring for GPP. *Remote Sensing of Environment*, 209(February), 808–823. <https://doi.org/10.1016/j.rse.2018.02.016>
- Sun, Y., Fu, R., Dickinson, R., Joiner, J., Frankenberg, C., Gu, L., ... Fernando, N. (2015). Drought onset mechanisms revealed by satellite solar-induced chlorophyll fluorescence: Insights from two contrasting extreme events. *Journal of Geophysical Research G: Biogeosciences*, 120(11), 2427–2440. <https://doi.org/10.1002/2015JG003150>
- Székely, G. J., Rizzo, M. L., & Bakirov, N. K. (2007). Measuring and testing dependence by correlation of distances. *Annals of Statistics*, 35(6), 2769–2794. <https://doi.org/10.1214/009053607000000505>
- Tagliabue, G., Panigada, C., Dechant, B., Baret, F., Cogliati, S., Colombo, R., ... Rossini, M. (2019). Exploring the spatial relationship between airborne-derived red and far-red sun-induced fluorescence and process-based GPP estimates in a forest ecosystem. *Remote Sensing of Environment*, 231(June), 111272. <https://doi.org/10.1016/j.rse.2019.111272>
- Tucker, C. J. (1979). Red and photographic infrared linear combinations for monitoring vegetation. *Remote Sensing of Environment*, 8(2), 127–150. [https://doi.org/10.1016/0034-4257\(79\)90013-0](https://doi.org/10.1016/0034-4257(79)90013-0)
- van Der Tol, C., Berry, J. A., Campbell, P. K. E., & Rascher, U. (2014). Models of fluorescence and photosynthesis for interpreting measurements of solar-induced chlorophyll fluorescence. *Journal of Geophysical Research: Biogeosciences*, 119(12), 2312–2327. <https://doi.org/10.1002/2014JG002713>
- van der Tol, C., Verhoef, W., Timmermans, J., Verhoef, A., & Su, Z. (2009). An integrated model of soil-canopy spectral radiance observations, photosynthesis, fluorescence, temperature and energy balance. *Biogeosciences Discussions*, 6(3), 6025–6075. <https://doi.org/10.5194/bgd-6-6025-2009>
- van Der Tol, C., Verhoef, W., Timmermans, J., Verhoef, A., & Su, Z. (2009). An integrated model of soil-canopy spectral radiances, photosynthesis, fluorescence, temperature and energy balance. *Biogeosciences*, 6(12), 3109–3129. <https://doi.org/10.5194/bg-6-3109-2009>
- van der Tol, C., Rossini, M., Cogliati, S., Verhoef, W., Colombo, R., Rascher, U., & Mohammed, G. (2016). A model and measurement comparison of diurnal cycles of sun-induced chlorophyll fluorescence of crops. *Remote Sensing of Environment*, 186, 663–677. <https://doi.org/10.1016/j.rse.2016.09.021>
- Van Wittenberghe, S., Alonso, L., Verrelst, J., Moreno, J., & Samson, R. (2015). Bidirectional sun-induced chlorophyll fluorescence emission is influenced by leaf structure and light scattering properties - A bottom-up approach. *Remote Sensing of Environment*, 158(2015), 169–179. <https://doi.org/10.1016/j.rse.2014.11.012>
- Verhoef, W. (1998). *Theory of radiative transfer models applied in optical remote sensing of vegetation canopies*. Wageningen Agricultural University. <https://doi.org/ISBNL 90-5485-804-4>
- Verhoef, W., van der Tol, C., & Middleton, E. M. (2018). Hyperspectral radiative transfer modeling to explore the combined retrieval of biophysical parameters and canopy fluorescence from FLEX – Sentinel-3 tandem mission multi-sensor data. *Remote Sensing of Environment*, 204, 942–963. <https://doi.org/10.1016/j.rse.2017.08.006>

- Vilfan, N., van der Tol, C., Muller, O., Rascher, U., & Verhoef, W. (2016). Fluspect-B: A model for leaf fluorescence, reflectance and transmittance spectra. *Remote Sensing of Environment*, 186, 596–615. <https://doi.org/10.1016/j.rse.2016.09.017>
- Vilfan, N., Van der Tol, C., Yang, P., Wyber, R., Malenovský, Z., Robinson, S. A., & Verhoef, W. (2018). Extending Fluspect to simulate xanthophyll driven leaf reflectance dynamics. *Remote Sensing of Environment*, 211(March), 345–356. <https://doi.org/10.1016/j.rse.2018.04.012>
- Violle, C., Navas, M.-L., Vile, D., Kazakou, E., Fortunel, C., Hummel, I., & Garnier, E. (2007). Let the concept of trait be functional! *Oikos*, 116(5), 882–892. <https://doi.org/10.1111/j.2007.0030-1299.15559.x>
- Walter-Shea, E. A., Privette, J., Cornell, D., Mesarch, M. A., & Hays, C. J. (1997). Relations between directional spectral vegetation indices and leaf area and absorbed radiation in alfalfa. *Remote Sensing of Environment*, 61(1), 162–177. [https://doi.org/10.1016/S0034-4257\(96\)00250-7](https://doi.org/10.1016/S0034-4257(96)00250-7)
- Wang, T., Brender, P., Ciais, P., Piao, S., Mahecha, M. D., Chevallier, F., ... Vaccari, F. P. (2012). State-dependent errors in a land surface model across biomes inferred from eddy covariance observations on multiple timescales. *Ecological Modelling*, 246(C), 11–25. <https://doi.org/10.1016/j.ecolmodel.2012.07.017>
- Wohlfahrt, G., Gerdel, K., Migliavacca, M., Rotenberg, E., Tatarinov, F., Müller, J., ... Yakir, D. (2018). Sun-induced fluorescence and gross primary productivity during a heat wave. *Scientific Reports*, 8(1), 1–9. <https://doi.org/10.1038/s41598-018-32602-z>
- Wong, C. Y. S., & Gamon, J. A. (2015). Three causes of variation in the photochemical reflectance index (PRI) in evergreen conifers. *New Phytologist*, 206(1), 187–195. <https://doi.org/10.1111/nph.13159>
- Yang, H., Yang, X., Zhang, Y., Heskel, M. A., Lu, X., Munger, J. W., ... Tang, J. (2017). Chlorophyll fluorescence tracks seasonal variations of photosynthesis from leaf to canopy in a temperate forest. *Global Change Biology*, 23(7), 2874–2886. <https://doi.org/10.1111/gcb.13590>
- Yang, P., & van der Tol, C. (2018). Linking canopy scattering of far-red sun-induced chlorophyll fluorescence with reflectance. *Remote Sensing of Environment*, 209(May), 456–467. <https://doi.org/10.1016/j.rse.2018.02.029>
- Yang, X., Shi, H., Stovall, A., Guan, K., Miao, G., Zhang, Y., ... Lee, J. E. (2018). FluoSpec 2—an automated field spectroscopy system to monitor canopy solar-induced fluorescence. *Sensors (Switzerland)*, 18(7). <https://doi.org/10.3390/s18072063>
- Yang, X., Tang, J., Mustard, J. F., Lee, J. E., Rossini, M., Joiner, J., ... Richardson, A. D. (2015). Solar-induced chlorophyll fluorescence that correlates with canopy photosynthesis on diurnal and seasonal scales in a temperate deciduous forest. *Geophysical Research Letters*, 42(8), 2977–2987. <https://doi.org/10.1002/2015GL063201>
- Yiou, P., Baert, E., & Loutre, M. F. (1996). Spectral analysis of climate data. *Surveys in Geophysics*, 17(6), 619–663. <https://doi.org/10.1007/BF01931784>
- Zarco-Tejada, P.J., 2000. "Hyperspectral Remote Sensing of Closed Forest Canopies: Estimation of Chlorophyll Fluorescence and Pigment Content." PhD diss. York University Toronto.

- Zarco-Tejada, P. J., González-Dugo, V., & Berni, J. A. J. (2012). Fluorescence, temperature and narrow-band indices acquired from a UAV platform for water stress detection using a micro-hyperspectral imager and a thermal camera. *Remote Sensing of Environment*, 117, 322–337. <https://doi.org/10.1016/j.rse.2011.10.007>
- Zeng, Y., Badgley, G., Dechant, B., Ryu, Y., Chen, M., & Berry, J. A. (2019). A practical approach for estimating the escape ratio of near-infrared solar-induced chlorophyll fluorescence. *Remote Sensing of Environment*, 232(July), 111209. <https://doi.org/10.1016/j.rse.2019.05.028>
- Zhang, C., Atherton, J., Peñuelas, J., Filella, I., Kolari, P., Aalto, J., ... Porcar-Castell, A. (2019). Do all chlorophyll fluorescence emission wavelengths capture the spring recovery of photosynthesis in boreal evergreen foliage? *Plant Cell and Environment*, 42(12), 3264–3279. <https://doi.org/10.1111/pce.13620>
- Zhang, Q., Ju, W., Chen, J. M., Wang, H., Yang, F., Fan, W., ... Chou, S. (2015). Ability of the photochemical reflectance index to track light use efficiency for a sub-tropical planted coniferous forest. *Remote Sensing*, 7(12), 16938–16962. <https://doi.org/10.3390/rs71215860>
- Zhang, Q., M. Chen, J., Ju, W., Wang, H., Qiu, F., Yang, F., ... Zhang, F. (2017). Improving the ability of the photochemical reflectance index to track canopy light use efficiency through differentiating sunlit and shaded leaves. *Remote Sensing of Environment*, 194, 1–15. <https://doi.org/10.1016/j.rse.2017.03.012>
- Zhang, X., Friedl, M. A., Schaaf, C. B., Strahler, A. H., Hodges, J. C. F., Gao, F., ... Huete, A. (2003). Monitoring vegetation phenology using MODIS. *Remote Sensing of Environment*, 84(3), 471–475. [https://doi.org/10.1016/S0034-4257\(02\)00135-9](https://doi.org/10.1016/S0034-4257(02)00135-9)
- Zhao, F., Gu, X., Verhoef, W., Wang, Q., Yu, T., Liu, Q., ... Zhao, H. (2010). A spectral directional reflectance model of row crops. *Remote Sensing of Environment*, 114(2), 265–285. <https://doi.org/10.1016/j.rse.2009.09.018>
- Zhao, F., Li, Y., Dai, X., Verhoef, W., Guo, Y., Shang, H., ... Huang, J. (2015). Simulated impact of sensor field of view and distance on field measurements of bidirectional reflectance factors for row crops. *Remote Sensing of Environment*, 156, 129–142. <https://doi.org/10.1016/j.rse.2014.09.011>
- Zheng, G., & Moskal, L. M. (2009). Retrieving Leaf Area Index (LAI) Using Remote Sensing: Theories, Methods and Sensors. *Sensors*, 9(4), 2719–2745. <https://doi.org/10.3390/s90402719>